Influences of Free-Stream Turbulence and Char-Layer Porosity on the Drag on Windborne Firebrands

Alexandre Cohen

Master of Engineering

Department of Mechanical Engineering

McGill University

Montréal, Québec

August 2018

A thesis submitted to McGill University in partial fulfillment of the requirements of the degree of Master of Engineering.

DEDICATION

To my wife Erica, for making it all possible, and worth it.

ACKNOWLEDGEMENTS

When I returned to school after close to 5 years in the workforce, I was looking for an intellectual challenge. Though this Master's degree did not turn out quite the way I expected it to, I definitely found the challenge I was looking for. I would like to thank, first and foremost, my supervisors, Professor Rabi Baliga and Professor Laurent Mydlarski, for inspiring me to return to school, and for all their support and guidance throughout the past two years. You have both taught me the value of integrity and discipline in scientific research. I would also like to thank the Natural Sciences and Engineering Research Council (NSERC) of Canada, the Fonds de Recherche du Québec − Nature et Technologies (FRQNT), the Professor Lucjan Kops foundation, and McGill University, for providing me with financial support throughout the course of my studies. I would like to extend a big thank you to my colleagues in the Aerodynamics laboratory: Alaïs Hewes, for teaching me to make hot-wires, and making them for me when the situation was desperate; Donovan Blais, without whose help I likely would never have finished all of my experiments; Milind Singh, who bench-marked all the equipment in the lab (so I wouldn't have to); and Vincent Tremblay-Dionne, who always had helpful insights to share (or at the very least, was free to grab some breakfast). I would also like to thank my other colleagues, Mike Hinton, Kevin Venne, Stephen Camozzi, James Medveszek, and Osaid Matar, for their help and support, whether it was by discussing ideas, comparing notes, or just having a laugh. Thank you to my friend Adam Smith for our weekly therapy sessions (all it cost me was a few Cannolis). Thank you as well to the technicians in the machine shop, Mathieu and Lydia, who were always ready to help or give advice in the machining of parts for this project. Finally, I would like to thank my family for their support during this period, and most importantly my wife Erica, who encouraged me to return to school, stood by me every step of the way, and lived through every issue by my side, whether it was a bad exam, an equipment failure, bringing me dinner during late night tests, or picking me up at the end of long days.

ABSTRACT

A better understanding of the mechanisms that cause or affect the propagation of forest fires is essential for their effective mitigation and control. One such mechanism is spotting, in which burning leaves, branches, and other debris, termed firebrands, are transported away from the main fire by the prevailing wind and ignite new fires. Spotting has been investigated in several experimental and numerical studies. However, the influences of free-stream turbulence and char-layer porosity on the trajectories of windborne firebrands have not been accounted for in these past studies. In this work, wind tunnel experiments were conducted to quantify the effects of free-stream turbulence intensity and char-layer porosity on the drag on stationary non-burning cylinders. A wind tunnel was set up to conduct the experiments, and the flow in its test section was characterized. A combination of passive and active grids was used to generate turbulence intensities of 1.7%, 2.7%, and 12.4% (with no grid installed, the background turbulence intensity was 0.4%). The porous char-layer was mimicked by wrapping wire meshes around the cylinders, with three values of pores per inch (10, 20, and 40) and wrapped to three different thicknesses ($1/16$", $1/8$", and $1/4$"). The drag on one smooth cylinder and nine cylinders with porous outer layers (1" diameter, 11.75" length exposed to air flow) was measured for Reynolds number in the range 7000 to 17000, at the aforementioned four turbulence intensities. The results showed that i) the free-stream turbulence intensity and pores per inch of the wire meshes affect the way in which the drag coefficient changes with Reynolds number; ii) the drag coefficient increases with free-stream turbulence intensity when it is relatively low ($0.4\% - 2.7\%$), then decreases at high turbulence intensity (12.4%), and this decrease is more pronounced as the number of pores per inch is increased; iii) the drag coefficient increases with the thickness of the porous layer, and asymptotes to an effectively constant value after a critical thickness of about $1/8$"; and iv) the drag coefficient exhibits a non-monotonic dependence on the number of pores per inch of the wire mesh. These results demonstrate the importance of accounting for the

free-stream turbulence intensity and the char-layer (porosity and depth) when modelling the drag on windborne firebrands. It is hoped that this work will eventually lead to a better understanding of the spread of forest fires by spotting, allow more accurate predictions of it, and thus enable better forest-fire prevention and suppression strategies.

RÉSUMÉ

Une meilleure compréhension des mécanismes qui affectent la propagation des feux de forêts est essentielle pour pouvoir les maîtriser. Un de ces mécanismes comprend le transport d'éléments végétaux (branches, feuilles, écorce) enflammés, appelés brandons, par le vent à des distances de centaines de mètres pour entamer des nouveaux feux. Ce mécanisme est connu sous le nom phénomène des sautes. Il existe de nombreuses études expérimentales et numériques sur les trajectoires de brandons enflammés dans l'atmosphère. Cependant, les effets de la turbulence dans l'atmosphère, et de la porosité de la couche de résidu charbonneux formée sur les brandons, n'ont pas été pris en compte. Le but de ce projet est de quantifier, à l'aide d'expériences dans une soufflerie, les effets de la turbulence et de la porosité de la couche de résidu charbonneux sur la trainée sur des cylindres stationnaires non-brûlants. Une soufflerie a été installé, et son écoulement a été caractérisé. Des intensités de turbulence de 1.7%, 2.7%, et 12.4% ont été créées à l'aide de grilles passives et actives installées dans le tunnel (l'intensité de la turbulence sans aucune grille installée était de 0.4%). Pour simuler la porosité de la couche de résidu charbonneux, les cylindres ont été enveloppés de grillages métalliques. Une combinaison de trois différentes valeurs de pores par pouces (10, 20, et 40) et trois épaisseurs de la couche poreuse ($1/16$", $1/8$", et $1/4$") ont été utilisées. La trainée sur un cylindre lisse et neuf cylindres avec couches poreuses (avec des diamètres de 1", et des longueurs exposées à l'air de 11.75") a été mesurée pour des nombres de Reynolds entre 7000 et 17000, aux quatre intensités de turbulence mentionnés ci-haut. Les résultats démontrent que i) l'intensité de la turbulence et le nombre de pores par pouce des grillages métalliques affectent la relation entre le coefficient de trainée et le nombre de Reynolds; ii) le coefficient de trainée augmente quand l'intensité de la turbulence est augmentée, quand celle-ci est basse ($0.4\% - 2.7\%$), et ensuite baisse à haute intensité de turbulence (12.4%), et cette baisse est une fonction du nombre de pores par pouce; iii) le coefficient de trainée augmente avec l'épaisseur de la couche poreuse, et cesse d'augmenter après une épaisseur d'environ $1/8$";

et iv) le coefficient de trainée a une relation non-monotone avec le nombre de pores par pouce des grillages métalliques. Ces résultats démontrent l'importance de prendre en compte les effets de l'intensité de la turbulence et de la couche de résidu charbonneux (porosité et épaisseur) dans la modélisation de la trainée sur les brandons. Il est à espérer que ce travail mènera éventuellement à une meilleure compréhension de la propagation de feux de forêts par le phénomène de saute, ainsi qu'à des prédictions plus précises de ce phénomène, pour pouvoir améliorer la prévention et la suppression de feux de forêts.

TABLE OF CONTENTS

LIST OF TABLES

LIST OF FIGURES

CHAPTER 1
Introduction

1.1 Background and Motivation

Forest fires have increased in frequency and intensity over the past 10-15 years, with significant adverse impacts on humans, flora and fauna (Adams 2013). For example, in 2016, a major forest fire forced the evacuation of over 88,000 residents in Fort McMurray, Alberta (Simms 2016). Just one year later, in 2017, a series of forest fires in British Columbia caused the evacuation of over 65,000 citizens (British Columbia Wildfire Service 2018). Also in 2017, wildfires in Portugal and California resulted in the deaths of 66 and 44 people, respectively (Aon Benfield 2018). Given these and the many other events related to damaging and catastrophic forest fires, i) enhancing our understanding of the mechanisms that lead to their propagation, and ii) improving the techniques that are used to predict their spread are more pertinent than ever.

Viegas (1998) grouped forest fires into three main categories based on the ways they propagate: ground fires, which usually burn without flame, and propagate in the organic layer above the soil; surface fires, in which flaming combustion occurs in vegetation at or near the surface; and crown fires, which extend to the upper layers of the foliage, that can consume groups of trees and achieve a state of sustained propagation to the surrounding foliage.

Crown fires can also spread by spotting, a propagation mechanism in which burning leaves, branches, and/or other debris, termed firebrands, are ejected and entrained into prevailing winds and transported hundreds of meters away from the main fire, igniting new fires (Anthenien *et al.* 2006). A schematic of the spotting mechanism, taken from the work of Oliveira *et al.* (2014), is presented in Figure 1–1. In large-scale forest fires, spotting is often the dominant propagation mechanism, and the most difficult to control (Koo *et al.* 2010).

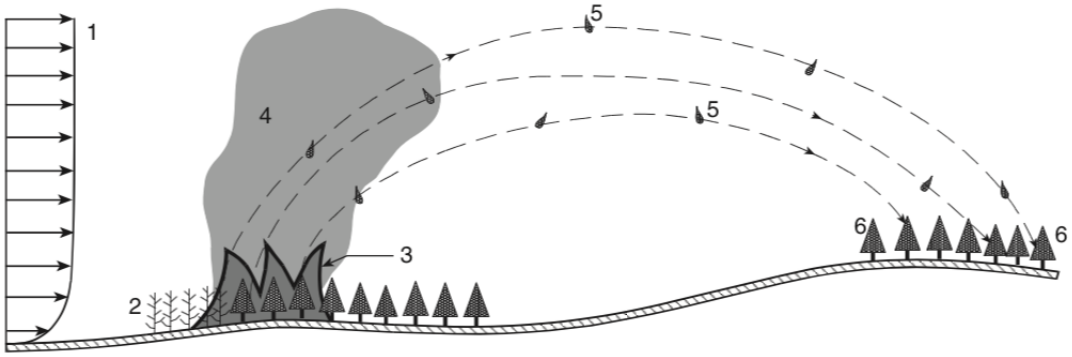

Figure 1–1: Schematic illustration of the spotting process. Taken from the work of Oliveira *et al.* (2014). 1, wind profile; 2, burned vegetation; 3, main fire; 4, plume; 5, firebrands; and 6, receptive fuel bed.

The propagation of forest fires by spotting has been investigated via field observations (Ohmiya and Iwami 2000), laboratory experiments (Tarifa *et al.* 1965; Manzello *et al.* 2011) and numerical simulations (Yin *et al.* 2003; Anthenien *et al.* 2006; Sardoy *et al.* 2007; Oliveira *et al.* 2014). Tarifa *et al.* (1965) conducted wind tunnel experiments to measure the forces and lifetimes of burning cylindrical and spherical objects representing firebrands. Based on these measurements, they estimated the maximum spotting distance of firebrands. More recently, Oliveira *et al.* (2014) used numerical simulations to determine the effects of initial orientation, oscillations, and spin of windborne cylindrical firebrands on their trajectories.

However, up to now, the investigations reported in the published literature have not accounted for two key aspects that could have a significant impact on the drag and lift experienced by windborne firebrands, and thus influence their trajectories: the free-stream turbulence in the atmosphere, and the porous char layer that forms on burning firebrands, as elaborated below.

The atmosphere is typically in a highly turbulent state. Counihan (1975) reviewed different investigations into atmospheric turbulence and summarized its properties: the turbulence intensities near the ground range from 10% to 20% in non-urban areas, and 20% to 35% in urban areas; the height of the atmospheric boundary layer over the ground ranges from 400m

to 800m; and the integral length scale of the turbulence increases with increasing height, with length scales near the ground of 10m to 200m in the direction of the prevailing winds.

The burning of wood is characterized by three processes: ignition; pyrolysis (a subsurface thermochemical process that causes decomposition of organic substances and produces volatile gases); and surface combustion, which produces a porous char layer (mostly carbon) on the particle (Sardoy *et al.* 2007). A schematic of this burning process for a cylindrical firebrand, taken from the work of Sardoy *et al.* (2007), is presented in Figure 1–2.

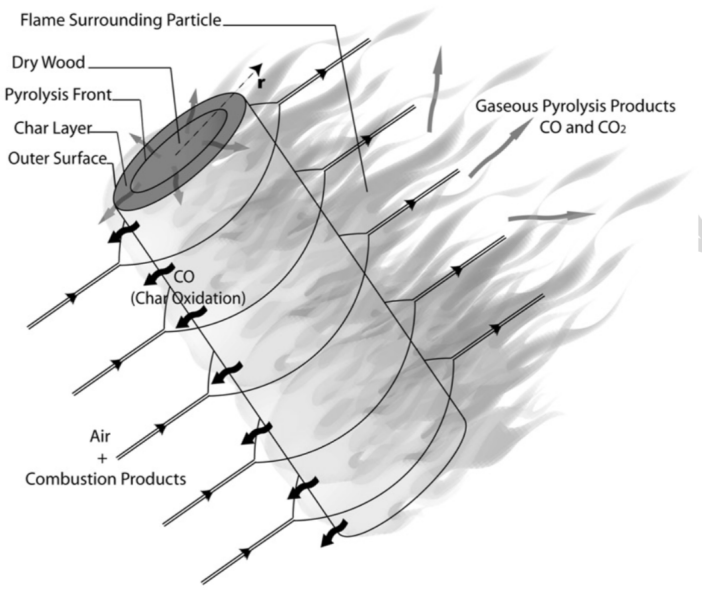

Figure 1–2: Schematic representation of a cylindrical wood particle undergoing pyrolysis and surface combustion. Taken from the work of Sardoy *et al.* (2007).

The characteristics of the char layer formed on burning wood have been investigated by Ragland *et al.* (1991). They found that this char layer has a porosity of 0.8 to 0.9, and a density of 10% to 20% of that of the dry wood. A picture of a wood particle having undergone combustion is presented in Figure 1–3. In this figure, the black, rough surface of the particle indicates the char layer. Even with the naked eye, it can be observed that the char layer is far from smooth.

In the investigations mentioned above, the firebrands were modelled as cylinders, disks or spheres, and their trajectories were estimated by measuring the drag and lift on them.

Figure 1–3: Char.

The present work will investigate the drag on cylinders. The overall goal of this project is to study the effects of free-stream turbulence and char-layer porosity and depth on the drag on cylindrical objects representing non-burning firebrands. It is the first step of a more comprehensive study aimed at making more accurate predictions of the trajectories of windborne firebrands.

1.2 Objectives

The objectives of this project are summarized below:

1. Setting up of a wind tunnel fitted with passive and active grids, to achieve the desired ranges of mean velocity and turbulent intensity.
2. Characterization of the flow in the test section of the wind tunnel, including the mean velocity profiles and turbulence statistics.
3. Quantification of the effects of free-stream turbulence on the drag on smooth cylinders in uniform cross-flow.
4. Quantification of the effects of a porous outer layer, mimicking the char layer on firebrands, on the drag on cylinders in uniform cross-flow, for various free-stream turbulence intensities.

1.3 Methodology

In the context of the first objective outlined in the previous section, a wind tunnel was assembled and set up, as described in §3.1. A blower was selected, acquired and installed to achieve mean velocities of 4m/s to 10m/s. Passive grids were installed upstream of the test section to generate low to intermediate intensities of turbulence (1.7% to 2.7%).

To generate turbulence intensities within the range encountered in the atmosphere (as mentioned above), an active grid was installed in the tunnel, following the recommendations of Mydlarski (2017). The active grid consists of rotating bars with agitator wings. Stepper motors are used to turn the bars back and forth, creating a flapping motion of the wings. A controller was designed and built to control the active grid in such a way as to achieve effectively isotropic, homogeneous turbulence, as per the work of Mydlarski (2017). The active grid and controller are described in more detail in §3.1.3.

In the context of the second objective, the flow in the test section of the wind tunnel was characterized. The mean velocity profiles, turbulence intensities, and integral lengths scales were measured without and with grids (passive and active). With the grids in place, turbulence intensities of 1.7% to 12.4% and integral length scales of 0.02m to 0.12m were generated. Due to the limited size of the wind tunnel and the capabilities of the instrumentation available for this work, it is not possible to replicate the ratio of integral length scale to firebrand size (diameter) in the atmosphere, which is on the order of $10^3 - 10^4$. Thus, the focus of this study is on the effects of free-stream turbulence intensities on the drag on cylinders in uniform cross-flow (and does not explicitly consider the effects of different turbulent length scales).

To minimize blockage effects, while still achieving the desired range of Reynolds numbers, 1" (0.0254m) diameter cylinders were used. Blockage effects were taken into account using the method described by Dalton (1971). To minimize end effects on the cylinder, flat plates were installed near each end of the cylinder, using the design recommended by Stansby (1974).

In the context of the third objective, the cylinders were suitably mounted on a wind tunnel balance to measure the drag at different mean velocities and turbulence intensities. The wind tunnel balance, a Kineoptics WTB 3.0 model, was installed and calibrated, as described in §3.3. The velocity and free-stream turbulence were measured using hot-wire anemometry.

The drag on circular cylinders is a function of the Reynolds number, a dimensionless parameter that can be considered as the ratio of inertial to viscous forces. For a circular cylinder in uniform cross-flow, the Reynolds number is:

$$Re_D \equiv \frac{\rho \overline{U} D}{\mu}, \tag{1.1}$$

where ρ is the fluid density, $\overline{U}$ is the mean velocity upstream of the cylinder, D is the cylinder diameter, and μ is the dynamic viscosity of the fluid. The Reynolds numbers achieved in this study ranged from 7000 to 17000.

Several options were explored with respect to acquiring solid cylinders with porous outer layers. There exist numerous suppliers of porous metal cylinders and solid cylinders with a porous outer layer. For example, Exxentis is a manufacturer of porous aluminum products. A sample of products from their catalogue is presented in Figure 1–4. However, such commercial products tend to be available in standard sizes only; customization is possible, but very costly. It has furthermore been found that products with the same model number and manufactured by the same supplier can have significant differences in their characteristics (Medvescek 2013).

After consideration of the reliability, availability, and cost-effectiveness of the different options, it was decided to use porous wire meshes wrapped around solid cylinders. This enabled control over the depth of the porous layer, as well as its porosity. Three different wire meshes (10, 20 and 40 pores per inch) were acquired to achieve different porosities. Three different nominal depths of the porous layer were also investigated ($1/16$" (0.0016m), $1/8$" (0.0032m), and $1/4$" (0.0064m)). Even using this method, much trial and error was required to implement a satisfactory procedure for wrapping the meshes around the cylinders. More details about this procedure are presented in §3.6.

Figure 1–4: Porous metal samples from an Exxentis catalogue.

1.4 Organization of the Thesis

In the earlier sections of Chapter 1, the background, motivation, objectives and methodology were presented. Chapter 2 presents a review of publications that are relevant to the present work. Descriptions of the experimental apparatus and techniques are detailed in Chapter 3, including the wind tunnel, passive and active grids, wind tunnel balance, and cylinders, without and with porous outer layers. In Chapter 4, the results are presented and discussed. Finally, conclusions, as well as a review of the thesis and suggestions for future work related to this study, are given in Chapter 5.

CHAPTER 2
Literature Review

There have been numerous publications on both the trajectories of windborne firebrands and the flow over circular cylinders. The goal in this chapter is not the presentation of an exhaustive review of this literature; instead, it is a review of publications directly related to the present work. This review is subdivided into the following sections: §2.1 trajectories of windborne firebrands; §2.2 drag over circular cylinders; and §2.3 turbulence.

2.1 Trajectories of Windborne Firebrands

The first study of trajectories of burning firebrands was published in 1965 by Tarifa *et al.* (1965), who conducted wind tunnel experiments to measure the drag on burning spherical and cylindrical objects representing firebrands. By measuring the firebrand size as it burned, they developed models to quantify the variation of the mass and density of the particles as a function of time and wind speed. The effects of particle size, type of wood, and moisture content on the drag and burning time were investigated. An important result from this study was that firebrands were observed to quickly reach a constant velocity during flight, equal to their terminal velocity. Based on this observation, the trajectories of the firebrands were calculated, and the maximum spotting distance of still-burning firebrands was estimated.

Tarifa *et al.* (1965) studied two different types of convection columns from which the firebrands would be ejected: i) a vertical convection column, in which the firebrands were lofted and then transported by a horizontal wind of constant velocity; and ii) an inclined convection column of a given width, in which the initial position of the firebrands determined the points at which they were ejected from the column. Another type of convection column that can loft firebrands are fire whirls, swirling natural convection plumes, which are more common in forest fires than vertical convection columns, and can result in greater spotting distances (Lee and Hellman 1969; Koo *et al.* 2010). Lee and Hellman (1969, 1970) analytically

and experimentally studied the behaviour of burning spherical firebrands of constant density lofted by fire whirls. They found that the parameters that governed the particle trajectories (and the maximum spotting distance) were the burning rate, initial size, initial position in the plume, and density of the firebrand. In a series of reports, Muraszew *et al.* (1975) and Muraszew and Fedele (1976, 1977) extended this work to develop models for the evolution of both the density and the mass of burning firebrands with time. They showed that for typical fire whirl heights (600m to 1200m), cylindrical firebrands can travel several kilometers, and land while still burning.

Further studies have sought to improve the predictions of forest fire spotting by improving models for one or more of the following: i) the firebrand trajectories; ii) the variation of mass and density of the firebrands with time; and iii) the convection columns from which the firebrands are lofted. More specifically, Albini (1979, 1981) studied the motion of cylindrical firebrands lofted from a line fire. He showed that the change in the diameter of a cylindrical firebrand with time is linearly proportional to the relative speed of the wind to the firebrand. He used these results to model the maximum lofting height of firebrands, as well as the maximum spotting distance of firebrands emitted from a line fire. Woycheese *et al.* (1999) challenged the assumption that firebrands are lofted at a constant vertical velocity, and used a more accurate fire plume flow field developed by Baum and McCaffrey (1989) to model the vertical lofting of firebrands.

In more recent years, the trajectories of burning firebrands have been studied numerically. Tse and Fernandez-Pello (1998) studied the flight of spherical embers generated by the collision of power lines with trees. Anthenien *et al.* (2006) extended this work by considering spheres, cylinders, and disks in their model. They found that disk-shaped particles flying with their axis perpendicular to the wind travelled 3 and 10 times farther than cylinders and spheres respectively. Sardoy *et al.* (2007) studied the effects of fire intensity and wind speed on firebrand trajectories for cylinders and disks. They found that the distance travelled by the firebrands varies almost linearly with wind speed, but varies little with fire intensity.

Finally, Oliveira *et al.* (2014) observed that cylinders do not always fly with their axis perpendicular to the wind, as assumed in previous studies, but tend to oscillate and spin during flight. They found that the initial orientation, oscillations, and spin of cylindrical firebrands had a significant effect on their trajectories.

2.2 Drag on Circular Cylinders

In all of the studies mentioned in the previous section, the firebrands were approximated as cylinders, spheres or disks, and the trajectories were determined from the drag and lift on these objects. As noted in Chapter 1, following this approach, the present work will focus on the drag on circular cylinders representing firebrands.

As previously stated, the flow around circular cylinders varies with the Reynolds number ($Re_D \equiv \frac{\rho \overline{U} D}{\mu}$). The regimes of flow over a cylinder at different ranges of Re_D are summarized in Figure 2–1, taken from the work of Lienhard (1966). At very low Re_D, the flow follows the contour of the cylinder without separation. For $5 \lesssim Re_D \lesssim 40$, symmetric vortices (termed Föppl vortices) are formed in the near wake, behind the cylinder. These continue to stretch as Re_D is increased, until they become unstable at $Re_D \sim 45$, and then the vortices detach periodically from alternating sides of the cylinder. This phenomenon, termed a vortex street, was first observed by von Kármán in 1911 (Von Kármán 1911).

Roshko (1954) observed that the vortex street transitions to turbulence in the range $150 \lesssim Re_D \lesssim 300$, becoming fully turbulent at $Re_D \gtrsim 300$, though the boundary layer along the surface of the cylinder remains laminar. In this flow regime, called the subcritical regime, the boundary layer separates from the cylinder at an angle of about 80 degrees from the front stagnation point. This continues until $Re_D \sim 1.5 \times 10^5$, when the boundary layer begins to transition from laminar to turbulent. In this transitional regime, the separation point moves downstream to approximately 140 degrees from the front stagnation point, and the vortex street is disrupted. For $Re_D \gtrsim 3.5 \times 10^6$, called the supercritical regime, the vortex street reappears downstream of the cylinder.

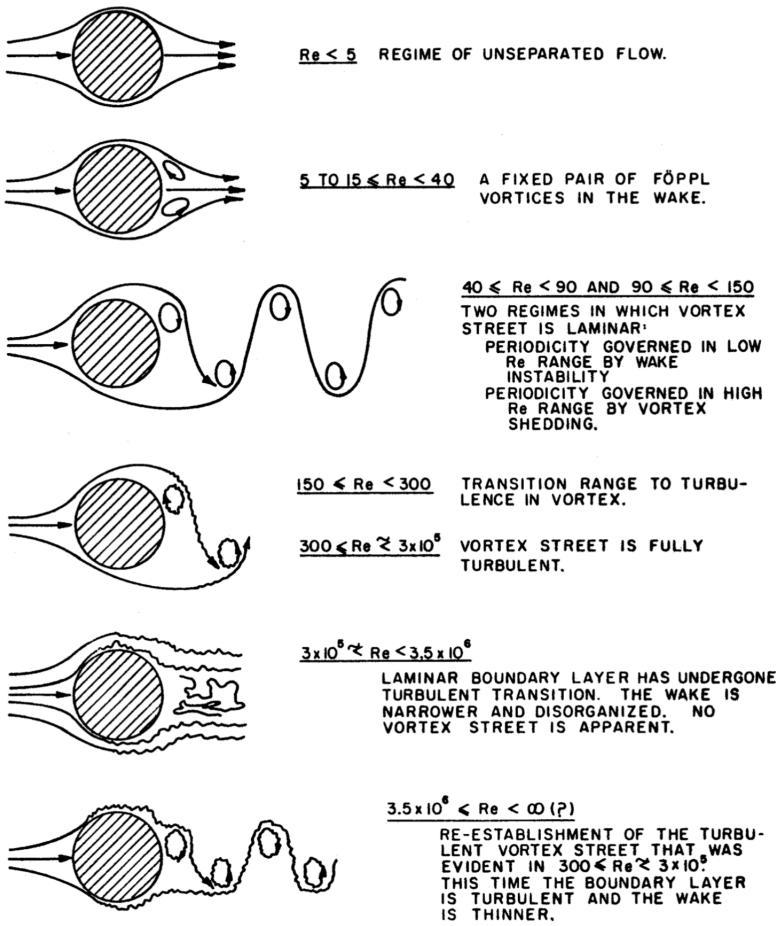

Figure 2–1: Regimes of flow over a cylinder for different ranges of Reynolds numbers. Taken from the work of Lienhard (1966).

2.2.1 Smooth Cylinders in Cross-Flow with Low Free-Stream Turbulence

The drag on smooth circular cylinders in cross-flow has been the subject of numerous investigations over the past century. The dimensionless parameter quantifying the drag on an object is the drag coefficient (C_D). It is defined as:

$$C_D \equiv \frac{F_{drag}/A_{proj}}{\frac{1}{2}\rho U_\infty^2}, \tag{2.1}$$

where F_{drag} is the drag force on an object, A_{proj} is the projected frontal area of an object, ρ is the fluid density, and U_∞ is the mean upstream velocity of the flow. The drag can be divided into two categories: viscous drag, caused by the friction on the surface of an object;

and form drag, caused by a net pressure difference between the upstream and downstream faces of an object.

One of the first to publish measurements of C_D on circular cylinders was Wieselsberger (1921). In his study, the drag coefficient was measured over a wide range of Reynolds numbers. The results are summarized in Figure 2–2, taken from the work of Schulz and Kallinderis (2000). For $Re_D \lesssim 10^3$, C_D decreases with increasing Re_D. In the range $10^3 \lesssim Re_D \lesssim 1.5 \times 10^5$, C_D is relatively invariant with respect to changes in Re_D. In the range $1.5 \times 10^5 \lesssim Re_D \lesssim 3.5 \times 10^5$, the boundary layer undergoes transition to turbulence, and the flow separation point on the cylinder moves downstream, from approximately 80 to 140 degrees (from the front stagnation point). This significantly and fairly abruptly reduces the form drag, and therefore C_D — a phenomenon referred to as the drag crisis. The Reynolds number at which this occurs is referred to as the critical Reynolds number $Re_{D,crit}$, is most often defined as that at which the C_D drops to 0.8, and is generally around $Re_D \sim 3 \times 10^5$ (Bearman and Morel 1983).

In such experiments, cylinders are assumed to be infinitely long, and the flow over them quasi-two-dimensional. However, the aspect ratio of the cylinder (i.e., the ratio of its length to its diameter (L/D)) can have an important effect on the drag coefficient and its dependence on the Reynolds number. In the results published by Wieselsberger (1921), the aspect ratios were high enough (280 and above) to be considered infinite. However, in most laboratory conditions, such high aspect ratios may not always be achievable. Figure 2–3, taken from the work of Zdravkovich *et al.* (1989), summarizes the effect of the aspect ratio on C_D using data from multiple investigations. As can be observed, even a cylinder with an aspect ratio of 20 exhibits a significantly lower C_D than that of an infinitely-long cylinder.

In addition to the effect of finite cylinder aspect ratios, the study of cylinders in wind tunnel experiments can also be affected by wall-interference effects if the ratio of the cylinder diameter to the tunnel width is not negligible. This causes the measured values of C_D to be overestimated. Fortunately, correlations exist to correct for these blockage effects. To this

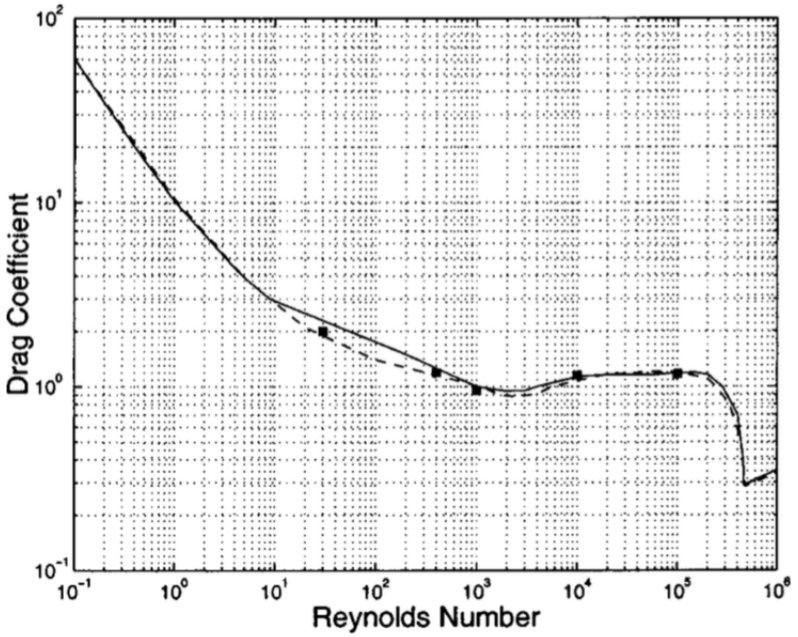

Figure 2–2: Drag coefficient as a function of Reynolds number. • Numerical results from Schulz and Kallinderis (2000); — Experimental results from Wieselsberger (1921); - - Experimental results from Massey (1979). Figure taken from the work of Schulz and Kallinderis (2000).

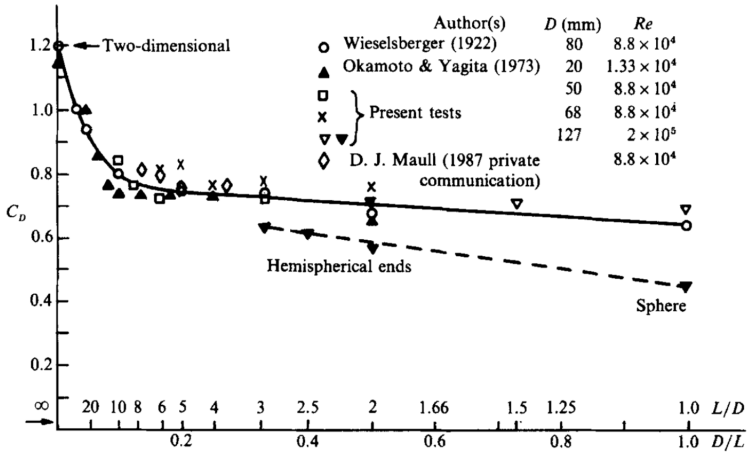

Figure 2–3: Drag coefficient for different aspect ratios (L/D) and Reynolds numbers. Taken from the work of Zdravkovich *et al.* (1989).

end, Allen and Vincenti (1944) published correlations that apply to a variety of shapes and account for compressibility in the flow at high Mach numbers (M). Dalton (1971) modified this approach specifically for cylinders in cross-flow, when compressibility effects are negligible

($M < 0.2$), and obtained the following result:

$$C_D = C'_D\left[1 - \frac{1}{4}(D/H)^2 - \frac{1}{2}(D/H)C'_D\right], \tag{2.2}$$

where C'_D is the measured drag coefficient, C_D is the corrected one, D is the cylinder diameter and H is the wind tunnel height for the case of a horizontal cylinder.

The drag on circular cylinders can also be influenced by the end conditions. When a cylinder has one or both ends free in the flow, three-dimensional flow along the span is induced (Zdravkovich 1997b). In the case of a cylinder that spans the cross-section of a wind tunnel, the wall boundary-layers separate around the cylinder and roll upstream, creating a "horseshoe swirl system" (Zdravkovich 1997b). By adding plates at each end of the cylinder, the boundary layers become very thin, and three-dimensional effects are minimized (Stansby 1974). There have been numerous investigations concerning the optimal shape and size for end plates. Kubo *et al.* (1989), using circular end plates with different diameters, found that the ratio of the end-plate diameter to the cylinder diameter had to be at least 8 for the effects on C_D to be minimal. Stansby (1974) found that square end plates with sides 7 times the cylinder diameter in length rendered the flow almost completely two-dimensional along its axis. He also found that the addition of end plates reduces the base pressure along the cylinder (i.e., the pressure 180° from the front stagnation point), therefore increasing C_D.

Finally, another parameter that may influence C_D on circular cylinders is the free-stream turbulence intensity T_i, which is defined as:

$$T_i \equiv \frac{u_{rms}}{\overline{U_\infty}}, \tag{2.3}$$

where u_{rms} is the root-mean-square average of the fluctuating part of the velocity, and $\overline{U_\infty}$ is the mean free-stream velocity. The free-stream turbulence intensity in the above-mentioned studies was in the range of $0.1\% \leq T_i \leq 0.7\%$, however the effects of these levels of turbulence on C_D have not been fully investigated. Moreover, in many publications on the drag on circular cylinders, T_i is not reported.

Because of the aforementioned effects of the aspect ratio, wind-tunnel blockage, end conditions, and free-stream turbulence intensity, particular care must be taken when comparing published values for C_D. Table 2–1 summarizes measured drag coefficients on smooth cylinders in cross-flow with low free-stream turbulence from prior published experiments with similar Reynolds numbers as those in this study. Not all results are corrected for blockage, and not all values of the free-stream turbulence are reported. It is clear, however, that the results exhibit a certain degree of variability for the same range of Reynolds numbers, depending on the parameters listed above.

The work of Norberg (1987) and Delany and Sorensen (1953) , being undertaken at Reynolds numbers at the lower and upper ranges, respectively, of those used in the present experiments, and with similar end conditions, will serve as a useful comparison with results of the present work (to be discussed in §4.2). It must, however, be noted that the aspect ratios of the cylinders used in their experiments, 80 and 28, respectively, are higher than those in this project ($L/D = 12$). The results of Okamoto and Yagita (1973), for cylinders with similar L/D as the present work, and with experiments at Reynolds numbers at the upper end of the range of Re_D in the present work, may also be useful for comparison; however, they have different cylinder end conditions.

2.2.2 Effect of Free-Stream Turbulence

Fage and Warsap (1929) were among the first researchers to observe that increasing the free-stream turbulence intensity (T_i) accelerated the transition to turbulence, decreased $Re_{D,crit}$, and shifted the C_D versus Re_D curves to the left. This trend has also been observed in the works of Arie *et al.* (1981) and Cheung and Melbourne (1983).

It is not clear how T_i affects C_D in the subcritical range, as there is wide scatter in the published results. For example, a study by Norberg (1987), in which $Re_D = 3000$ and 8000, exhibited an increase in C_D as T_i was increased from 0.1% to 1.4%. Ko and Graf (1972), who studied the drag over a cylinder for $1300 \leq Re_D \leq 8000$ and $1.3\% \leq T_i \leq 21.3\%$, found that C_D initially decreased with increasing T_i, reaching a minimum at $T_i \approx 4\%$;

and C_D then increased. And Arie *et al.* (1981), undertaking experiments in the ranges of $7900 \leq Re_D \leq 54000$ and $1\% \leq T_i \leq 15.8\%$, found that C_D decreased with increasing T_i.

The effect of the ratio of the longitudinal integral length scale (ℓ_x) of the background turbulence to the diameter is also unclear. The integral length scale is characteristic of the largest length scales in a turbulent flow. Arie *et al.* (1981) observed that C_D decreases with decreasing ℓ_x/D when $\ell_x/D < 1$, and is unaffected when $\ell_x/D > 1$. Ko and Graf (1972) found no clear trend between C_D and ℓ_x/D. Perhaps the best summary of the effects of ℓ_x/D can be found in the work of Bearman and Morel (1983), who stated: "As far as the length scale is concerned, increasing its ratio to characteristic body dimension sometimes increases the turbulence effects, sometimes it attenuates them, and in a number of cases it has been found to have no effect at all over a wide range of length scales."

To provide some physical explanations of the aforementioned observations, Bearman and Morel (1983) identified three mechanisms by which the free-stream turbulence can affect the

Source	Re_D	C_D	L/D	End conditions	T_i (%)	Corrected for Blockage
Wieselsberger (1921)	5000	1.00	> 280	2FE	-	no
Wieselsberger (1921)	20000	1.20	> 280	2FE	-	no
Wieselsberger (1922)	88000	0.80	10	2FE	-	no
Fage and Warsap (1929)	47000	1.08	17	2WA	-	no
Fage and Faulkner (1931)	60000	1.19	16	2WA	-	no
Delany and Sorensen (1953)	18000	1.00	28	2EP	-	yes
Achenbach (1968)	40000	1.24	3	2WA	0.7	no
Okamoto and Yagita (1973)	13300	1.00	13	1FE, 1EP	0.25	no
Sadeh and Saharon (1982)	54000	1.00	31	2EP	0.56	yes
Norberg (1987)	8000	1.13	80	2EP	0.1	no
Zdravkovich *et al.* (1989)	88000	0.83	10	2FE	0.3	no
Klausmann and Ruck (2017)	40000	1.24	10	2EP	< 1	yes

Table 2–1: Summary of C_D results from different publications. T_i = Free-stream turbulence intensity, FE = free end, WA = adjacent to wall, EP = end plates.

flow over bluff bodies: i) acceleration of the transition to turbulence, ii) enhanced mixing and entrainment, and iii) distortion of the turbulence itself by the mean flow. A possible reason for the scatter in published results is that more than one of these mechanisms were acting at the same or different locations in the flow.

Studies on the turbulent wakes downstream of bluff bodies, without explicitly measuring the drag, can also give an indication of how free-stream turbulence affects the flow around such bodies. For example, Rind and Castro (2012b) measured the turbulent wake downstream of an axisymmetric disk placed with its axis parallel to the flow, and observed that the presence of free-stream turbulence in the flow enhanced the momentum deficit in the wake, which is associated with an increase in the drag. Eames *et al.* (2011) noted that the growth of a wake behind a cylinder in cross-flow is affected by the ratio of the integral length to the size of the wake. Other notable works in this field include Wu and Faeth (1994, 1995), Rind and Castro (2012a), and Pal and Sarkar (2015a,b). Finally, the effects of background turbulence in other free-shear flows may also be relevant, e.g.: Khorsandi *et al.* (2013).

To summarize, it is clear that more research on the effects of turbulence intensities and length scales on the drag on circular cylinders in cross-flow are required for conclusions to be drawn with greater confidence.

2.2.3 Effect of Porous Outer Layers

Until now, studies on solid cylinders with porous outer layers were mostly focused on applications in vibration damping (Bhattacharyya and Singh 2011) or heat transfer (Sobera *et al.* 2003). The few investigations of the drag on solid cylinders with porous outer layers have been mostly numerical in nature.

Bhattacharyya and Singh (2011) studied the flow over a solid cylinder with a porous outer layer in cross-flow using numerical simulations, and found that the porous layer reduced the drag, when compared to a solid cylinder with no porous outer layer. In another numerical study, Bruneau and Mortazavi (2006) observed that C_D either increased or decreased depending on the porosity of the outer layer.

In an attempt to induce drag reductions on the flow over bluff bodies, Klausmann and Ruck (2017) experimentally studied the flow over cylinders with a porous outer layer on a part of the leeward side of the cylinder (between 40 and 160 degrees), as shown in Figure 2–4. They chose a partial coating because preliminary tests on fully coated cylinders exhibited an increase in C_D. They observed that the partial porous layer increased the base pressure on the leeward side of the cylinder, leading to a decrease in C_D of up to 13%, when compared to a smooth cylinder.

Watanabe *et al.* (1989, 1991) conducted wind tunnel experiments on solid cylinders surrounded by different (porous) fabrics. They observed that the presence of such fabrics caused the separation point to move forward, towards the front stagnation point on the cylinder. Though their study did not include drag measurements, a reduction of the separation angle is related to an increase in C_D, due to an increase in form drag (Bearman and Morel 1983).

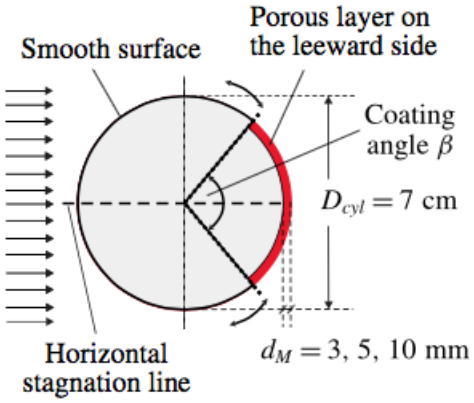

Figure 2–4: Schematic of a cylinder with a partial porous outer layer. Taken from the work of Klausmann and Ruck (2017).

2.3 Turbulence

The majority of flows occurring in both nature and engineering applications are turbulent, including the atmospheric boundary layer, the Gulf Stream in the ocean, and wakes behind bluff bodies (Tennekes and Lumley 1972). In general, no complete, precise definition of turbulence exists; therefore, to describe it, many authors have chosen to describe its universal properties. To this end, one can observe that turbulence is random, is diffusive, has

three-dimensional vorticity fluctuations, occurs at large Reynolds numbers, and contains a range of scales. In addition, it is dissipative by nature, and requires a continuous input of energy to balance this dissipation if the turbulence is to be sustained.

In mathematical terms, the flow of a Newtonian fluid with constant properties is governed by the following form of the Navier-Stokes equations (Pope 2000):

$$\rho\frac{D\tilde{u_i}}{Dt} = \mu\frac{\partial^2\tilde{u_i}}{\partial x_j \partial x_j} - \frac{\partial P}{\partial x_i} - \rho\frac{\partial \Psi}{\partial x_i}, \tag{2.4}$$

where $\tilde{u_i}$ is the instantaneous velocity, μ is the dynamic viscosity, P is the static pressure, Ψ is a gravitational potential, and repeated indices imply summation. D/Dt is the material derivative, defined as:

$$\frac{D}{Dt} = \frac{\partial}{\partial t} + \tilde{u_j}\frac{\partial}{\partial x_j}. \tag{2.5}$$

Given the random nature of turbulent flows, it is logical to consider average values of its properties. To this end, it is common practice to apply the Reynolds decomposition, in which the instantaneous properties of the flow (i.e., velocity, pressure, etc.) are decomposed into mean and fluctuating components. For the velocity, this decomposition is as follows:

$$\tilde{u_i} = \overline{U_i} + u_i, \tag{2.6}$$

where $\tilde{u_i}$ is the instantaneous velocity in a particular direction, and $\overline{U_i}$ and u_i are its mean and fluctuating components, respectively. Applying this decomposition to the Navier-Stokes equation yields the Reynolds-Averaged Navier-Stokes equations (RANS), which have more unknowns than equations and therefore cannot be solved; this is referred to as the closure problem (Tennekes and Lumley 1972).

Moreover, it is also of interest to study the statistics of the fluctuations about their aforementioned mean value, as discussed in Pope (2000). Once again using the velocity as an example, one can quantify the magnitude of the fluctuations by the variance of the fluctuating component of velocity ($\overline{u^2}$) or it root-mean-square value ($u_{rms} \equiv (\overline{u^2})^{1/2}$). The variance of the velocity fluctuations is directly related to the turbulent kinetic energy (TKE) of the flow

as follows:

$$TKE \equiv \frac{1}{2}\overline{u_i u_i}. \tag{2.7}$$

Another characteristic of turbulence is that it is dissipative by nature; the rate of dissipation of TKE per unit mass, commonly referred to as the energy dissipation rate, ϵ, is defined as (Tennekes and Lumley 1972):

$$\epsilon \equiv 2\nu\overline{s_{ij}s_{ij}}, \tag{2.8}$$

where s_{ij} is the fluctuating rate of strain:

$$s_{ij} \equiv \frac{1}{2}\left(\frac{\partial u_i}{\partial x_j} + \frac{\partial u_j}{\partial x_i}\right). \tag{2.9}$$

Turbulence is referred to as statistically homogeneous if it is invariant to translations of the coordinate system, and statistically isotropic if it is invariant to rotations and reflections of the coordinate system (Pope 2000). For the case of homogeneous, isotropic turbulence, the energy dissipation rate is:

$$\epsilon = 15\nu\overline{\left(\frac{\partial u_1}{\partial x_1}\right)^2}. \tag{2.10}$$

Since it is impractical to measure $\partial u_1/\partial x_1$ in laboratory conditions, the energy dissipation rate is frequently measured in terms of $\partial u/\partial t$. Using Taylor's hypothesis, which states that if the turbulence intensity is not overly large ($T_i \lesssim 20\%$), the turbulence does not substantially deform as it is convected past a point in space, the derivative with respect to position can be related to the derivative with respect to time, $\frac{\partial}{\partial x} = -\frac{1}{\overline{U}}\frac{\partial}{\partial t}$ (Tennekes and Lumley 1972; Pope 2000). Thus the equation for ϵ becomes:

$$\epsilon = 15\nu\frac{1}{\overline{U}^2}\overline{\left(\frac{\partial u}{\partial t}\right)^2}. \tag{2.11}$$

As mentioned above, turbulence exhibits a range of scales of various quantities. At the upper bound, the length scales are dictated by the geometry of the flow field. The integral length scale (ℓ) is characteristic of the largest eddies in the flow, and the root mean-square of

the fluctuating component of velocity (u_{rms}) is the characteristic velocity of these large-scale fluctuations. An integral timescale can be determined from these: $\mathcal{T} = \ell/u_{rms}$.

The integral length scale can be calculated from the spatial autocorrelation of the velocity fluctuations as follows (Pope 2000):

$$\ell = \int_0^\infty \rho(r)dr, \tag{2.12}$$

where $\rho(r)$ is the two-point spatial autocorrelation coefficient of the velocity fluctuations, $\rho(r) \equiv \frac{\overline{u(x)u(x+r)}}{u_{rms}}$, and r is the distance between two points. Using Taylor's hypothesis, the spatial autocorrelation can be related to the temporal autocorrelation as follows:

$$\ell = \overline{U} \int_0^\infty \rho(\tau)d\tau, \tag{2.13}$$

where $\rho(\tau)$ is the one-point temporal autocorrelation coefficient of the velocity fluctuations, $\rho(\tau) \equiv \frac{\overline{u(t)u(t-\tau)}}{u_{rms}}$, and τ is the time lag of the correlation (Tennekes and Lumley 1972).

The TKE is not dissipated at the large scales; there exists an energy cascade in which kinetic energy is transferred from the largest eddies to smaller and smaller eddies until reaching scales so small that the TKE is "dissipated" by viscosity (i.e., converted into internal energy). These scales are the Kolmogorov microscales; they represent the smallest scales in the flow, and are uniquely defined by the energy dissipation rate (ϵ) and the kinematic viscosity (ν). From dimensional analysis, the Kolmogorov microscales of length, time and velocity are defined, respectively, as (Tennekes and Lumley 1972):

$$\eta \equiv (\nu^3/\epsilon)^{1/4}, \qquad \tau \equiv (\nu/\epsilon)^{1/2}, \qquad \upsilon \equiv (\nu\epsilon)^{1/4}. \tag{2.14}$$

An intermediate length scale that is often used in the study of turbulence is the Taylor microscale λ, which can be calculated from the following equation (Tennekes and Lumley 1972):

$$\overline{\left(\frac{du_1}{dx_1}\right)^2} = \frac{\overline{u_1^2}}{\lambda^2}. \tag{2.15}$$

It is used as a length scale in the definition of a turbulent Reynolds number, often used to quantify turbulent flows, as follows:

$$R_\lambda \equiv \frac{u_{rms}\lambda}{\nu}. \tag{2.16}$$

Combining Equations 2.10 and 2.15, and noting that for homogeneous, isotropic turbulence, $\overline{u_1^2} = u_{rms}^2$, the Taylor microscale can be related to the energy dissipation rate in the following way (Tennekes and Lumley 1972):

$$\epsilon = 15\nu\frac{u_{rms}^2}{\lambda^2}. \tag{2.17}$$

2.3.1 Atmospheric Turbulence

Atmospheric turbulence is generally more complex than canonical flows generated in laboratory experiments, because i) the turbulence in the earth's boundary layer is generated from a combination of shear and buoyancy effects, and ii) the flow outside the boundary layer is strongly affected by the rotation of the earth.

The heating of the earth's surface during the day and the shear force on it from winds causes a vertical transport of momentum, heat and moisture (from the earth's surface). The height of the boundary layer is dictated, in part, by the temperature distribution with height. In stably stratified flow, the temperature increases with height, and instabilities are dampened by buoyancy forces; this is the case on a clear night with low winds. On a typical sunny day, temperature decreases with height (unstable stratification); in this case, the buoyancy forces amplify the instabilities, generating a boundary layer that is much larger.

To accurately study the flight of firebrands in the atmosphere, it is important to quantify atmospheric turbulence. Counihan (1975) reviewed different investigations of atmospheric turbulence and summarized their properties, including turbulence intensities, integral length scales (in the direction of the prevailing wind), heights of the boundary layer, and mean velocity profiles, for rural and urban areas. Some key properties near the ground are summarized in Table 2–2. As will be shown in Chapter 4, an active grid can be used to generate

turbulence intensities similar to those observed in the atmosphere. However, the ratio of integral length scales to firebrand size (diameter) in the atmosphere is on the order of $10^3 - 10^4$; to achieve such a ratio in laboratory experiments would require either an impractically large wind tunnel, or a very thin cylinder (and therefore a capability to measure very small forces).

Property	Rural	Urban
Turbulence intensity T_i (%)	10-20	20-35
Integral length scale ℓ_x (m)	10-100	100-200
Boundary layer height (m)	400-700	500-800

Table 2–2: Properties of atmospheric turbulence near the ground, from the work of Counihan (1975).

2.3.2 Grid Turbulence

Early experimental studies on turbulent flows generated turbulence by placing a grid of horizontal and vertical bars in a wind tunnel, upstream of the test section. With such grids, the turbulence becomes effectively homogeneous and isotropic ($u_{rms}/v_{rms} \approx 1.1$) far enough downstream of the grid ($x/M \gtrsim 30$, where M is the mesh length of the grid; Gad-el-Hak and Corrsin 1974). However, turbulence generated by such grids (except, for rare exceptions, generated by impractically large ones), is typically characterized by low Re_λ ($50 \lesssim Re_\lambda \lesssim 150$), making them unsuitable for modelling atmospheric or other highly turbulent flows (Mydlarski 2017). Some notable works using passive grids include the works of Simmons and Salter (1934), Stewart and Townsend (1951), and Comte-Bellot and Corrsin (1966, 1971).

A breakthrough in grid-generated turbulence was achieved by Makita (1991), who designed the first active grid, depicted in Figure 2–5. The active grid is composed of agitator wings attached to rotating grid bars, controlled by stepper motors that rotate the grid bars back and forth, independently and randomly, creating a flapping motion. Using this grid, Makita (1991) achieved a Re_λ close to 400 − one order of magnitude higher than that which would have been achieved using a passive grid with the same mesh length (Mydlarski 2017). The flow generated by the active grid also exhibited increased integral length scales, and

a high degree of homogeneity. The only drawback was a slight reduction in the isotropy compared to passive grids ($u_{rms}/v_{rms} \approx 1.2$) (Mydlarski 2017).

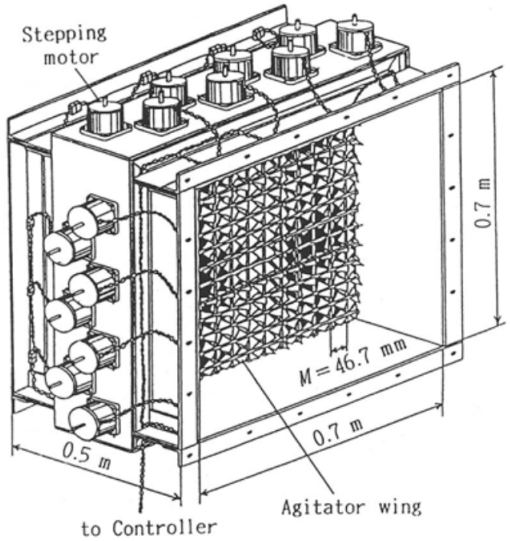

Figure 2–5: Schematic of an active grid. Taken from the work of Makita (1991).

Following this work, Mydlarski and Warhaft (1996, 1998) used a Makita-style active grid to generate homogeneous, isotropic turbulence with a Re_λ of up to 730. Larssen and Devenport (2011) placed an active grid in the contraction of a wind tunnel (upstream of the test section) to improve the isotropy of the flow, achieving results as low as $u_{rms}/v_{rms} \approx 1.02$. They also generated the highest Taylor-microscale Reynolds number and integral length scales to date, with values of 1362 and 67cm, respectively. In an attempt to study active-grid operating parameters, Hearst and Lavoie (2015) did an extensive parametric study on the effects of the mean wing angular velocity, mean flow velocity, wing geometries, and other factors on the turbulence generated by an active grid. They found that the parameters having the greatest influence on the turbulence are the Rossby number ($Ro \equiv U/\Omega M$, where Ω is the mean angular velocity of the agitator wings), the grid Reynolds number ($Re_M \equiv UM/\nu$), and the wing blockage ratio.

In a review article on active grids, Mydlarski (2017) noted that the algorithms used to operate active grids fall into three general categories: i) synchronous mode, in which the angular velocity Ω of each grid bar is equal, but adjacent grid bars are rotated in opposite

directions; ii) single-random asynchronous mode (single-random mode), in which each grid bar rotates at either Ω or $-\Omega$ for a random duration of time (ΔT), after which it changes direction for a new randomly selected duration of time; and iii) double-random asynchronous mode (double-random mode), in which both Ω and ΔT take on new random values after each direction change. For the study of homogeneous, isotropic turbulence, double-random mode is the preferred method of operation, as it produces the most intense turbulence with minimal contamination of the velocity field from the grid bar rotation rates.

2.3.3 Hot-Wire Anemometry

Hot-wire anemometry (HWA) is an important research tool for the study of turbulent flows. Some of the main benefits of HWA include a: i) high spatial resolution, and therefore the ability to quantify the smallest of scales in the flow, ii) high frequency response, allowing measurements of up to several kilohertz, and iii) high signal-to-noise ratio (Bruun 1987).

The principle of operation of hot-wire anemometers is based on the convective heat transfer from a heated wire placed in a flow. The wire is heated by passing an electrical current through it. In Constant Temperature Anemometers (CTA), the current in the wire is modified to maintain it at a constant resistance (and therefore temperature). The CTA keeps the hot-wire at an operating resistance (R_{op}) above that of the resistance of the wire at the ambient temperature (R_a) by a factor called the overheat ratio. For tungsten wires, an overheat ratio (R_{op}/R_a) of 1.8 is generally used. The CTA outputs a voltage that is directly related to the power required to maintain the wire at this temperature (equal to the heat transfer from the wire, ignoring the thermal inertia of the wire for unsteady flow measurements), which can be related to the velocity of the flow using King's Law:

$$E^2 = A + BU^n, \tag{2.18}$$

where U is the velocity over the wire, and A, B, and n are constants that are determined by calibration (Bruun 1987).

To account for small variations in R_a, which would require re-calibration, Medvescek *et al.* (2014) used a modified King's law in which the power supplied to the hot-wire (E^2/R_{op}) was calibrated as a function of the velocity:

$$\frac{E^2}{R_{op}} = A + BU^n, \tag{2.19}$$

where A, B and n are different calibration constants.

CHAPTER 3
Experimental Apparatus and Techniques

Descriptions of the experimental apparatus (including the wind tunnel; passive and active grids; hot-wire anemometer; wind tunnel balance; data acquisition system; and cylinders, without and with porous outer layers) and techniques are presented and discussed in this chapter.

3.1 Wind Tunnel

Details of the setup of the wind tunnel, characterization of the flow in it, and the grids used to generate turbulence are presented in this section.

3.1.1 Overall Setup

A wind tunnel was gifted to Professor Mydlarski by Professor Warhaft of Cornell University, and was transported to McGill University in pieces. Before the present experiments could be performed in this wind tunnel, the following steps had to be undertaken:

1. An appropriate blower had to be selected, acquired and installed.
2. A support structure for the wind tunnel had to be designed and built.
3. The wind tunnel had to be assembled, ensuring each part was level.
4. The flow in the test section of this wind tunnel had to be characterized.

The main constraint when selecting the blower for this wind tunnel was its (physical) size. Since the Aerodynamics Laboratory is located on the first floor (above the ground floor) of the Macdonald Engineering Building at McGill University, the chosen blower had to be small enough to fit inside the building's elevator, while still having enough power to meet the air-flow requirements of this project. The selected blower is a Cincinnati HDBI-240 model with a 10 horsepower motor, controlled with a variable frequency drive (ABB ACH550-UH). The blower and motor specifications are summarized in Table 3–1. To reduce operating noise, a muffler was also purchased and installed at the inlet of the blower. To reduce vibrations

from the blower and muffler, both were mounted on damping pads, and fastened to the floor of the laboratory.

Property	Value
Model	Cincinnati HDBI-240
Variable frequency drive	ABB ACH550-UH
Motor power (hp)	10
Maximum air flow (m^3/s)	3.2
Maximum static pressure difference (Pa)	1692
Maximum motor speed (rpm)	1770
Fan diameter (m)	0.62
Maximum static efficiency (%)	72.7

Table 3–1: Specifications of the wind-tunnel blower.

The wind tunnel is of open-circuit design, and the following parts of it are located downstream of the blower, in the order given: i) a transition section to connect the blower outlet to the flow-conditioning inlet (which are of different cross-sectional geometries), ii) the flow-conditioning section, and iii) the test section. The transition section diverges slightly in the horizontal plane, and contracts in the vertical plane, to connect the blower outlet (0.427m×0.695m) to the flow-conditioning inlet (0.470m×0.200m). The flow-conditioning section includes a diffuser, a settling chamber, and a 9:1 area ratio contraction. Screens in the settling chamber reduce the background turbulence by breaking up large turbulent eddies (coming from the blower) into smaller ones that decay more rapidly (Cattafesta *et al.* 2010). The contraction serves to further reduce the levels of background turbulence in the wind tunnel. The 0.407m×0.407m×4.5m long test section follows. The top wall of the test section diverges slightly in the vertical plane to maintain a constant centreline velocity in the wind tunnel by offsetting boundary-layer growth on the tunnel walls. A honeycomb at the end of the test section ensures that external perturbations to the flow inside the test section are minimized. A schematic of the wind tunnel is presented in Figure 3–1, and photographs of the fully-assembled wind tunnel are presented in Figure 3–2.

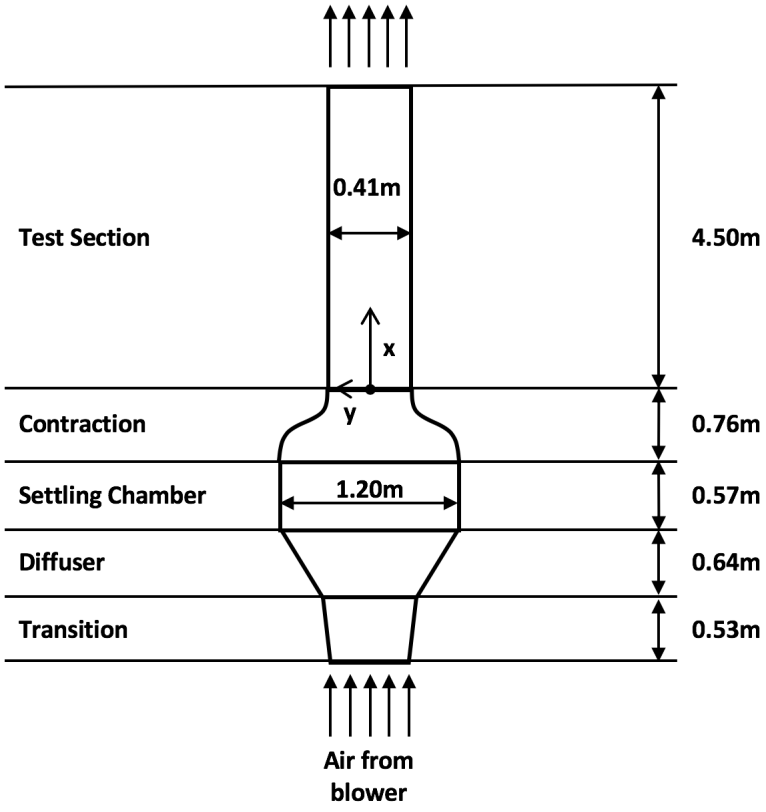

Figure 3–1: Schematic of the wind tunnel in the horizontal plane (top view, not to scale), indicating the coordinate system used in the test section (the z-coordinate, normal to x, y, points vertically upward, starting at the centreline of the wind tunnel).

A structure was designed and built to support the tunnel, using aluminum Unistrut parts (it can be seen in Figure 3–2). During assembly, each part of the tunnel was carefully leveled to minimize discontinuities at the interfaces between its sections. To minimize vibrations of the wind tunnel, and also facilitate its assembly and disassembly, threaded inserts were installed in the floor, such that the supporting frame could be easily bolted to the floor.

3.1.2 Flow Characterization

The x-direction velocity profiles in the test section of the wind tunnel were measured to validate the homogeneity of the flow. With reference to the coordinate system shown in Figure 3–1, three vertical (y = -4" (0.102m), 0", 4" (0.102m)) and three horizontal profiles (z = -4" (0.102m), 0", 4" (0.102m)) were measured, at three different downstream locations (x = 0.92m, 2.32m, and 4.32m), for a total of 18 profiles, with no grid installed. Furthermore,

Figure 3–2: Downstream and upstream views of the wind tunnel.

one vertical ($y = 0$) and one horizontal ($z = 0$) profile were measured at two downstream locations ($x = 2.32$m, and 4.32m) for the following cases: i) 1" passive grid, ii) 2" passive grid, and iii) active grid (these grids are described in Section 3.1.3). For each velocity profile, measurements were made at 15 points evenly spaced at 1" (0.0254m) intervals between the tunnel walls. Statistical moments of the velocity were also calculated at each of these points.

To quantify the decay of turbulence, the mean velocities and moments were measured at 10 downstream locations along the centreline of the tunnel for the following cases: i) 1" passive grid, ii) 2" passive grid, and iii) active grid. The results of the flow characterization are presented in §4.1.

To measure the x-direction velocity profiles, a TSI 1210 single-hot-wire probe was attached to a TSI 1155-18 probe support (covered by a TSI 1160 probe shield) and a TSI 1152 elbow, and inserted into the flow through different ports along the bottom and side faces of

the tunnel. The probe support was slid along the y- or z-direction to the selected measurement points. A photograph of the hot-wire probe, probe support and elbow is presented in Figure 3–3.

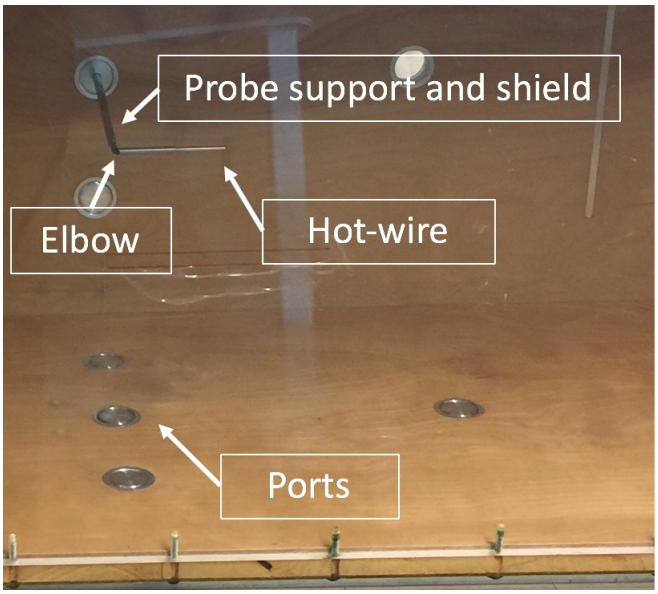

Figure 3–3: The hot-wire probe in the wind tunnel.

3.1.3 Grids

Four different levels of free-stream turbulence intensity were investigated in this study. The first level corresponded to the residual background turbulence in the tunnel with no grid installed. The three other levels of turbulence intensities were generated by: i) a 1" passive grid, ii) a 2" passive grid, and iii) an active grid. Photographs of the grids are presented in Figure 3–4. In the case when no passive grid was present in the tunnel, an empty frame filled the gap normally occupied by the passive grids, to prevent the gap in the tunnel wall from disturbing or altering the air flow. This frame was also used when the active grid was in place, as shown in Figure 3–4(c).

Passive Grids

As previously noted, two passive grids, with mesh lengths of 1" (0.0254m) and 2" (0.0508m), were installed in the wind tunnel to generate different intensities of free-stream turbulence. The grids are composed of vertical and horizontal bars of square cross-section,

(a) 1" passive grid (b) 2" passive grid (c) active grid

Figure 3–4: Photographs of the a) 1" passive grid, b) 2" passive grid, and c) active grid.

arranged in a bi-planar configuration normal to the direction of the main flow. The grids can be easily installed (and removed) by opening up the top of the tunnel and sliding them into (or out of) a slot at the upstream end of the test section. The properties of the grids are summarized in Table 3–2. In this table, solidity is defined as the ratio of the projected solid area to the projected total area.

Property	Passive grid 1"	Passive grid 2"	Active grid
Bar shape	Square	Square	Round
Bar width (diameter) (cm)	0.48	0.96	0.64
Number of bars	15×15	7×7	7×7
Mesh length M (cm)	2.54	5.08	5.08
Solidity (%)	34	34	n/a

Table 3–2: Properties of passive and active grids.

Active Grid

The active grid is composed of 7 horizontal and 7 vertical aluminum grid bars, with 0.64cm-diameter circular cross-sections, fitted with 0.38mm thick square agitator wings. The mesh length between the grid bars is 5.08cm. Each rod is driven by a Superior Electric Slo-Syn stepper motor (5V, 5W) with 200 steps per revolution. A schematic of the active grid, taken from the work of Mydlarski and Warhaft (1996), is presented in Figure 3–5. Adjacent to the walls are static triangular wings, with holes to reduce the velocity deficit near the walls,

designed to improve the homogeneity of the flow. For the same reason, rotating wings near the wall also had holes drilled into them (Mydlarski and Warhaft 1996). Although Figure 3–4 seems to show holes in all rotating wings, it should be noted that the holes in the wings at the center of the grid were taped over, and thus, effectively solid, as depicted in Figure 3–5.

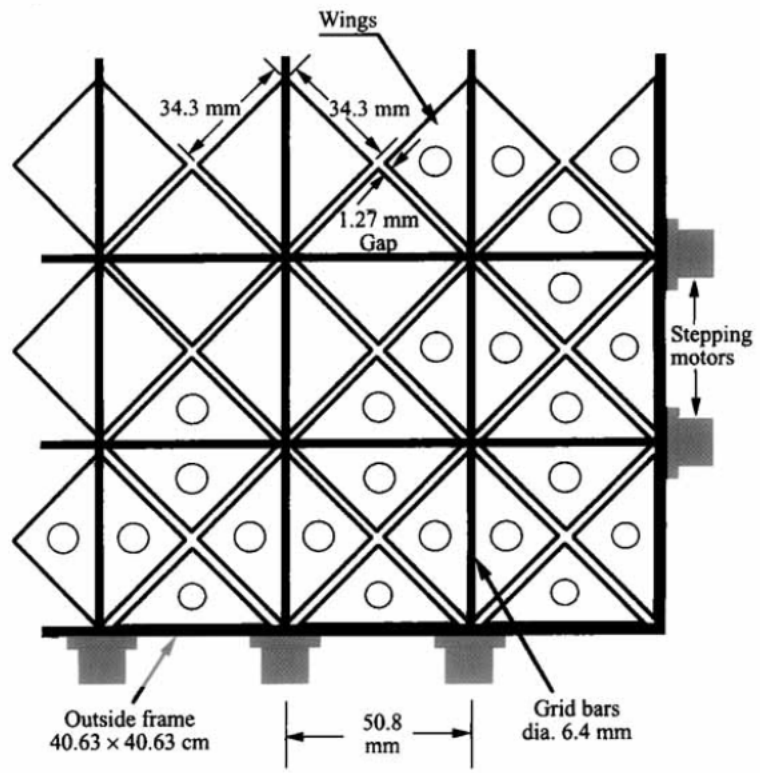

Figure 3–5: Schematic of the active grid, taken from the work of Mydlarski and Warhaft (1996)

As discussed in §2.3.2, the preferred method of operating an active grid for the study of homogeneous, isotropic turbulence is in the double-random mode. A controller was designed to operate the grid in such a mode, using a combination of different Arduino microcontrollers; the Arduinos were selected because of their relatively low cost and ease of configuration. Note that some of the microcontrollers selected for this project were from Elegoo, almost identical to their Arduino counterparts, but at lower cost. Top and side views of the active-grid controller are presented in Figure 3–6.

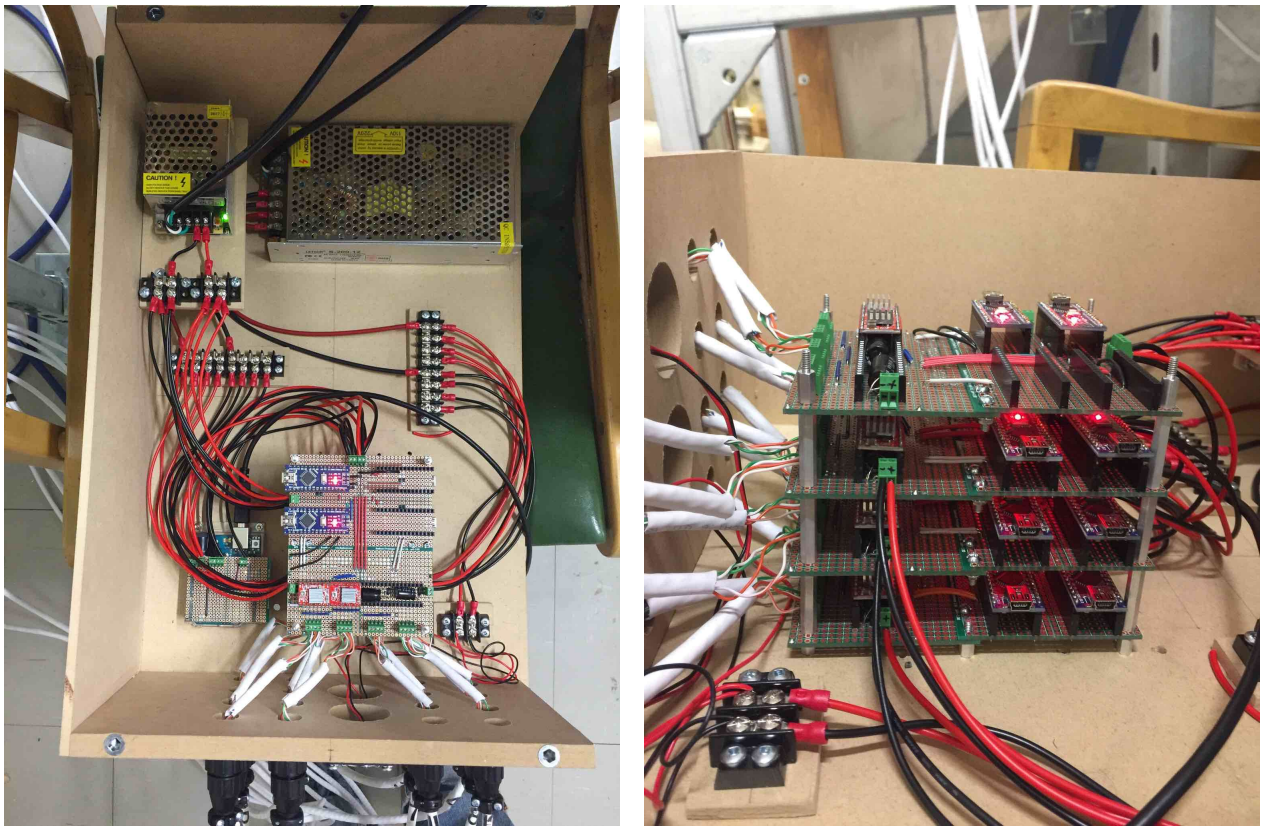

Figure 3–6: Top and side views of the active-grid controller.

The active-grid controller is composed of the following components:

1. Fourteen Elegoo Nanos (slaves), one for each stepper motor, referred to hereafter as slave Arduinos.
2. Fourteen Elegoo A4988 stepper-motor drivers.
3. One Arduino Uno, which can change the parameters of the slave Arduinos, referred to hereafter as the master Arduino.
4. One Yaetek S-36-12 D.C. power supply (12V, 36W) to provide power to the slave and master Arduinos.
5. One Letour S-200-12 D.C. power supply (12V, 200W) to provide power to the stepper motors and motor drivers.
6. Four protoboards (stacked), designed and constructed to provide connections between the slave Arduinos, motor drivers, stepper motors, and power supplies.

7. One protoboard, stacked on top of the master Arduino, designed and constructed to provide connections between the master and slave Arduinos.

The active-grid controller operates in the following manner: at the beginning of operation, each slave Arduino generates random numbers for the turning angle (Θ) and angular velocity (Ω), from the pre-determined ranges $[\Theta_{min}, \Theta_{max}]$ and $[\Omega_{min}, \Omega_{max}]$, presented below. The values for Θ and Ω are defined in steps, and steps per second, respectively, with 200 steps resulting in one complete revolution (360°). Each slave Arduino initializes the random-number generator with a different "seed", such that each sequence of random numbers is different. A third random number (0 or 1) is generated to define the initial direction. Once the direction, speed, and turning angle are set, the Arduino sends a square wave to the motor driver, which causes the stepper motor to move one step. The correct speed is attained by defining the period of each square wave, to a precision of one microsecond. A series of square waves are sent until the correct number of steps have been taken, after which two new random numbers are generated for the next values of Θ and Ω, and the direction is reversed.

Default ranges for $[\Omega_{min}, \Omega_{max}]$ and $[\Theta_{min}, \Theta_{max}]$ are summarized in Table 3–3; they are based on the work of Larssen and Devenport (2011) and Hearst and Lavoie (2015), as well as the capabilities of the stepper-motor drivers. These are hard-coded into the slave Arduinos; however, they can be changed with the master Arduino. The codes (programs) for the master Arduino and one of the slave Arduinos are presented in Appendix A, and the active grid operating procedure is presented in Appendix B.

Property	Minimum	Maximum
Θ $(steps)$	50	300
Θ (rev)	0.25	1.5
Ω $(steps/sec)$	200	500
Ω (rev/sec)	1	2.5
ΔT $(\equiv \frac{\Theta}{\Omega})$ (sec)	0.1	1.5

Table 3–3: Default ranges for active-grid operation.

3.2 Hot-Wire Anemometer

A DANTEC 55M10 Constant Temperature Hot-wire Anemometer (HWA) was used to measure the fluid velocity in the wind tunnel. A tungsten hot-wire of 5μm diameter was used as the sensor. The hot-wire ambient (or cold) resistance (R_a) was measured before each test, and the operating resistance (R_{op}) was selected such that the overheat ratio (R_{op}/R_a) was 1.8.

Initially, the hot-wire was calibrated using King's law, by which the square of the output voltage (E^2) from the HWA is determined as a function of the velocity for a given operating resistance ($E^2 = A + BU^n$). However, small variations in R_a (and therefore R_{op}) between tests, due to changes in the ambient-air temperature and/or aging of the hot-wire, produced changes in E^2 for the same velocity, requiring the hot-wire to be frequently recalibrated. To account for these changes in R_a, a modified King's law was used, whereby the power supplied to the HWA (E^2/R_{op}) was used (instead of E^2) and calibrated as a function of the velocity, based on the work of Medvescek *et al.* (2014). This approach enabled the same calibration to be used for different values of R_{op}, for the conditions encountered in this work, and reduced the effects of small changes in the ambient-air temperature and other factors causing drift of the hot-wire resistance.

Nevertheless, some drift in the data is inevitably observed between different calibration runs. To further account for this drift, the hot-wire was calibrated both before and after each series of tests, and the results were recast using the average constants from these two calibrations. A typical set of calibration curves, before and after a series of runs, is presented in Figure 3–7, with the corresponding calibration constants summarized in Table 3–4. Slight changes in the measured velocity ($\sim$0.3m/s at 10m/s, for example) can be observed between the first and second calibration curves, for the same value of E^2/R_{op}.

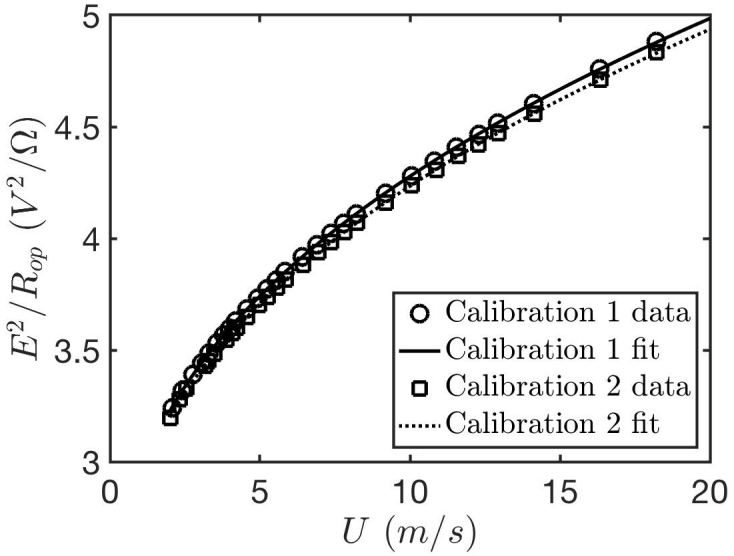

Figure 3–7: Typical hot-wire calibration curves before and after a series of experiments.

Property	Calibration 1	Calibration 2
Ambient resistance R_a (Ω)	2.49	2.50
Operating resistance R_{op} (Ω)	4.48	4.50
Calibration constant A	2.0669	2.1059
Calibration constant B	0.8800	0.8259
Calibration constant n	0.4001	0.4112
Correlation coefficient R^2	1.0000	1.0000

Table 3–4: Typical hot-wire calibration constants before and after a series of experiments.

3.3 Wind Tunnel Balance

A Kineoptics WTB 3.0 wind tunnel balance (WTB) was used to measure the drag. In a typical configuration, its three load cells can be used to measure the drag, lift, and pitching moment. The load cells used in this work are Honeywell, model 31, rated to a range of ±250g. A photograph of the wind tunnel balance is presented in Figure 3–8.

3.3.1 Calibration

To calibrate the WTB, a screw was installed in the bracket on top of the balance, to which a nylon string was hooked and strung over a low-friction pulley. Gauge blocks, carefully weighed to a precision of ±0.01g, were hung from the string to provide loads of

Figure 3–8: Kineoptics WTB 3.0 wind tunnel balance.

0-100g, transmitting a static horizontal force to the balance. The resulting load-cell voltages were recorded, and a calibration curve was fit to the data for each load cell. A schematic of the WTB during calibration and drag measurement, including applied loads and reaction forces, is presented in Figure 3–9.

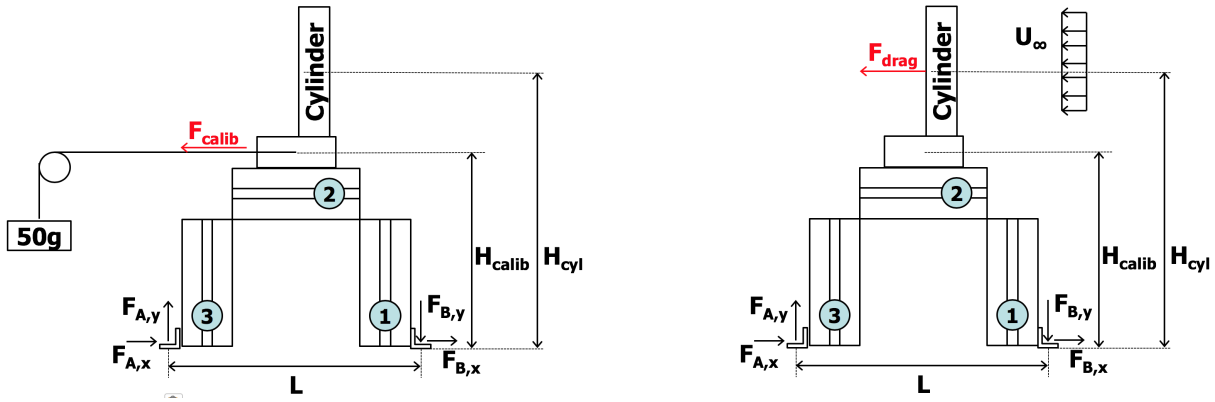

(a) Calibration (b) Measurement of drag

Figure 3–9: Schematic of the wind tunnel balance during (a) calibration, and (b) measurement of drag, where $H_{calib} = 0.230$m, $H_{cyl} = 0.641$m, and $L = 0.295$m.

In the schematic presented in Figure 3–9(a), the external forces on the WTB are the calibration load (F_{calib}), and the reaction forces at the supports ($F_{A,x}$, $F_{A,y}$, $F_{B,x}$, and $F_{B,y}$). The forces from the supports are transmitted to the three load cells in the following way: $F_1 = F_{B,y}$, $F_2 = F_{calib}$, and $F_3 = F_{A,y}$.

The forces $F_{A,y}$ and $F_{B,y}$ can be related to the calibration load by taking a sum of moments about points A and B:

$$\Sigma M_A = F_{calib}H_{calib} - F_{B,y}L = 0 \qquad \Rightarrow F_{B,y} = F_1 = \frac{H_{calib}}{L}F_{calib} \tag{3.1}$$

$$\Sigma M_B = F_{calib}H_{calib} - F_{A,y}L = 0 \qquad \Rightarrow F_{A,y} = F_3 = \frac{H_{calib}}{L}F_{calib} \tag{3.2}$$

Thus, the calibration constants relating the output voltage of the load cells to the above-mentioned forces can now be calculated as:

$$V_1 = a_1F_1 + b_1, \tag{3.3}$$

$$V_2 = a_2F_2 + b_2, \quad \text{and} \tag{3.4}$$

$$V_3 = a_3F_3 + b_3. \tag{3.5}$$

When measuring the drag on a cylinder, the drag force (assumed to be concentrated at the center of mass of the part of the cylinder between the two end plates) is not applied at the same location as the calibration force, as shown in Figures 3–9 (a) and (b). Thus, the voltage outputs from load cells 1 and 3 must be corrected to account for this difference. These relations can again be derived by taking a sum of moments about points A and B:

$$\Sigma M_A = F_{drag}H_{cyl} - F_{B,y}L = 0 \qquad \Rightarrow F_{B,y} = F_1 = \frac{H_{cyl}}{L}F_{drag} \tag{3.6}$$

$$\Sigma M_B = F_{drag}H_{cyl} - F_{A,y}L = 0 \qquad \Rightarrow F_{A,y} = F_3 = \frac{H_{cyl}}{L}F_{drag} \tag{3.7}$$

To compute the drag force, the voltage output from each load cell is compared to its no-load case ($V_{0,1}$, $V_{0,2}$, and $V_{0,3}$), and divided by the slope obtained during calibration (a_1, a_2, and a_3). Thus, the following relations are obtained:

$$F_{drag,1} = \frac{L}{H_{cyl}}\frac{\Delta V_1}{a_1}, \tag{3.8}$$

$$F_{drag,2} = \frac{\Delta V_2}{a_2}, \quad \text{and} \tag{3.9}$$

$$F_{drag,3} = \frac{L}{H_{cyl}}\frac{\Delta V_3}{a_3}, \tag{3.10}$$

where $F_{drag,1}$, $F_{drag,2}$ and $F_{drag,3}$ are the drag force as measured by load cells 1, 2, and 3, respectively, and ΔV_1, ΔV_2, and ΔV_3 are defined as:

$$\Delta V_1 = V_1 - V_{0,1}, \tag{3.11}$$

$$\Delta V_2 = V_2 - V_{0,2}, \quad \text{and} \tag{3.12}$$

$$\Delta V_3 = V_3 - V_{0,3}. \tag{3.13}$$

Typical calibration curves are depicted in Figure 3–10, with the corresponding calibration constants summarized in Table 3–5. During both calibration and measurement of drag, load cells 1 and 2 are in tension, while load cell 3 is in compression. It was found during preliminary tests that the load cells produce more repeatable results when under compression. Thus, load cells 1 and 2 were pre-compressed to ∼200g, while load cell 3 was pre-compressed to ∼100g, so that they would remain in compression for the full range of drag forces encountered in this work (10g $\lesssim F_{drag} \lesssim$ 70g). Note that even when no load is applied to them, the load cells have a non-zero voltage. It is for this reason, along with the pre-compression, that the intercepts of the calibration curves (b in Table 3–5) shown here are non-zero.

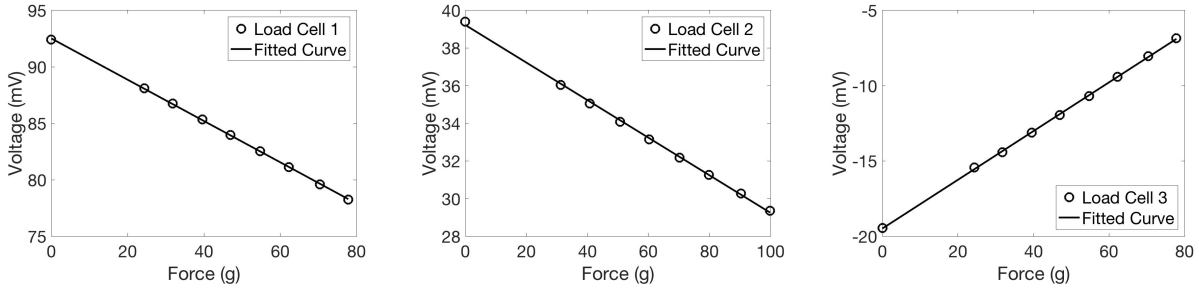

(a) Load Cell 1 (b) Load Cell 2 (c) Load Cell 3

Figure 3–10: Typical calibration curves for the wind tunnel balance.

Property	Load Cell 1	Load Cell 2	Load Cell 3
Slope a (mV/g)	-0.183	-0.100	0.162
Intercept b (mV)	92.5	39.2	-19.5
Correlation coefficient R^2	1.000	0.999	1.000

Table 3–5: Typical calibration constants for the wind tunnel balance.

3.4 Data Acquisition and Procedure

The output signals of the hot-wire anemometer (HWA) and the load cells from the WTB were digitized using a 16-bit National Instrument PCI 6143 data acquisition card and a BNC 2110 connector block, and recorded using custom-made LabVIEW programs. When measuring the velocity fluctuations, a Krohn-Hite 3382 filter was used to i) high-pass filter the signal from the hot-wire at 0.1Hz to remove the mean component, ii) low-pass filter the signal at the frequency at which it was determined that the HWA measures only noise, and iii) amplify the filtered signal to minimize the discretization error.

For the data obtained from the hot-wire anemometer, the filtered signal (used to calculate velocity fluctuations) consisted of a time series of 4.096×10^4 samples recorded at a rate of 400Hz, for a total sampling time of 1.7 minutes; the mean value of the signal was then computed with a data set of 1.024×10^4 samples recorded at a rate of 400Hz, for a total sampling time of 0.4 minutes. Many preliminary runs showed that these sampling parameters were satisfactory (gave statistically converged results).

When measuring the drag at mean velocities of 6, 8 and 10m/s, the data obtained from each load cell in the WTB consisted of data sets of 4.096×10^4 samples, recorded at a rate of 400Hz, for a total sampling time of 1.7 minutes. When the mean velocity was 4m/s, 1.2288×10^5 samples were recorded at a sampling rate of 400Hz, for a total sampling time of 5.1 minutes (This longer sampling time was required, given the lower vortex shedding frequency at this mean velocity, and therefore a longer period of oscillation of the cylinder). The number of samples for each data set was selected such that the measurements were statistically converged. This was determined by studying the evolution of the computed

statistics using incremental fractions of the full data set. At 4m/s, it was determined that longer sampling times were required to record sufficient vortex shedding cycles to obtain converged data.

Before a typical series of tests, the hot-wire and wind tunnel balance were calibrated. A zero reading of the wind tunnel balance was then recorded, to be compared to subsequent readings. The blower was turned on and set to a mean velocity of 4m/s in the test section, and this mean free-stream velocity was measured with the hot-wire at the tunnel centreline, upstream of the cylinder. The hot-wire probe was then moved to a position near the wall, to minimize interference with the air flow over the cylinder. The voltages from the WTB load cells were recorded, and compared to the zero readings to compute the drag force. The hot-wire was then slid back to the tunnel centreline to take a final velocity measurement. Using the average of the two velocity measurements, and the average of the drag forces measured with the three load cells, the drag coefficient was computed. This procedure was repeated at velocities of 6, 8 and 10m/s.

Note that the hot-wire ambient resistance (R_a) was measured before each test, and the hot-wire set to the desired operating resistance (R_{op}) using the specified overheat ratio (=1.8). The temperature of the air in the tunnel was also measured at the beginning and the end of each test using a thermocouple.

3.5 Smooth Cylinders

To benchmark the drag measurements using the WTB, a smooth aluminum cylinder, of 1" (0.0254m) diameter and 22" (0.559m) total length, was tested in different levels of free-stream turbulence. A ½" (0.0127m) threaded hole (½"-20 UNF thread) was made in the center of the bottom face of the cylinder, to fasten it to the wind tunnel balance. A ¼" (0.0064m) threaded hole (¼"-28 UNF thread) was made in the center of its top face, and used to lower the cylinder into the tunnel using a threaded rod. Photographs of the cylinder are presented in Figure 3–11. More details on how the cylinder is mounted in the wind tunnel can be found in §3.7.

(a) Side view

(b) Bottom view

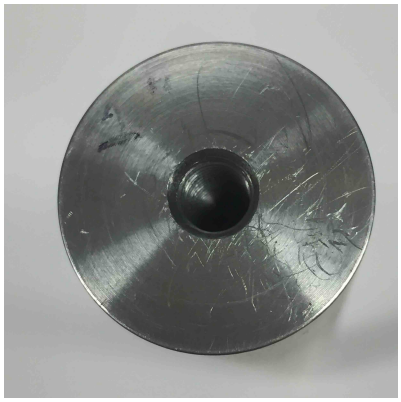

(c) Top view

Figure 3–11: Smooth cylinder, (a) side view, (b) bottom view, and (c) top view.

3.6 Cylinders with Porous Layers

Cylinders with porous outer layers were made by wrapping different wire meshes around solid aluminum cylinders. The solid cylinders were the same as the smooth cylinder described in §3.5, but with the upper 14" (0.356m) length machined to the appropriate diameter, such that the outer diameter of the porous layer, in all cases, was within 1 ± 0.05" (0.0254 ± 0.00127m). To achieve porous layer thicknesses of 1/4" (0.0064m), 1/8" (0.0032m), and 1/16" (0.0016m), the upper 14" (0.356m) length of the solid cylinders were machined to diameters of 1/2" (0.0127m), 3/4" (0.0191m), and 7/8" (0.0222m), respectively.

Three different steel wire meshes, purchased from McMaster-Carr, were used in this study. Photographs of the meshes are shown in Figure 3–12, and their properties are summarized in Table 3–6. In this table, solidity is defined as the ratio of the projected solid area to the projected total area, while open area refers to one minus the solidity.

The first step in making each of the cylinders with the porous outer layer was to cut the wire mesh to the appropriate width and length, then glue a thin strip of it to the solid

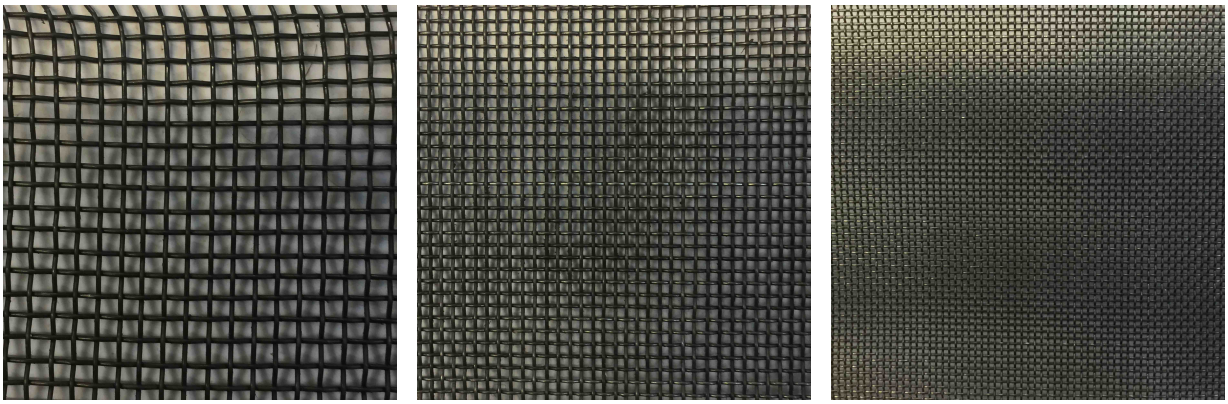

(a) Coarse - 10 PPI (b) Medium - 20 PPI (c) Fine - 40 PPI

Figure 3–12: Steel wire meshes used to make the porous outer layers.

Property	Coarse	Medium	Fine
McMaster-Carr product number	9219T176	9219T199	9219T956
Pores per inch PPI	10	20	40
Wire diameter (mm)	0.64	0.41	0.25
Open area (%)	56	46	36
Solidity (%)	44	54	64

Table 3–6: Properties of the steel wire meshes used to make the porous outer layers.

aluminum cylinders (the glue used was two-part Lepage Speed Set Professional Epoxy). To do so with precision, a jig was designed to hold the wire mesh tightly over the cylinder (over the upper 14" (0.356m) length, machine to the desired diameter), while a thin line of epoxy was applied from the top (through the mesh). To improve adhesion between the epoxy and the wire mesh, the surface of the cylinder was roughened with sandpaper. A cap was then screwed onto the top part of the cylinder to facilitate supporting and wrapping of the wire mesh over the cylinder. A picture of this gluing jig is presented in Figure 3–13(a).

The wire mesh was laid on top of the cylinder, and supported from either side of the cylinder axis, with the edge of the mesh set roughly 2" (0.0508m) past the axis of the cylinder. For easy removal of this extra length of wire mesh after gluing, it was pre-scored along a line with a utility knife parallel to the axis of the cylinder. The glue was applied adjacent to this

line. Once the glue was dry (24 hours), the extra length of wire mesh was bent back-and-forth along the pre-scored line until it broke off cleanly (along this line).

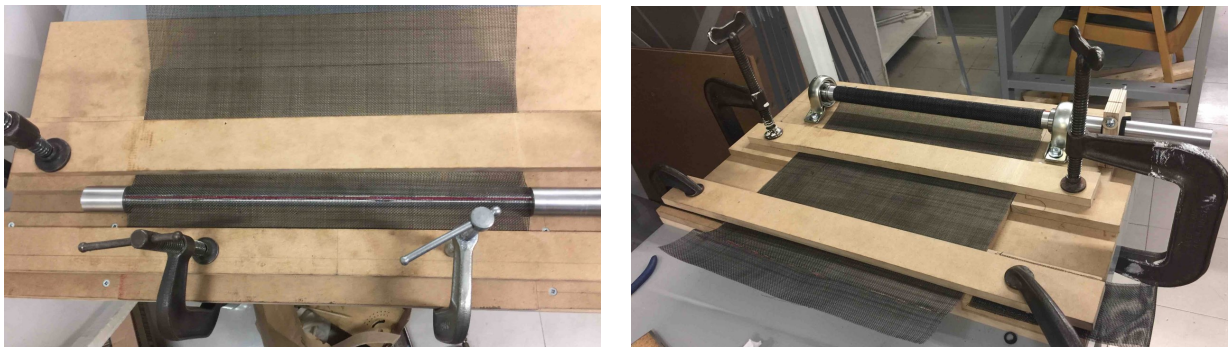

(a) Gluing jig (b) Wrapping jig

Figure 3–13: The two jigs constructed to (a) glue, and (b) wrap porous wire meshes around the solid cylinders.

The second step was to wrap the mesh (glued to the cylinder along this thin strip) tightly around the cylinder, ensuring a minimal gap between each layer. To this end, a second jig was designed in which the the cylinder was supported on each end using two bearings − see Figure 3–13(b). The wire mesh, now attached to the cylinder by the thin strip of glue, was held in tension with two pieces of wood placed across its width and affixed at either end. The cylinder was then turned about its axis, wrapping the mesh tightly around it, until the desired diameter was reached. The cylinder was then fixed in place using a special clamp (a piece of wood with a hole in the middle and a slot at its top; a screw across the slot allowed the clamp to be tightened around the cylinder, holding it in place).

Once the cylinder was wrapped with the wire mesh to the appropriate diameter and clamped, the outer-most layer of wire mesh was glued to the one below it, at about the same radial location at which the other end of the mesh was glued to the cylinder. Once again, the mesh was pre-scored prior to gluing; and the extra length of the wire mesh removed by hand, once the glue had dried, by bending it back-and-forth along the scored line, until it broke off cleanly. A total of nine cylinders with porous outer layers were made, corresponding to the three different wire meshes and porous layer thicknesses mentioned above. Photographs of three of the cylinders with porous outer layers are presented in Figure 3–14.

(a) Some cylinders with porous outer layer

(b) 1/16" thickness

(c) 1/8" thickness

(d) 1/4" thickness

Figure 3–14: Cylinders with porous outer layers, including view from the top for three different thicknesses of the porous layer.

Because of the different thickness of the three wire meshes, it was not possible to produce cylinders that were all exactly 1" in diameter. In addition, there were slight variations in diameter in the axial direction of a given cylinder. To account for these variations, an average of 5 measurements of the diameter along the porous part of the cylinder was used. All mean diameters were within the range 1 ± 0.05" (0.0254 ± 0.00127m), with standard deviations (σ) between 0.002" and 0.006", for a maximum relative uncertainty of 0.603%. The mean diameters and standard deviations for the smooth cylinder and the cylinders with porous outer layers are summarized in Table 3–7.

Pores Per Inch PPI	Porous Layer Thickness PLT (in)	Mean Diameter (in)	Standard Deviation (in)	Layers of Wire Mesh
Smooth	n/a	1.001	0.001	n/a
10	$1/16$	1.052	0.002	2
10	$1/8$	1.003	0.005	3
10	$1/4$	1.002	0.006	5
20	$1/16$	0.981	0.006	2
20	$1/8$	0.991	0.003	5
20	$1/4$	0.988	0.004	10
40	$1/16$	0.982	0.005	3
40	$1/8$	0.990	0.003	7
40	$1/4$	0.975	0.004	13

Table 3–7: Mean diameters and standard deviations of cylinders without and with porous outer layers.

3.7 Mounting of the Cylinder in the Wind Tunnel

To minimize end effects on the flow over the cylinder, rectangular end plates were installed near the top and bottom of the cylinder adjacent to the walls of the wind tunnel. Following the recommendations of Stansby (1974), the end plate dimensions were $7D_{cyl}$ wide in the cross-stream direction, and $8D_{cyl}$ long in the stream-wise direction, with the longitudinal axis of the cylinder located $3.5D_{cyl}$ from its upstream end and $4.5D_{cyl}$ from its downstream end. The corners of the end plates were rounded to minimize the formation of tip vortices.

The end plates were placed outside the boundary layers on the wind tunnel walls, 2" (0.0508m) from the bottom wall and 2.75" (0.0699m) from the top wall (it should be noted again that the top wall of the wind-tunnel test section diverges to ensure a constant mean velocity in the inner region of the flow). Following the design of Klausmann and Ruck (2017), 1.66" (0.0421m) diameter PVC pipes (schedule 80, $1\frac{1}{4}$" nominal) were installed between the end plates and the tunnel walls to prevent flow over the cylinder in these regions. The resulting length of the cylinder between the two end plates (i.e., the length of the cylinder exposed to air flow in the wind tunnel) was 11.75" (0.298m).

The cylinder was mounted on the wind tunnel balance (which was installed below the wind tunnel) in the following way. An aluminum block was fastened to the bottom of the cylinder with a 1/2" (0.0127m) fine-threaded screw. Then the aluminum block was fastened horizontally with two 10-32 screws to the bracket at the top of the wind tunnel balance. A photograph of a cylinder mounted in the tunnel in this manner is presented in Figure 3–15.

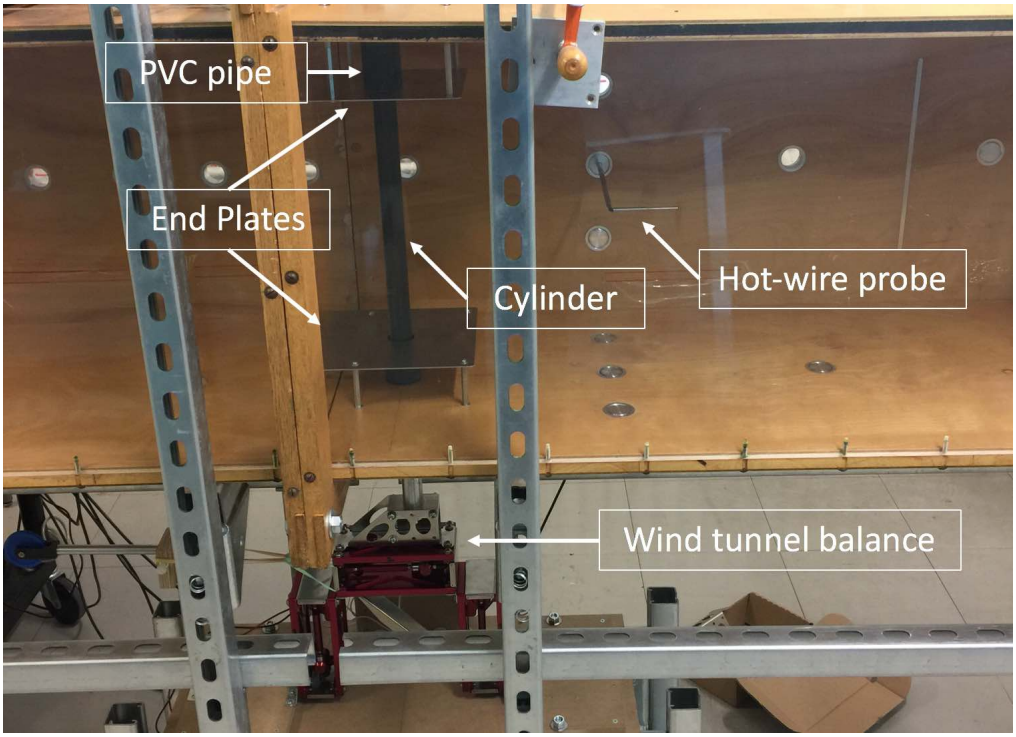

Figure 3–15: Mounting of a cylinder in the wind tunnel.

CHAPTER 4
Results and Discussion

The results of experiments quantifying the drag on cylinders, with and without porous outer layers, are discussed in this chapter. First, however, the flow in the test section of the wind tunnel is characterized. Next, measurements of the drag coefficient for a smooth cylinder at different Reynolds numbers are presented and compared with values from the literature. Subsequently, the drag coefficient for a smooth cylinder in flows of different free-stream turbulence intensities is presented. Finally, the drag on cylinders with porous outer layers, including the effects of the Reynolds number, free-stream turbulence intensity, porous layer thickness, and pores-per-inch (PPI) of the wire meshes (used for creating the porous layer), are summarized.

4.1 Wind Tunnel Flow Characterization

As was discussed in §3.1.2, the flow in the test section of the wind tunnel was first characterized by measuring three horizontal and three vertical mean (time-mean) velocity profiles, at three downstream locations, with no grid installed. The resulting mean velocities and turbulence intensities are presented in Figures 4–1 and 4–2, respectively.

The mean velocity profile exhibits a high degree of homogeneity at all three downstream locations in both the horizontal (y) and vertical (z) cross-stream directions. The thickness of the boundary layer along the wind-tunnel walls is roughly 0.025m, 0.050m, and 0.075m at $x = 0.92$m, 2.32m and 4.32m, respectively. Note that the boundary layer along the top wall is farther from the tunnel centreline ($y, z = 0$) due to the divergence of that wall, as previously noted.

The profiles of turbulence intensity further validate the homogeneity of the flow, as well as identifying the boundary layers at different downstream locations. The turbulence intensity in the core of the flow is $T_i = 0.4\%$.

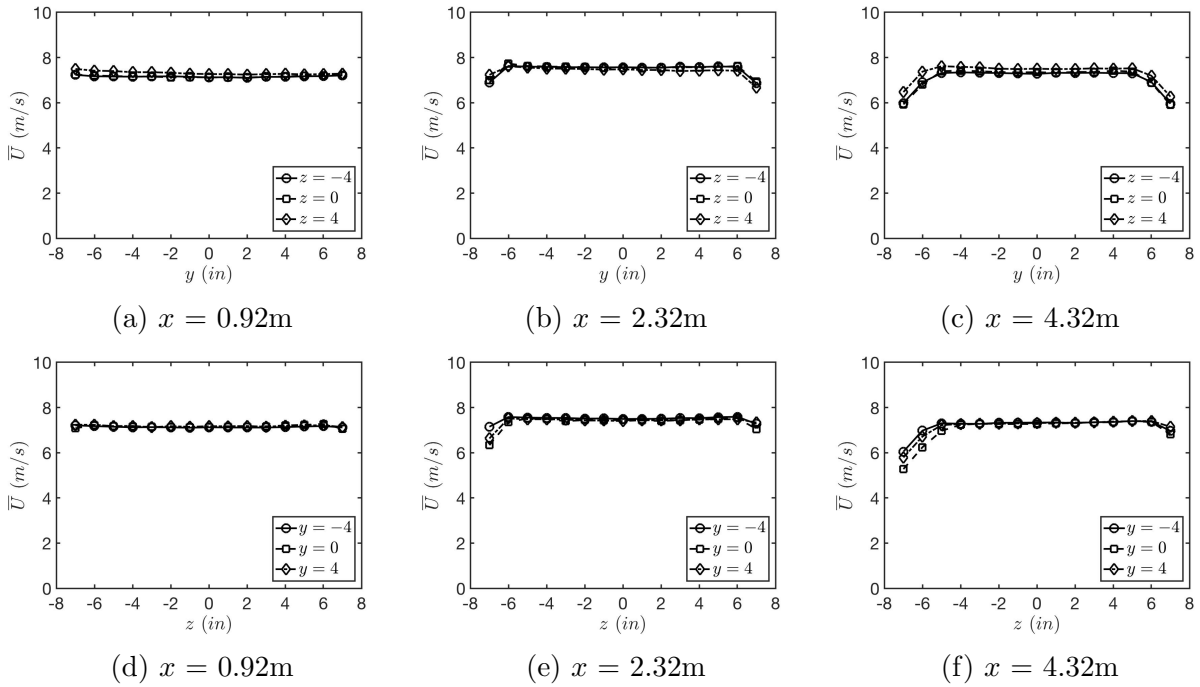

(a) $x = 0.92$m (b) $x = 2.32$m (c) $x = 4.32$m

(d) $x = 0.92$m (e) $x = 2.32$m (f) $x = 4.32$m

Figure 4–1: Horizontal (a, b, c) and vertical (d, e, f) mean velocity profiles at different downstream (x) locations in the wind tunnel test section, with no grid, at a nominal mean velocity of 7.5m/s.

The flow in the test section was then characterized after installing three different grids (1" passive grid, 2" passive grid, and active grid) by taking one horizontal ($z = 0$) and one vertical ($y = 0$) profile at two downstream locations. (Profiles were not taken at $x = 0.92$m since the flow would not have sufficiently developed to become homogeneous and isotropic at this downstream location, due to the larger mesh lengths of the 2" passive grid and active grid.) The resulting mean velocities and turbulence intensities are presented in Figures 4–3 and 4–4, respectively.

It can be observed that the flow is effectively homogeneous (away from the boundary layers) in both the horizontal and vertical directions, at both downstream locations, for all three grids. However, the degree of homogeneity of the flow with the active grid is somewhat less strong, due to the large integral length scales generated. (The larger the ratio of the wind tunnel width to the integral length scale, the more homogeneous will be the flow). At x = 2.32m, the centreline turbulence intensities generated by the 1" passive grid, the

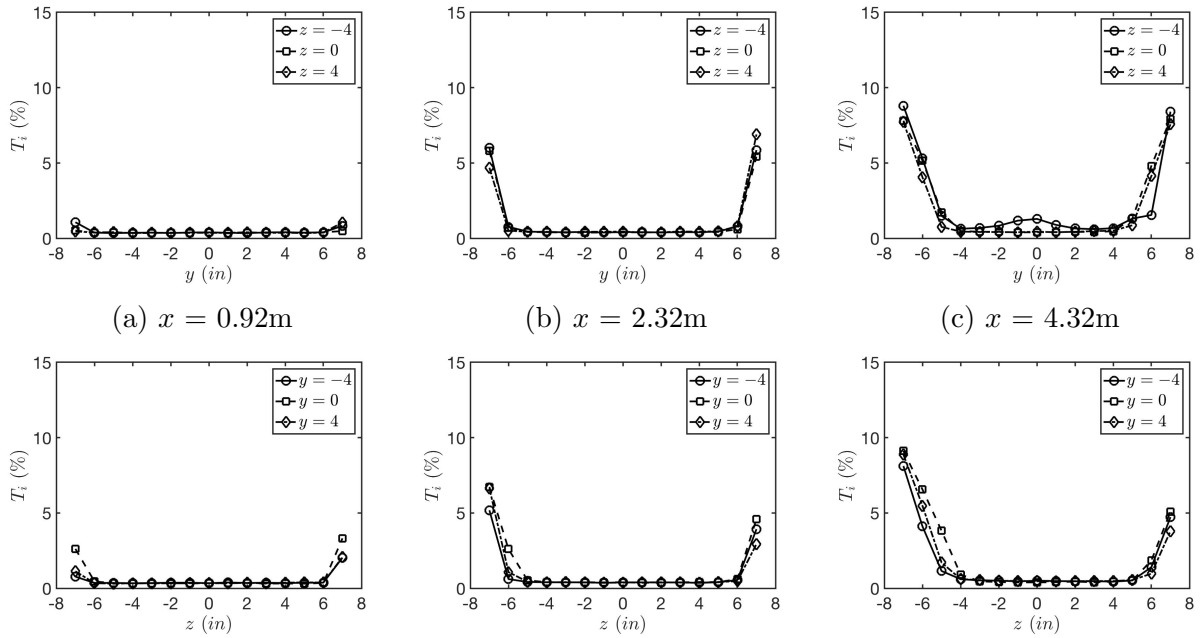

(a) $x = 0.92$m (b) $x = 2.32$m (c) $x = 4.32$m

(d) $x = 0.92$m (e) $x = 2.32$m (f) $x = 4.32$m

Figure 4–2: Horizontal (a, b, c) and vertical (d, e, f) profiles of turbulence intensity at different downstream (x) locations in the wind tunnel test section, with no grid, at a nominal mean velocity of 7.5m/s.

2" passive grid, and the active grid are 1.7%, 2.7% and 12.4%, respectively. Clearly, the active grid generates significantly higher turbulence intensities than the passive ones. More importantly, this is within range of the turbulence intensities observed in the atmosphere ($10\% \lesssim T_i \lesssim 35\%$).

To measure the decay of the turbulence in the downstream direction, the variance of the velocity fluctuations (i.e., a surrogate of the turbulent kinetic energy of the flow) was measured at the tunnel centreline ($y, z = 0$) at 10 different downstream locations, at a nominal mean velocity of 6m/s, for the i) 1" passive grid, ii) 2" passive grid, and iii) active grid. The results are presented in Figure 4–5, and include power-law curve fits to the data for each case. In all three cases, the decay of the velocity variance followed a power law ($u_{rms}^2/\overline{U}^2 = B(x/M)^n$), where the coefficient (n) was found to be approximately –1.3. This is in agreement with results from Sirivat and Warhaft (1983) for passive grids, and Mydlarski and Warhaft (1996) for the active grid.

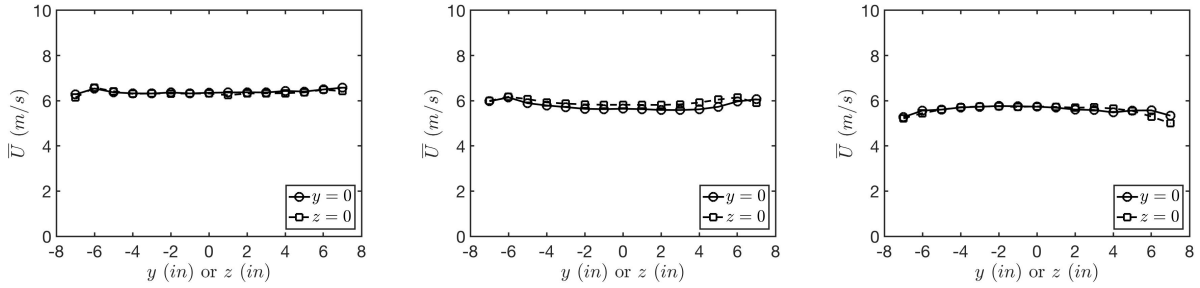

(a) 1" Passive Grid, $x = 2.32$m (b) 2" Passive Grid, $x = 2.32$m (c) Active Grid, $x = 2.32$m

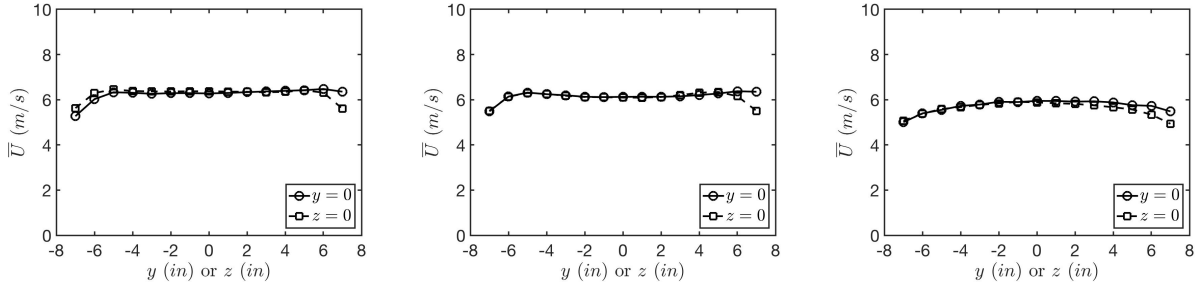

(d) 1" Passive Grid, $x = 4.32$m (e) 2" Passive Grid, $x = 4.32$m (f) Active Grid, $x = 4.32$m

Figure 4–3: Horizontal and vertical mean velocity profiles at $x = 2.32$m (a,b,c) and $x = 4.32$m (d,e,f) in the wind tunnel test section, for the different grids, at a nominal mean velocity of 6m/s.

The turbulence intensities, integral length scales, and other turbulence statistics were measured at $x = 2.32$m, just upstream of where the cylinder would be located in the wind tunnel ($x_{cyl} = 2.57$m). The results are summarized in Table 4–1. As expected, the turbulence generated with the active grid exhibits significantly higher values of the Taylor-microscale Reynolds number (R_λ), the turbulence intensity (T_i), and the integral length scale in the x-direction (ℓ_x).

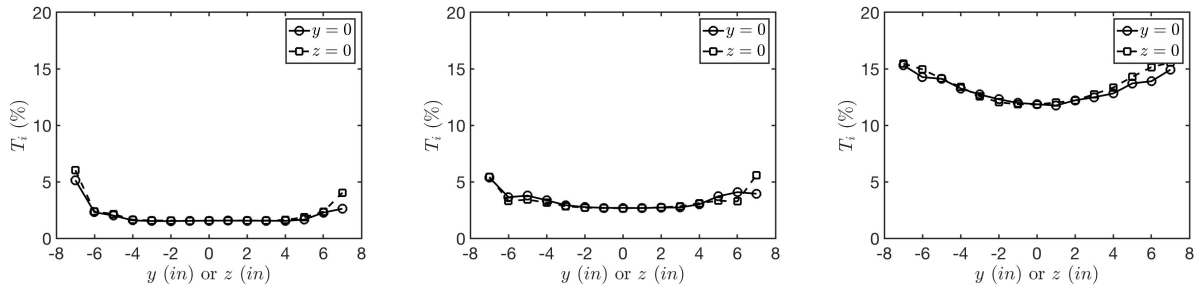

(a) Passive Grid 1", $x = 2.32$m (b) Passive Grid 2", $x = 2.32$m (c) Active Grid, $x = 2.32$m

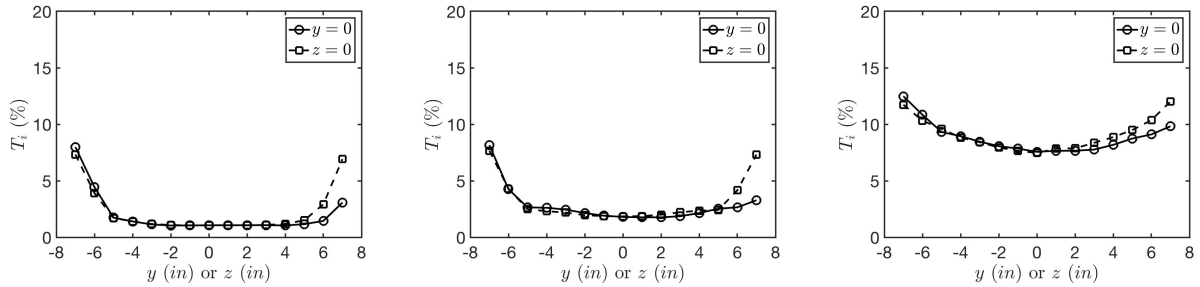

(d) Passive Grid 1", $x = 4.32$m (e) Passive Grid 2", $x = 4.32$m (f) Active Grid, $x = 4.32$m

Figure 4–4: Horizontal and vertical profiles of turbulent intensity at $x = 2.32$m (a,b,c) and $x = 4.32$m (d,e,f) in the wind tunnel test section, for the different grids, at a nominal mean velocity of 6m/s.

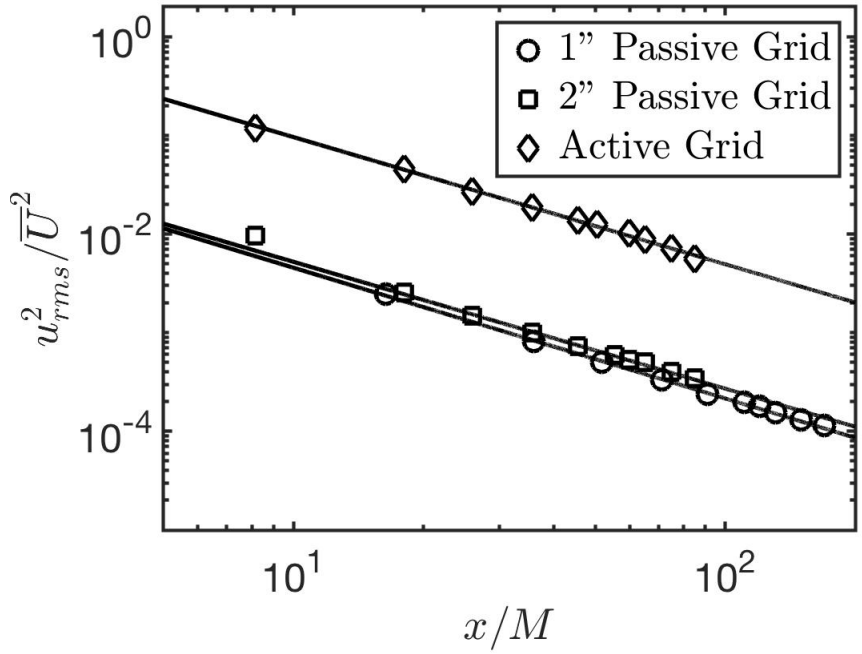

Figure 4–5: Downstream decay of the variance of the velocity at the tunnel centreline for different grids, including power-law curve fits, at a nominal mean velocity of 6m/s.

Parameter	No grid	1" Passive Grid	2" Passive Grid	Active Grid
Mesh size M (cm)	n/a	2.54	5.08	5.08
x/M	n/a	91	46	46
$\overline{U}$ (m/s)	9.97	9.96	9.95	10.06
u_{rms} (m/s)	0.04	0.17	0.27	1.25
T_i (%)	0.4	1.7	2.7	12.4
R_λ	n/a	59	94	430
ℓ_x (m)	0.002	0.022	0.037	0.125
ϵ (m^2/s^3)	0.02	0.21	0.61	13.0
η (mm)	0.66	0.37	0.29	0.15
B	n/a	0.0958	0.100	2.10
n	n/a	-1.32	-1.28	-1.29

Table 4–1: Turbulence statistics without and with grids upstream of the location of the cylinder, measured at $x = 2.32$m without the cylinder in place.

4.2 Drag on Smooth Cylinders: Benchmarking Experiments

To benchmark the experimental apparatus, the drag coefficient on a smooth cylinder was measured in the wind tunnel with no grid installed ($T_i = 0.4\%$), at nominal mean velocities of 4, 6, 8 and 10m/s ($7000 \lesssim Re_D \lesssim 17000$). This range of mean velocity was selected to obtain Reynolds numbers similar to those experienced by cylindrical firebrands. The results are presented in Figure 4–6, and compared to results from relevant prior investigations.

As was mentioned in §2.2, the drag coefficients measured on circular cylinders depend upon the aspect ratio, cylinder end conditions, blockage effects, and free-stream turbulence intensity. The present results are in general agreement ($\pm 5\%$) with those of Delany and Sorensen (1953), who had similar cylinder end conditions as the present work, though with a higher aspect ratio ($L/D = 28$, compared to 12 for this work). Since the drag coefficient increases with aspect ratio (see Figure 2–3), this may explain why their results are $3 - 5\%$ larger than the current results. The present results are also in agreement with those of Okamoto and Yagita (1973), whose cylinders had a similar aspect ratio, but different end conditions (one free end and one end plate, as opposed to the two end plates used in this

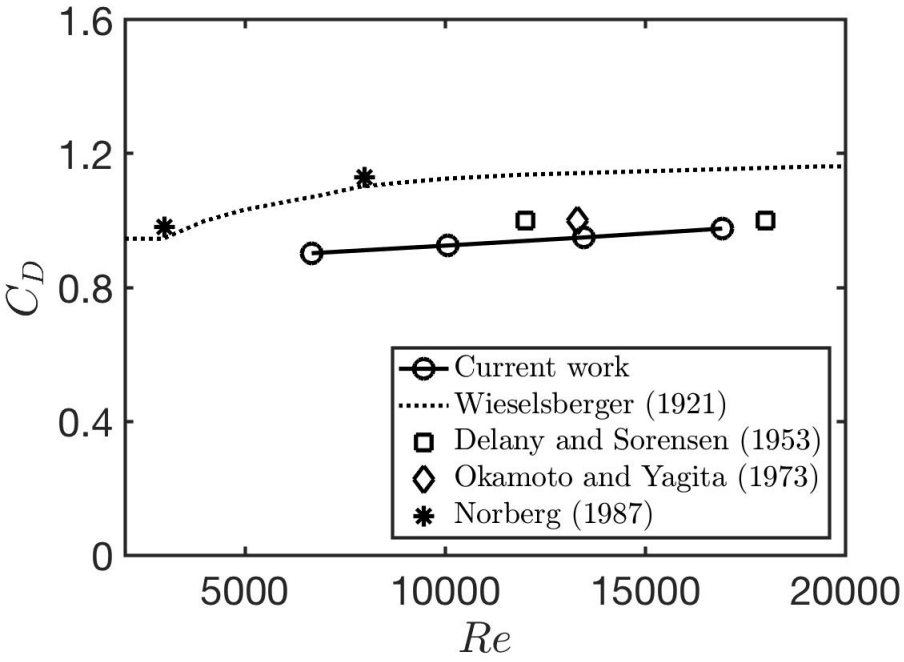

Figure 4–6: Drag coefficient as a function of Reynolds number for a smooth cylinder at $T_i = 0.4\%$, including results from other investigations.

work). The results of Wieselsberger (1921) and Norberg (1987) were significantly higher than the current results, likely due to the substantially higher aspect ratios (>280 and 80, respectively) in these experiments, as well as the lack of a correction for blockage effects, which cause the drag coefficient to decrease. Note, however, that the drag coefficient in the current experiments increased slightly with Reynolds number — a trend also observed by both Wieselsberger (1921) and Norberg (1987) in the range $3000 \lesssim Re_D \lesssim 20000$.

4.3 Drag on Smooth Cylinders: Effects of Free-Stream Turbulence

The drag coefficient for a smooth cylinder was further measured in flows with three different grids installed in the wind tunnel, for the same range of mean velocity, and compared with results at $T_i = 0.4\%$. The results are summarized in Figure 4–7. At relatively low turbulence intensities ($T_i = 0.4\%$, 1.7% and 2.7%), the drag coefficient increases with increasing turbulence intensity (i.e., $C_{D,0.4\%} \lesssim C_{D,1.7\%} \lesssim C_{D,2.7\%}$). However, at high turbulence intensity ($T_i = 12.4\%$), the drag coefficient is reduced, attaining similar values as those for $T_i = 0.4\%$. As will be demonstrated in the next section, the same trend was also observed

for the cylinders with porous outer layers, i.e., the drag coefficient increasing with turbulence intensity at relatively low turbulence intensities, then decreasing at high turbulence intensity. A possible explanation for this behaviour will be presented later.

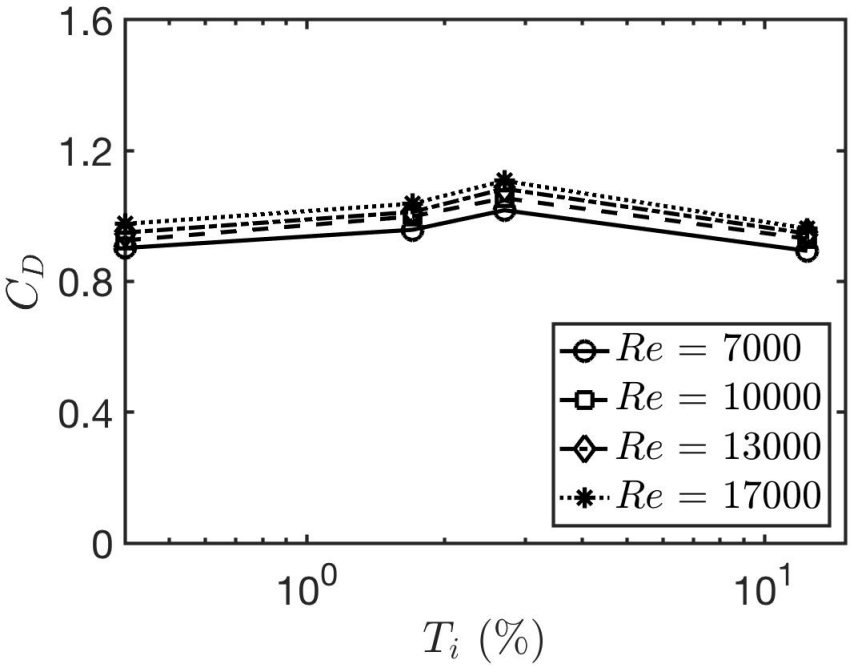

Figure 4–7: Effects of the turbulence intensity on the drag coefficient for a smooth cylinder.

4.3.1 Repeatability

To determine the repeatability of the results, experiments to measure the drag coefficient for a smooth cylinder at nominal mean velocities of 4, 6, 8 and 10m/s, were repeated for the following cases: i) no grid ($T_i = 0.4\%$), 5 runs; ii) 1" passive grid ($T_i = 1.7\%$), 4 runs; and iii) 2" passive grid ($T_i = 2.7\%$), 4 runs. The results are presented in Figure 4–8, and the mean values ($\overline{C_D}$) and standard deviations (σ_{C_D}) are summarized in Table 4–2. The results showed excellent repeatability in all cases, with a standard deviation of the drag coefficient of $0.01 - 0.03$, and a maximum relative uncertainty of 3.07%, where the relative uncertainty is taken as the standard deviation divided by the value of the drag coefficient. This is higher than the relative uncertainty of 2.06% calculated in Appendix C, likely because this value was computed by combining relative uncertainties of different measured parameters. A complete

analysis on the uncertainties of the measured and calculated variables, including the mean velocity and the force, is presented in Appendix C.

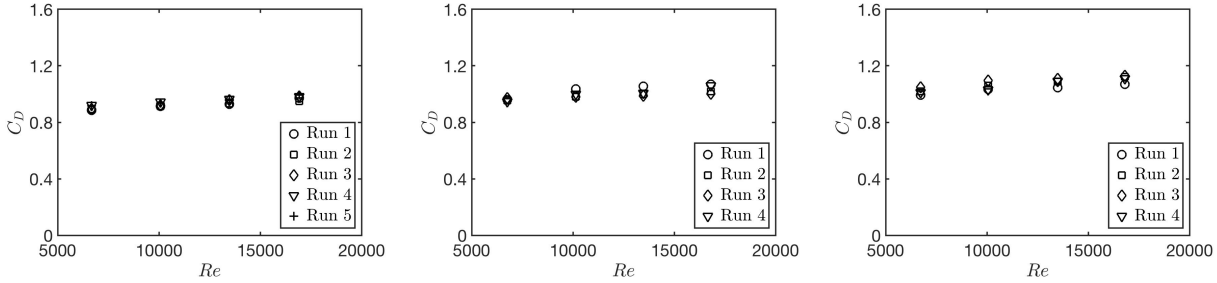

(a) $T_i = 0.4\%$ (b) $T_i = 1.7\%$ (c) $T_i = 2.7\%$

Figure 4–8: Repeatability results for a smooth cylinder with (a) $T_i = 0.4\%$, (b) $T_i = 1.7\%$, and (c) $T_i = 2.7\%$.

	No Grid		1" Passive Grid		2" Passive Grid	
$\overline{U}$ (m/s)	$\overline{C_D}$	σ_{C_D}	$\overline{C_D}$	σ_{C_D}	$\overline{C_D}$	σ_{C_D}
4	0.90	0.02	0.96	0.01	1.02	0.02
6	0.93	0.01	1.00	0.03	1.05	0.03
8	0.95	0.02	1.01	0.03	1.08	0.03
10	0.98	0.02	1.04	0.03	1.11	0.03

Table 4–2: Mean ($\overline{C_D}$) and standard deviations (σ_{C_D}) of repeated runs for a smooth cylinder for the cases of no grid ($T_i = 0.4\%$), a 1" passive grid ($T_i = 1.7\%$), and a 2" passive grid ($T_i = 2.7\%$).

4.4 Drag on Cylinders with Porous Outer Layers

Nine cylinders with porous outer layers were tested, corresponding to three different values of pores per inch (PPI) and three different thicknesses (porous layer thickness or PLT). These experiments were conducted at four different nominal mean velocities (4, 6, 8 and 10m/s) and four turbulence intensities (0.4%, 1.7%, 2.7% and 12.4%). Note that the Reynolds number differs slightly between each case for similar nominal velocities because i) there was some variability in the values of mean velocity, even though an effort was made to get them as close as possible to the nominal values of 4, 6, 8 and 10m/s; and ii) each cylinder with a porous outer layer has a slightly different mean diameter, as was previously noted.

In the following sections, the results are presented in four different ways to observe the effects of the i) Reynolds number, ii) free-stream turbulence intensity, iii) porous-layer thickness (PLT), and iv) pores per inch (PPI) on the drag coefficient.

4.4.1 Effects of Reynolds Number

The effects of the Reynolds number on the drag coefficients for the cylinders with porous outer layers are summarized in Figure 4–9. Firstly, it can be observed that for a turbulence intensity of 0.4%, the drag coefficient increases with Reynolds number, as in the case for a smooth cylinder. On the other hand, at a turbulence intensity of 12.4%, the drag coefficient is relatively independent of Reynolds number. At turbulence intensities of 1.7% and 2.7%, the relationship between C_D and Re_D appears to be affected by the pores per inch: at 10 PPI, the drag coefficient is relatively invariant to changes in Reynolds number; while at 20 PPI and 40 PPI, the drag coefficient increases with Reynolds number.

As was mentioned in the previous section, for a smooth cylinder, the results of Wieselsberger (1921) and Norberg (1987) exhibit a drag coefficient that increases with the Reynolds number in the range $3000 \lesssim Re_D \lesssim 20000$, then remains relatively flat in the range $20000 \lesssim Re_D \lesssim 10^5$. Also, as was mentioned in Section 2.2.2, experiments by Fage and Warsap (1929) (later validated by other researchers) show that as the free-stream turbulence intensity increases, the critical Reynolds number decreases, causing a shift of the C_D versus Re_D curve to the left. This shift towards lower Reynolds numbers may explain why the C_D versus Re_D slope tends towards zero with increasing turbulence intensity.

Although one cannot definitively conclude from the present measurements why the above-mentioned effect is observed for porous layers of 10 PPI, it appears as if the relatively higher surface roughness associated with PPI = 10 generates higher turbulence near the surface of the cylinder, and therefore produces similar effects on the boundary layer to those caused by the free-stream turbulence on a smooth cylinder.

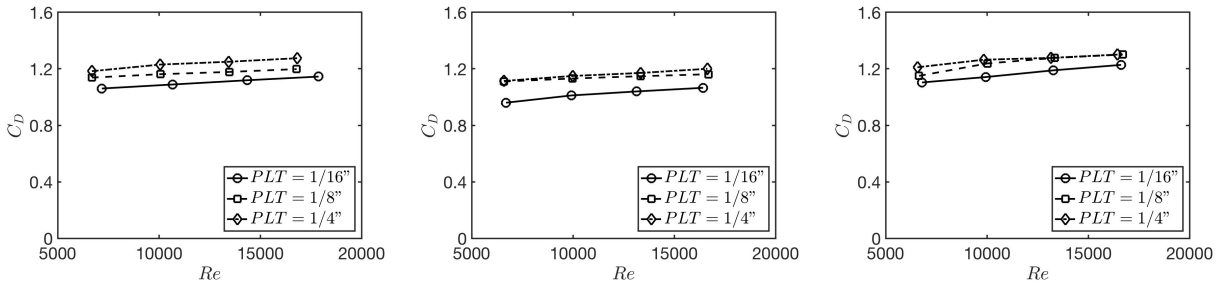

(a) $T_i = 0.4\%$, 10 PPI (b) $T_i = 0.4\%$, 20 PPI (c) $T_i = 0.4\%$, 40 PPI

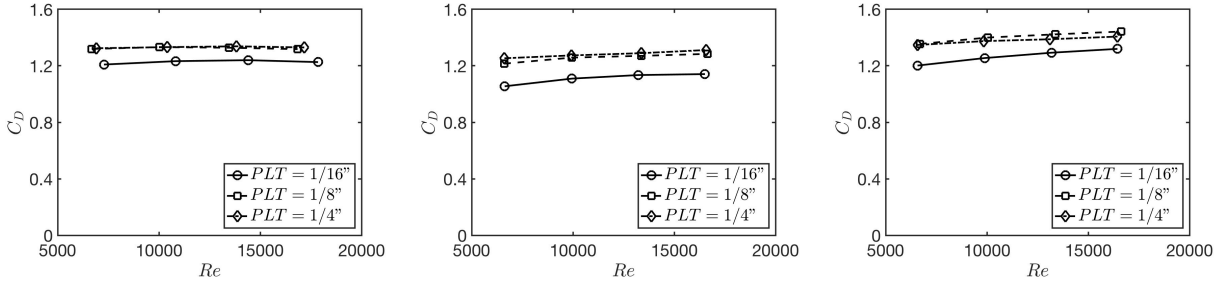

(d) $T_i = 1.7\%$, 10 PPI (e) $T_i = 1.7\%$, 20 PPI (f) $T_i = 1.7\%$, 40 PPI

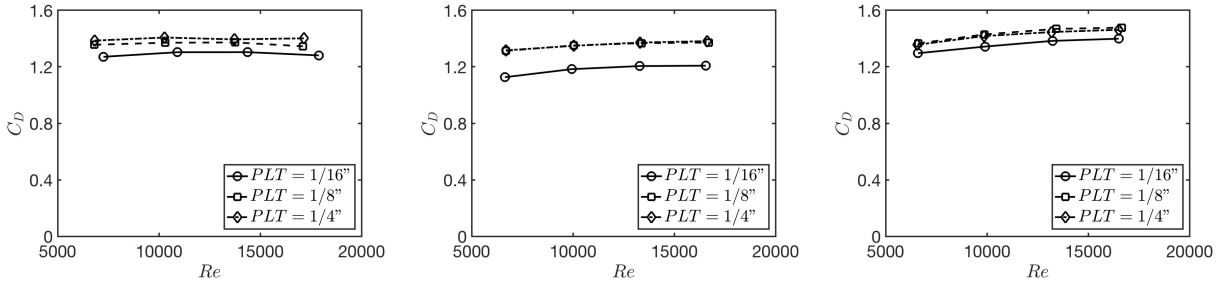

(g) $T_i = 2.7\%$, 10 PPI (h) $T_i = 2.7\%$, 20 PPI (i) $T_i = 2.7\%$, 40 PPI

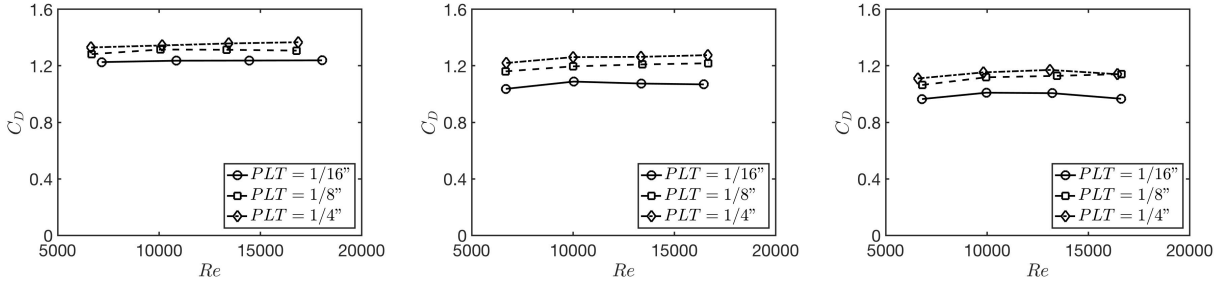

(j) $T_i = 12.4\%$, 10 PPI (k) $T_i = 12.4\%$, 20 PPI (l) $T_i = 12.4\%$, 40 PPI

Figure 4–9: Effects of the Reynolds number on the drag coefficient for cylinders with porous outer layers.

4.4.2 Effects of Free-Stream Turbulence

The effects of the free-stream turbulence intensity on the drag coefficients for cylinders with porous outer layers are summarized in Figure 4–10. As in the case of a smooth cylinder,

the drag coefficient increases with increasing turbulent intensity for relatively low turbulence intensities (0.4%, 1.7% and 2.7%), then exhibits a decrease at the highest turbulence intensity (12.4%). It is worth noting that this decrease seems to be affected by value of the PPI: for 10 PPI, $C_{D,0.4\%} \lesssim C_{D,12.4\%} \approx C_{D,1.7\%} \lesssim C_{D,2.7\%}$; for 20 PPI, $C_{D,0.4\%} \lesssim C_{D,12.4\%} \lesssim C_{D,1.7\%} \lesssim C_{D,2.7\%}$; and for 40 PPI, $C_{D,12.4\%} \lesssim C_{D,0.4\%} \lesssim C_{D,1.7\%} \lesssim C_{D,2.7\%}$. Recall from the discussions in the previous section that $C_{D,12.4\%} \approx C_{D,0.4\%} \lesssim C_{D,1.7\%} \lesssim C_{D,2.7\%}$ for a smooth cylinder.

To explain these observations, it is hypothesized that, at the relatively low turbulence intensities (0.4% to 2.7%), an increase in the turbulence intensity increases the friction drag on the cylinders without reducing the form drag, causing a net increase in the drag coefficient. A similar result was obtained by Norberg (1987), who observed an increase in the drag coefficient between turbulence intensities of 0.1% and 1.4%; however, as was noted in §2.2, there is wide scatter in published results on effect of the turbulence intensity on the drag coefficient in the subcritical range. For high turbulence intensities, the friction drag would continue to increase as in the other cases; however, this effect on the friction drag is overpowered by a decrease in form drag, perhaps due to the displacement of the separation point of the boundary layer along the cylinder away from the front stagnation point, potentially associated with a transition to turbulent flow in the boundary layer resulting from the intense free-stream turbulence, and a narrowing of the wake. This phenomenon appears to be more pronounced as the PPI value increases.

4.4.3 Effects of Porous-Layer Thickness

The effects of the porous-layer thickness on the drag coefficient are summarized in Figure 4–11. Note that in this figure, a porous-layer thickness of zero corresponds to the smooth cylinder. From this figure, two principle observations can be made: first, the drag coefficient appears to be a monotonically increasing function of the thickness of the porous layer; and second, the drag coefficient appears to asymptote to a constant value at porous layer thicknesses beyond $1/8$", such that $C_{D,1/8"} \approx C_{D,1/4"}$.

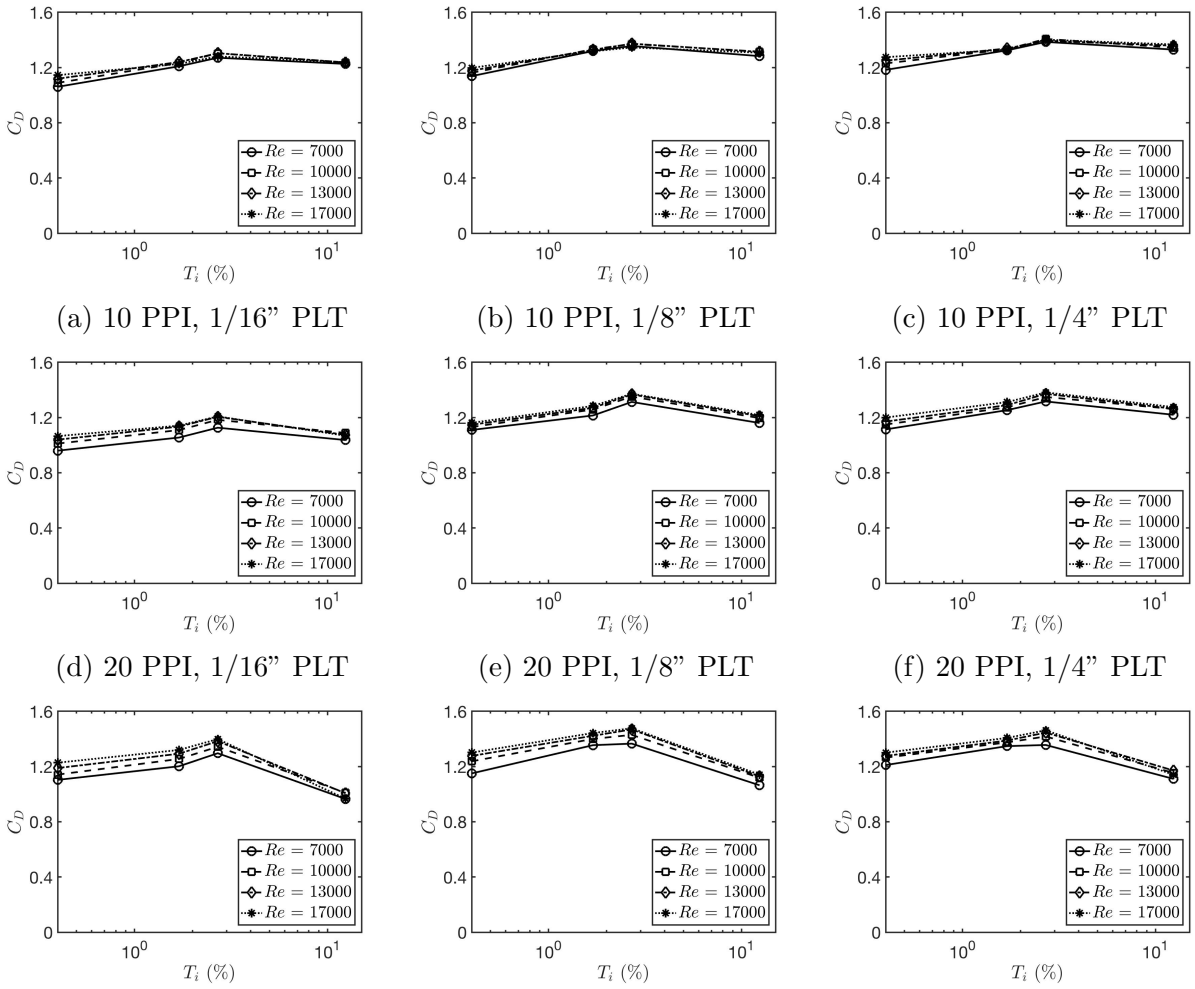

(a) 10 PPI, 1/16" PLT (b) 10 PPI, 1/8" PLT (c) 10 PPI, 1/4" PLT

(d) 20 PPI, 1/16" PLT (e) 20 PPI, 1/8" PLT (f) 20 PPI, 1/4" PLT

(g) 40 PPI, 1/16" PLT (h) 40 PPI, 1/8" PLT (i) 40 PPI, 1/4" PLT

Figure 4–10: Effects of the turbulence intensity on the drag coefficient for cylinders with porous outer layers.

As was mentioned in §2.2, Klausmann and Ruck (2017) remarked that experiments on cylinders with porous outer layers exhibited an increase in the drag coefficient compared to smooth cylinders, though they did not publish any results to this effect. The first observation outlined above ($C_{D,Porous} > C_{D,Smooth}$) is in agreement with these findings. However, these results contradict the results of numerical simulations by Bruneau and Mortazavi (2006) and Bhattacharyya and Singh (2011), which showed a decrease in the drag coefficient from that for a smooth cylinder to one with a porous outer layer. A possible explanation for this discrepancy may lie with the uncertainties in the models used to approximate the flow

(assumed to be laminar) in the porous layer. For example, Bhattacharyya and Singh (2011) discretize the volume-averaged Darcy-Forchheimer equation to describe the laminar flow in the porous layer, without explicitly resolving the full details of the flow in the interstices of the porous layer, which would be prohibitively expensive, and effectively impossible due to the difficulty in specifying the exact topology of the porous media.

The observation that the drag coefficient increases with increasing PLT and asymototes to a fixed value may be explained as follows: as the thickness of the porous layer is increased, more fluid is able to flow within the porous outer layer, causing an increased drag, and therefore higher C_D. However, past a certain thickness, the air flow does not penetrate the full porous layer, all the way to the solid inner cylinder; the effect of increasing the PLT further becomes essentially insignificant. In these experiments, this critical thickness of the porous layer (PLT_{crit}) appears to occur somewhere in the range $1/16" \leq PLT_{crit} \leq 1/8"$.

4.4.4 Effects of Pores per Inch (PPI)

The effects of the PPI on the drag coefficient are summarized in Figure 4–12. Note that in this figure, zero PPI corresponds to the smooth cylinder. For almost all cases at relatively low turbulent intensities ($T_i = 0.4\%$, 1.7% and 2.7%), the drag coefficient decreases from porous layers with 10 PPI to those with 20 PPI, and then increases for porous layers with 40 PPI, such that $C_{D,20PPI} \lesssim C_{D,10PPI} \lesssim C_{D,40PPI}$. At the highest turbulent intensity ($T_i = 12.4\%$), the drag coefficient increases with decreasing PPI, such that $C_{D,40PPI} \lesssim C_{D,20PPI} \lesssim C_{D,10PPI}$.

To advance a physical explanation of these effects, further studies, with additional values of T_i and PPI, are required. In this context, flow visualization, or near-cylinder velocity measurements (by particle image velocimetry, for example), could also be very useful.

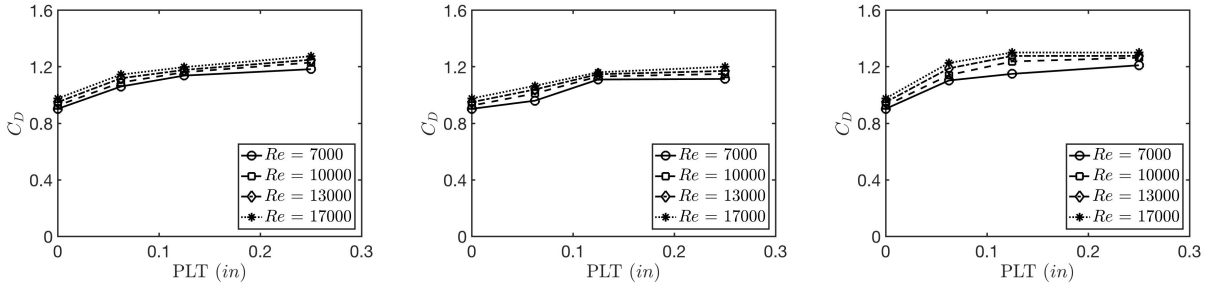

(a) $T_i = 0.4\%$, 10 PPI (b) $T_i = 0.4\%$, 20 PPI (c) $T_i = 0.4\%$, 40 PPI

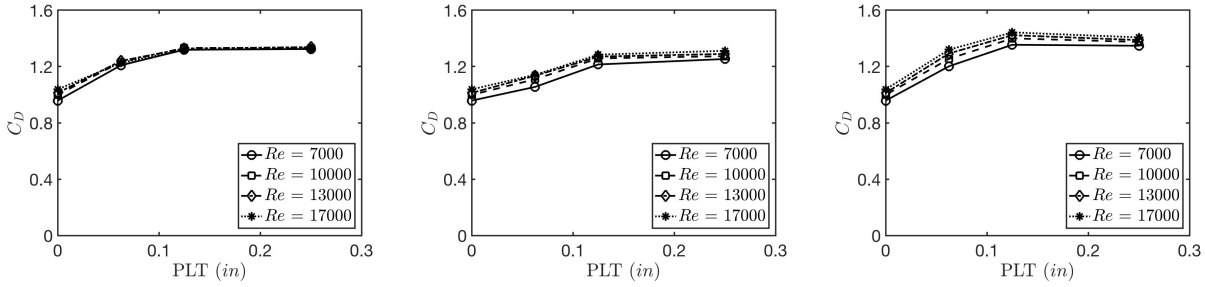

(d) $T_i = 1.7\%$, 10 PPI (e) $T_i = 1.7\%$, 20 PPI (f) $T_i = 1.7\%$, 40 PPI

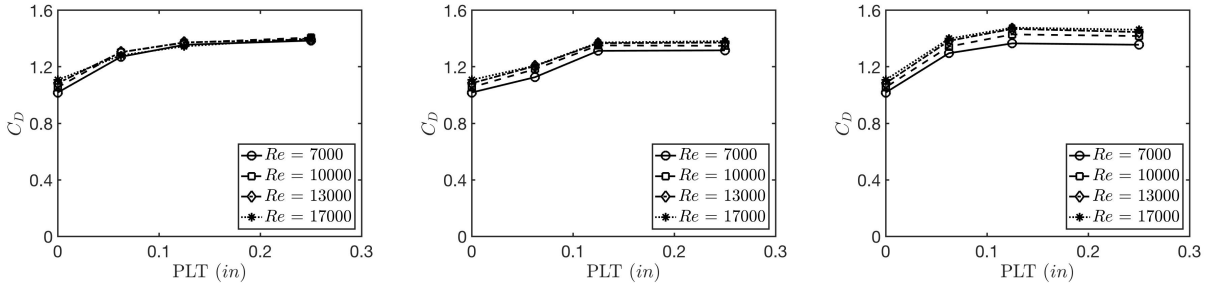

(g) $T_i = 2.7\%$, 10 PPI (h) $T_i = 2.7\%$, 20 PPI (i) $T_i = 2.7\%$, 40 PPI

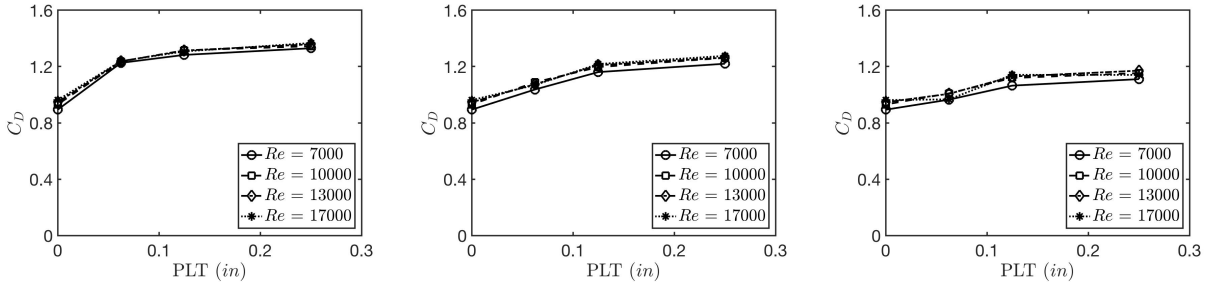

(j) $T_i = 12.4\%$, 10 PPI (k) $T_i = 12.4\%$, 20 PPI (l) $T_i = 12.4\%$, 40 PPI

Figure 4–11: Effects of the porous layer thickness on the drag coefficient for cylinders with porous outer layers. A porous layer thickness of zero corresponds to the smooth cylinder.

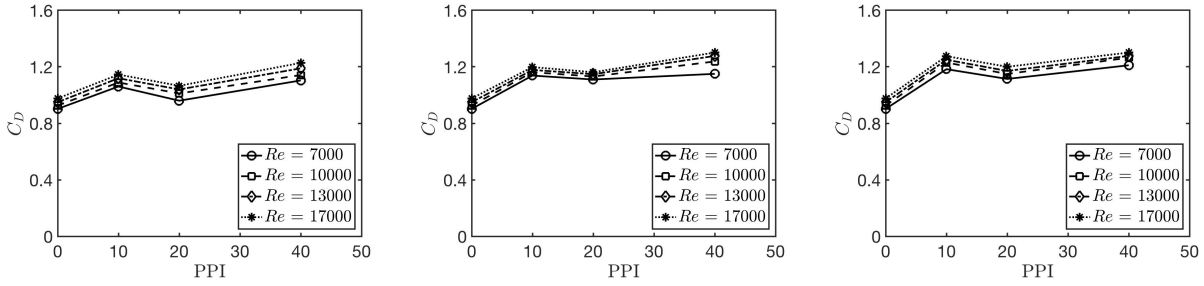

(a) $T_i = 0.4\%$, 1/16" PLT (b) $T_i = 0.4\%$, 1/8" PLT (c) $T_i = 0.4\%$, 1/4" PLT

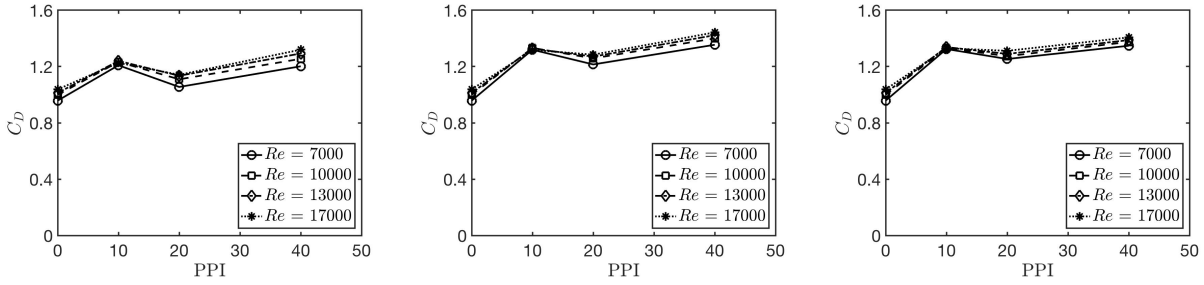

(d) $T_i = 1.7\%$, 1/16" PLT (e) $T_i = 1.7\%$, 1/8" PLT (f) $T_i = 1.7\%$, 1/4" PLT

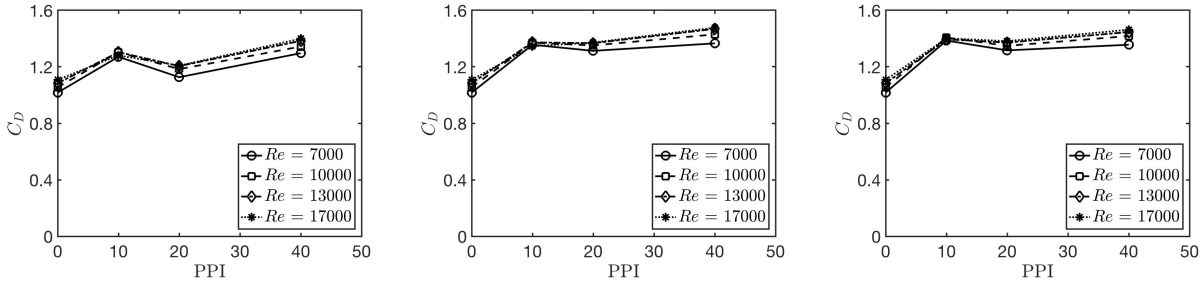

(g) $T_i = 2.7\%$, 1/16" PLT (h) $T_i = 2.7\%$, 1/8" PLT (i) $T_i = 2.7\%$, 1/4" PLT

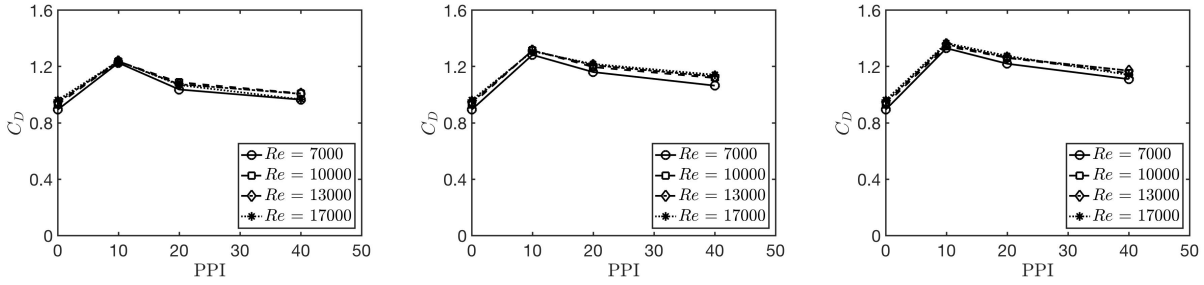

(j) $T_i = 12.4\%$, 1/16" PLT (k) $T_i = 12.4\%$, 1/8" PLT (l) $T_i = 12.4\%$, 1/4" PLT

Figure 4–12: Effects of the pores per inch (PPI) on the drag coefficient for cylinders with porous outer layers. Zero PPI corresponds to the smooth cylinder.

CHAPTER 5
Conclusion

This final chapter contains i) a summary of the previous chapters of this thesis; ii) an overview of the main contributions of this work; and iii) recommendations for extensions of this work.

5.1 Summary

In Chapter 1, the background and motivation, objectives, methodology, and organization of the thesis were presented. Chapter 2 presented a review of publications that are relevant to the present work, including prior studies of the trajectories of windborne firebrands and related topics.

Central to the second chapter was a review of past investigations of the drag coefficient for circular cylinders in cross-flow. The effects of the Reynolds number, cylinder aspect ratio, cylinder end conditions, and tunnel wall-interference were discussed. It was argued that the scatter in the published results of this drag coefficient is presumably due to variations in these parameters from one study to the next. Past investigations of the effects of the free-stream turbulence on the drag coefficient for circular cylinders were then reviewed, including the effects of turbulence intensity and integral length scales. It was concluded that there is little consensus thus far as to the effects of these parameters on the drag coefficient in the subcritical range (which is the range of Reynolds numbers considered in the present work). A short review of studies on the drag on cylinders with porous outer layers followed. The few investigations on this topic, however, were mostly numerical in nature.

The second chapter concluded with a section in which a brief review of the literature on the subject of turbulence was presented. In this section, a short overview of atmospheric turbulence, as well as its properties, was presented. A summary of past research on active

grids followed, where different modes of operation of active grids were discussed. Finally, a review of the principles underlying hot-wire anemometry was presented.

The experimental apparatus and techniques were discussed in Chapter 3. First, a description of the wind tunnel and its components was presented. Then, the properties of the different grids used (2 passive and 1 active) were summarized, including the design and construction of a controller to operate the active grid in the double-random mode. The operation and calibration of a hot-wire anemometer to measure the fluid velocity was also presented, including a modified King's law that minimizes the effects of small changes in the hot-wire ambient (cold) resistance. Following this, the operation and calibration of the wind tunnel balance, that was used to measure the drag on the cylinders, was outlined in detail.

Steel wire meshes wrapped around solid cylinders allowed the construction of cylinders with porous outer layers, with the desired depth and porosity. The procedure for precisely and reliably wrapping the wire meshes around the solid cylinders was explained, including the design and construction of specialized jigs to assist in this process. Three different wire meshes were used, wrapped to three different thicknesses, for a total of nine cylinders with porous outer layers. Finally, the mounting of the cylinders in the tunnel, including the design and installation of end plates to minimize tunnel-wall effects, was presented.

The results were presented and discussed in Chapter 4, starting with those used for the characterization of the flow in the wind tunnel. Horizontal and vertical profiles of the velocity and turbulence intensity were measured at different downstream locations, without and with the grids (passive and active). It was shown that the flow was effectively homogeneous across the test section for all cases. The variance of the velocity fluctuations was also measured at the tunnel centreline at different downstream locations, and was shown to follow a power-law decay, in agreement with results from the literature.

To benchmark the wind tunnel balance, the drag on a smooth cylinder in the wind tunnel with no grid ($T_i = 0.4\%$) was measured for Reynolds number in the range 7000 to 17000, and the drag coefficients calculated from the related measurements were in agreement with

values from the literature. The drag on the smooth cylinder was then measured at different levels of free-stream turbulence intensity, generated by i) a 1" passive grid ($T_i = 1.7\%$), ii) a 2" passive grid ($T_i = 2.7\%$), and iii) an active grid ($T_i = 12.4\%$). It was shown that at low turbulence intensities ($T_i = 0.4\% - 2.7\%$), the drag coefficient increases with increasing turbulence intensity, while at the high turbulence intensity ($T_i = 12.4\%$), the drag coefficient decreases. This same trend was observed for all 9 cylinders with porous outer layers, with the notable result that the decrease in the drag coefficient at high turbulence intensity appeared to be affected by the pores per inch (PPI) of the wire mesh (the higher the PPI, the lower the drag coefficient). This may be due to a displacement of the separation point of the boundary layer along the cylinder away from the front stagnation point, causing a narrowing of the wake and a decrease in the form drag, and therefore C_D.

The effects of the Reynolds number on the drag coefficient for cylinders with porous outer layers were also shown to depend on both the free-stream turbulence intensity and the PPI of the wire meshes. At low turbulence intensities and high PPI, the drag coefficient was shown to increase with Reynolds number, as in the case of a smooth cylinder; at high turbulence intensities and low PPI, the drag coefficient was relatively invariant to changes in Reynolds number.

The effects of the porous layer thickness on the drag coefficient were presented next. It was shown that the drag coefficient first increases with the thickness of the porous outer layer, then asymptotes to an almost constant value at a porous layer thickness of 1/8".

Finally, the effects of the pores per inch (PPI) of the wire meshes on the drag coefficient were discussed. The related results demonstrated that the drag coefficient decreased when the PPI was increased from 10 to 20, and then increased at a PPI of 40, at low turbulence intensities ($T_i = 0.4\% - 2.7\%$). At the highest turbulence intensity ($T_i = 12.4\%$), the drag coefficient decreased with increasing PPI.

5.2 Overview of the Main Contributions

The main contributions of this work are summarized below:

1. Setting up of a wind tunnel with passive and active grids, acquisition and installation of a blower and muffler, and design and construction of a support structure for the tunnel.
2. Design and construction of a controller to operate the active grid in double-random mode (the preferred mode of operation of active grids for the study of homogeneous, isotropic turbulence).
3. Characterization of the flow in the wind tunnel for the following cases: i) no grid, ii) 1" passive grid, iii) 2" passive grid, and iv) active grid.
4. Design and construction of special cylinders with porous outer layers of different porosities and thicknesses of the porous layer.
5. Quantification and discussion of the effects of Reynolds number, free-stream turbulence, porous-layer thickness, and pores per inch of the wire meshes (used to construct the porous layer) on the drag coefficient for the cylinders with and without the porous outer layer, for Reynolds number in the range 7000 to 17000. The key findings were elaborated in Chapter 4 and summarized in §5.1.

5.3 Recommendations for Extensions of this Work

Some recommendations for extending this work are summarized below:

1. Visualization and/or measurement of the flow near the surface of the cylinder would serve to quantify the effects of free-stream turbulence, porous layer thickness, and pores per inch of the wire meshes (used for constructing the porous outer layer on the cylinders), on the location of the separation of the boundary layer on the cylinder. Surface oil flow visualisation (SOFV) has been used in the past to determine the boundary-layer separation point, however this technique may not be feasible on the cylinders with porous outer layers. The use of particle image velocimetry (PIV) may be a more viable option, and could be implemented without much modification of the experimental setup, since one of the walls of the wind tunnel used in this work is transparent.

2. Velocity profiles measured upstream and downstream of the cylinders would provide insight into the effects of free-stream turbulence and the thickness and porosity of the porous outer layer on the flow in the wake behind the cylinders. These measurements could be readily made by way of hot-wire anemometry, with no modifications to the current setup.
3. The drag coefficient was shown to exhibit a non-monotonic dependence on the pores per inch (PPI) of the wire meshes that were used to construct the porous outer layer on the cylinders. Future work could be undertaken to determine the PPI at which the drag coefficient is minimized, by using the same procedure, as that described in Chapter 4, for making cylinders with steel wire meshes with 15, 25, 30 and 35 pores per inch.
4. The drag coefficient was shown to asymptote at a porous-layer thickness between $1/16$" and $1/8$". Future work could be undertaken to determine the porous-layer thickness at which the drag coefficient asymptotes, by wrapping steel mesh around inner cylinders machined to the appropriate diameters. Moreover, the dependence of this critical thickness on the number of pores per inch, Reynolds number, and turbulence intensity could also be investigated.
5. The effects of the cylinder yaw angle on the drag coefficient could be investigated by modifying the end plates in the wind tunnel and also the jig used to mount the cylinder on the wind tunnel balance. With these modifications in place, the lift coefficient, and its dependence on the Reynolds number, turbulence intensity, porous-layer thickness, pores per inch of the wire meshes, and yaw angle could also be investigated.
6. Investigations of additional values of the free-stream turbulence intensity, porous-layer thickness, and PPI of the wire meshes would allow the formulation of suitable correlations that could be used to predict the influence of these parameters on the drag and lift coefficients. Such correlations could be used to improve cost-effective mathematical models for the predictions of the trajectories of cylindrical firebrands.

7. Disks of circular and elliptic shape could be used to model firebrands made of leaves and pieces of bark.
8. Additional research could be undertaken in the wakes of heated porous cylinders, as well as in other turbulent flows, e.g.: Beaulac and Mydlarski (2004a,b), Lepore and Mydlarski (2009, 2012), and Berajeklian and Mydlarski (2011).
9. Experiments conducted with burning wooden cylinders and disks could be used for quantifying the effects of the surface temperature and volume-evolution of actual firebrands.

The overall goal of the work reported in this thesis was to contribute to ongoing worldwide efforts to improve the understanding and predictions of the spread of forest fires by the spotting mechanism. The focus in this work was on wind-tunnel experiments for quantifying the influences of free-stream turbulence intensity and char-layer characteristics (porosity and depth) on the drag on wind-borne firebrands. Attention was limited to non-burning cylindrical objects, without and with porous outer layers, which were constructed by wrapping wire meshes around solid cylinders. The results (presented and discussed in Chapter 4; and summarized in the earlier parts of this chapter) showed that the drag on these cylinders was significantly affected by the free-stream turbulence intensity, pores per inch of the wire meshes, and the depth of the wire-mesh layers. However, to obtain results which would lead to improved predictions of the trajectories of burning firebrands in the spotting mechanism, quite a few extensions of this work are necessary. Recommendations for such extensions were provided in this section. In conclusion, the author hopes that the work presented in this thesis will motivate other researchers to undertake these extensions. The long-term benefits of such extensions would be considerable, as they would allow the formulation of more effective strategies for the management (prevention, containment, and extinguishing) of forest fires.

Appendix A: Arduino Codes for the Active-Grid Controller

The codes for the master Arduino and one of the slave Arduinos used in the active-grid controller are presented in this appendix.

A.1 Master Arduino

```
// Program for Arduino Uno (Master) to send instructions
// to slave Arduinos to change operating parameters

#include <Wire.h>
int vars[4], j;
byte temp;

// *** MAIN FUNCTION ***
void setup() {
  Wire.begin(); // Start I2C Bus as Master
  Serial.begin(9600);
  vars[0] = 50; // min length
  vars[1] = 200; // max length
  vars[2] = 200; // min speed
  vars[3] = 500; // max speed
  j = 1;
  }

// *** MAIN LOOP ***
void loop() {
  int i;
```

```
  while (j<=10){  //send transmission j times
    Wire.beginTransmission(8);
    for (i = 0; i < 4; i++) {
      temp = vars[i];
      Wire.write(temp);
      temp = vars[i] >> 8;
      Wire.write(temp);
      }
    Wire.endTransmission();
    delay(500);
    j++;
    Serial.println("sent");
    }
  delay(1000);
  }
```

A.2 Slave Arduino

```
// Program for Arduino Nano controlling a single stepper motor,
// while receiving instructions from a Master Arduino
// Motor 1 (A1,A0)

#include <Wire.h>
int motorNum = 1;
int stepPin = A1;
int dirPin = A0;
const int stepsPerRev = 200; //Steps per rev for each motor
int minLength = 50;    // steps (200 steps per turn)
int maxLength = 300;   // steps
```

```
int minSpeed = 200;    // steps/second
int maxSpeed = 500;    // steps/second
int instSpeed, instLength, counter;
long delayUs;
int dir;
int rcd = 0;

// Define class stepper motors with functions Stepper,
// getSteps,goHIGH, goLOW
class stepper {
  private:
    int _stpPin;
    int _dirPin;
    long _steps = 0;

  public:
    stepper (int stpPin, int dirPin);
    void setDirection(int dir);
    void pulseVarHigh(long microDelay);
    void pulseVarLow(long microDelay);
};

// Stepper function for Stepper class,
// defines step and direction pins
stepper::stepper (int stpPin, int dirPin) {
  _stpPin = stpPin;
  _dirPin = dirPin;
```

```
  pinMode (_stpPin, OUTPUT);
  pinMode (_dirPin, OUTPUT);
}

// setDirection function for Stepper class, set direction
void stepper::setDirection(int dir) {
  digitalWrite(_dirPin, dir > 0); //Sets direction
}

// pulseVar function for Stepper class,
// allows variable length pulses for variable speeds
void stepper::pulseVarHigh(long microDelay) {
  digitalWrite(_stpPin, HIGH);
  delayMicroseconds(microDelay); // used to control the
                                 // pause between pulses
}

// pulseVar function for Stepper class,
// allows variable length pulses for variable speeds
void stepper::pulseVarLow(long microDelay) {
  digitalWrite(_stpPin, LOW);
  delayMicroseconds(microDelay); // used to control the
                                 // pause between pulses
}

// Define stepper motor output pins
stepper motor = stepper(stepPin,dirPin);
```

```
// *** Start of non-main functions***
// move each motor for the total pulse
// sequence with random velocities
void varSpeedStep()
{
    motor.pulseVarHigh(delayUs);
    motor.pulseVarLow(delayUs);
}

// Change parameters when instructions
// recieved from Mater Arduino
void receiveInt() {
  int vars[4], i;
  byte temp1, temp2;
  for (i = 0; i < 4; i++)
  {
    temp1 = Wire.read();
    temp2 = Wire.read();
    vars[i] = (unsigned int)temp2*256 + temp1;
  }
  minLength = vars[0];
  maxLength = vars[1];
  minSpeed = vars[2];
  maxSpeed = vars[3];
}
```

```
// *** MAIN FUNCTION ***
void setup() {
  Wire.begin(8); // join i2c bus with address #8
  Wire.onReceive(receiveInt);
  Serial.begin(9600);
  Serial.println("startup");

  //initialize direction, speed and length
  randomSeed(motorNum*100);
  dir = random(0,2);
  motor.setDirection(dir);
  instLength = random(minLength,maxLength+1);
  instSpeed = random(minSpeed,maxSpeed+1);
  delayUs = 1000000/(float)instSpeed/2;
  counter = 1;
}

// *** MAIN LOOP ***
void loop() {
  if (counter > instLength) {
    dir = not(dir); // change direction
    motor.setDirection(dir);
    instLength = random(minLength,maxLength+1); // choose new length
    instSpeed = random(minSpeed,maxSpeed+1);    // choose new speed
    delayUs = 1000000/(float)instSpeed/2;
    counter = 1; // restart counter
  }
```

```
    else
      counter++;

    varSpeedStep();
}
```

Appendix B: Active Grid Operating Procedure

In this appendix, the active grid operating procedure is presented, including how to operate the active grid, how to modify the operating parameters, as well as troubleshooting.

B.1 Operating the Active Grid

The active grid controller is designed in such a way that it operates in double random mode as soon as it is powered up. Because of this, both DC power supplies in the controller are connected to a power bar; the switch of the power bar can be used to turn the controller on and off.

B.2 Modifying the Operating Parameters

The default operating parameters, presented in §3.1.3, are hard-coded into the master Arduino. To change them, the code in the master Arduino must be modified (the default code for the master Arduino is presented in Appendix A).

To modify the master Arduino code or upload a new code, the following steps must be taken:

1. Download and install the open source Arduino IDE from *www.arduino.cc*.
2. Connect the active grid controller to the power source. The active grid must be operating to change its operating parameters.
3. Connect the master Arduino to the computer using the USB cable.
4. In the Arduino IDE, select the port that the Arduino is connected to by selecting Tools > Port.
5. Select the Arduino Uno board by selecting Tools > Boards.
6. To change the minimum and maximum turning angle, change the *minLength* and *maxLength* variables, respectively. Note that these are measured in steps, where 200 steps is equivalent to one full revolution (360°).

7. To change the minimum and maximum angular velocity, change the *minSpeed* and *maxSpeed* variables, respectively. Note that these are measured in steps per second, where 200 steps is equivalent to one full revolution (360°).
8. Click the upload button to upload the new code to the Arduino. The new operating parameters will be transmitted to the slave Arduinos within a few seconds.

B.3 Parameters of the Slave Arduinos

As mentioned in §3.1.3, each slave Arduino controls one stepper motor, which turns one of the fourteen bars on the active grid. The controller is designed with four protoboards in a stack, which provide the connections between the master Arduino, slave Arduinos, motor drivers, and stepper motors. The bottom three boards have four slave Arduinos and four motor drivers each, while the top board has two slave Arduinos and two motor drivers. Each slave Arduino is numbered from 1 to 14, as shown in Figure B–1, in reference to the grid bar it controls on the active grid.

To drive the motors, each slave Arduino is connected to a stepper motor driver with two pins: one step pin, and one direction pin. To make the design more space efficient, different slave Arduino are connected to the motor drivers with different pins. For example, slave Arduino 1 has pins A1 and A0, respectively, as the step and direction pins, while slave Arduino 3 has pins 5 and 4, respectively, as the step and direction pins. The pin assignments for the 14 slave Arduinos are presented in Table B–1.

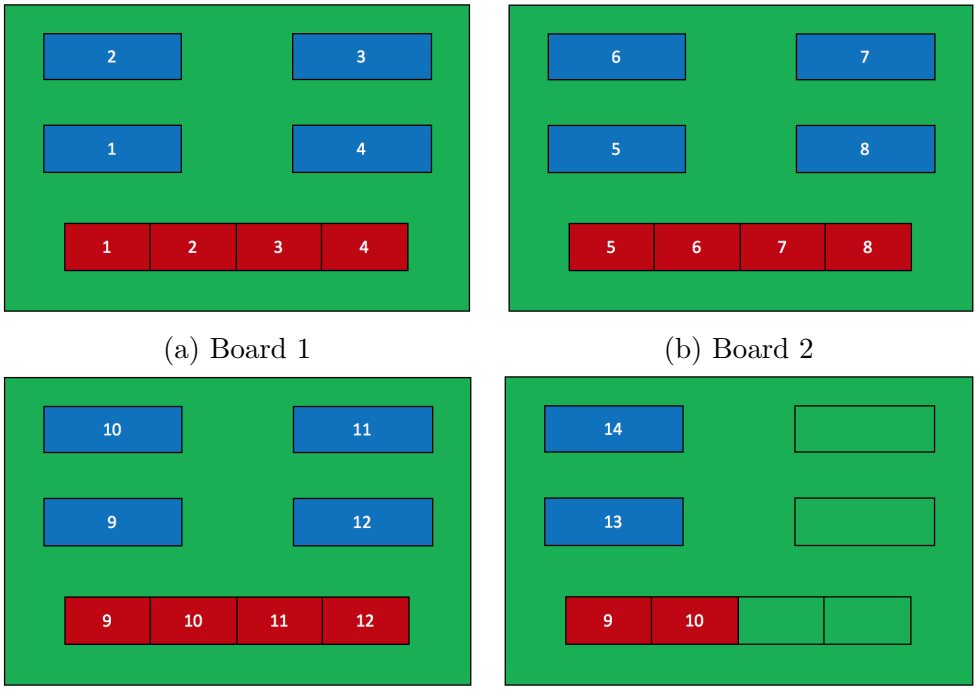

(a) Board 1

(b) Board 2

(c) Board 3

(d) Board 4

Figure B–1: Slave Arduino (blue) and stepper motor driver (red) numbering sequence on the active grid controller.

Slave Arduino	Step Pin	Direction Pin
1	A1	A0
2	A1	A0
3	5	4
4	5	4
5	A1	A0
6	A1	A0
7	5	4
8	5	4
9	A1	A0
10	A1	A0
11	5	4
12	5	4
13	A1	A0
14	A1	A0

Table B–1: Step and direction pin assignments for the slave Arduinos.

B.4 Troubleshooting

In the case where one of the active grid bars is not turning correctly, it is likely being caused by a loose connection, or a problem with the corresponding slave Arduino or motor driver.

If the active grid bar is turning with a jerky motion, this may be caused by a loose connection in the screw terminals. It may be enough to simply adjust the wires by hand. If this does not work, try disconnecting and reconnecting the wires in the screw terminal (each stepper motor is connected to the controller with 4 wires). If this still does not work, the problem may be in the cable that connects the active grid to the controller. To test this hypothesis, try switching the cable to another grid bar, and see if the problem persists.

To replace a slave Arduino with a new one, copy the code in Appendix A into the Arduino IDE. Determine the Arduino reference number, and note the corresponding step and direction pin assignments from Table B–1. Replace the *stepPin* and *dirPin* variables in the code with these. To initialize the random number generator with the proper "seed", change the *motorNum* variable to the corresponding Arduino reference number. Finally, upload the code to the new Arduino. Note that a slave Arduino must be disconnected from the active grid controller to upload a new code to it.

It is not uncommon for the motor drivers to overheat and stop working. To replace one, simply remove the old one and plug a new one in, ensuring it is in the same orientation as the others.

Appendix C: Uncertainty Analysis

In this appendix, an uncertainty analysis is performed on the time-mean velocity and force measurements made in this work, and used to compute the uncertainties in the Reynolds number, drag coefficient, and turbulence intensity. For each case, the uncertainties from individual sources are combined into a total uncertainty, as per the work of Jørgensen (2005).

C.1 Uncertainty in the Time-Mean Velocity Measurements

The uncertainty in the time-mean velocity measurements can be attributed to the following sources: i) the constant-temperature anemometer, ii) the calibration equipment, iii) changes in ambient-air temperature, iv) the data acquisition (DAQ) board, and v) the curve-fit to the calibration data.

As was mentioned in Chapter 2, constant-temperature anemometers (CTA) have a high frequency response, high signal-to-noise ratio, and good repeatability. The uncertainty in velocity measurements caused by the CTA is therefore taken to be negligible, compared to other experimental uncertainties in this work.

The TSI calibration equipment used in this work is assumed to have a relative uncertainty of 1%, consistent with typical values for commercial calibration equipment (Jørgensen 2005). To measure the uncertainty caused by the curve-fit to the calibration data, the mean-square error is computed, using the differences between the measured time-mean velocities ($U_{measured}$) and the velocities computed using the curve-fit function ($U_{curve-fit}$), normalized by the curve-fit velocities. The mean-square error for each point is then summed and divided by the number of points minus three, where the minus three represents the three degrees of freedom used in the curve fitting (i.e., the three calibration constants, A, B, and n), and its square-root is taken. This procedure yields the following equation:

$$uncertainty = \sqrt{\frac{1}{N-3}\sum_{i=1}^{N}\left(\frac{U_{curve-fit}-U_{measured}}{U_{curve-fit}}\right)^2}. \tag{C.1}$$

In this study, the uncertainty related to the calibration curve fit was 0.158%.

Variations of ambient-air temperature of up to $\pm 1^{\circ}C$ were observed between the time a hot-wire was calibrated to the end of a series of runs. The uncertainty related to temperature changes can be calculated as follows (Jørgensen 2005):

$$uncertainty = \frac{\Delta T}{\sqrt{3} U_{min}(T_w - T_a)} \left(\frac{A}{B} U_{min}^{-1/2} + 1 \right)^{1/2}, \tag{C.2}$$

where T_w is the wire temperature, T_a is the ambient-air temperature, ΔT is the observed change in ambient-air temperature, and U_{min} is the minimum measured velocity (4m/s). In this study, the uncertainty related to ambient-air temperature variations was 0.109%.

The uncertainty attributed to the DAQ board is assumed to be random and have a uniform distribution. The relative standard uncertainty can be calculated from the following expression, taken from the work of Jørgensen (2005):

$$uncertainty = \frac{E_{AD}}{\sqrt{3} U_{min} 2^n} \frac{\partial U}{\partial E}, \tag{C.3}$$

where E_{AD} is the input voltage range of the DAQ board (10V), n is the resolution of the acquisition board in bits (16), U_{min} is the minimum measured velocity (4m/s), and $\frac{\partial U}{\partial E}$ is the slope of the calibration curve. Using the maximum slope in this study ($\frac{\partial U}{\partial E}_{max} = 49.8$), the maximum relative uncertainty related to the acquisition board was 0.110%.

Adding all the aforementioned errors, the total relative uncertainty in the time-mean velocity measurements is 1.30%. Note that the uncertainties produced by changes in pressure, humidity, and positioning angle of the hot-wire probe were assumed to be negligible.

C.2 Uncertainty in the Force Measurements

The uncertainty in the force measurements can be attributed to the following sources: i) the load cells, ii) the calibration weights, iii) the data acquisition (DAQ) board, and iv) the curve-fit to the calibration data.

The uncertainty in the load cells was taken from the manufacturer's datasheet: it is

0.25%, including hysteresis and non-repeatbility. Also included in this datasheet is the effect of temperature on the uncertainty, notably $0.027\%/^{\circ}C$. As was mentioned above, the ambient-air temperature variation over a series of runs was $\pm 1^{\circ}C$. Thus, the total uncertainty related to the load cells is 0.277%.

As was mentioned in Chapter 3, the wind-tunnel balance was calibrated using gauge blocks, which were weighed to a precision of 0.01g. The relative uncertainty in these data can be calculated as follows:

$$uncertainty = \frac{1}{\sqrt{3}} \frac{0.01}{m_{min}}, \tag{C.4}$$

where m_{min} is the minimum mass used for calibration (31.2g). The uncertainty associated with the gauge block mass measurements is 0.018%.

The error caused by the calibration curve-fit to the data can be computed by applying Equation C.1 to the load cell calibrations. In these cases, only two calibration constants are used (A and B), corresponding to two degrees of freedom. This yields the following equation:

$$uncertainty = \sqrt{\frac{1}{N-2} \sum_{i=1}^{N} \left(\frac{F_{curve-fit} - F_{measured}}{F_{curve-fit}} \right)^2}. \tag{C.5}$$

In this study, the uncertainty related to the calibration curve fit was 0.283%.

The uncertainty attributed to the DAQ board can be measured by applying Equation C.3 to the force measurements in the following way:

$$uncertainty = \frac{E_{AD}}{\sqrt{3} F_{min} 2^n} \frac{\partial F}{\partial E}, \tag{C.6}$$

where F_{min} is the minimum measured force (10g), and $\frac{\partial F}{\partial E}$ is the slope of the calibration curve. Using the maximum slope in this study ($\frac{\partial F}{\partial E}_{max} = 10.0$), the maximum relative uncertainty related to the acquisition board was 0.009%.

Adding all the aforementioned errors, the total relative uncertainty in the force measurements is 0.59%.

C.3 Uncertainties in the Reynolds Number, Drag Coefficient and Turbulence Intensity

The uncertainties in the Reynolds number ($Re_D \equiv \frac{\overline{U}D}{\nu}$), drag coefficient ($C_D \equiv \frac{F_{drag}/A_{proj}}{\frac{1}{2}\rho\overline{U}^2}$), and turbulence intensity ($T_i \equiv \frac{u_{rms}}{\overline{U}}$), referred to as the total relative uncertainties, can be computed by adding the uncertainties of each term used to compute them in quadrature, as per the work of Taylor (1997):

$$\frac{\delta Re_D}{|Re_D|} = \sqrt{\left(\frac{\delta\overline{U}}{|\overline{U}|}\right)^2 + \left(\frac{\delta D}{|D|}\right)^2 + \left(\frac{\delta\nu}{|\nu|}\right)^2}, \tag{C.7}$$

$$\frac{\delta C_D}{|C_D|} = \sqrt{\left(\frac{\delta F_{drag}}{|F_{drag}|}\right)^2 + \left(\frac{\delta D}{|D|}\right)^2 + \left(\frac{\delta L}{|L|}\right)^2 + 2\left(\frac{\delta\overline{U}}{|\overline{U}|}\right)^2 + \left(\frac{\delta\rho}{|\rho|}\right)^2}, \quad \text{and} \tag{C.8}$$

$$\frac{\delta T_i}{|T_i|} = \sqrt{2\left(\frac{\delta\overline{U}}{|\overline{U}|}\right)^2}. \tag{C.9}$$

Here, the mean and fluctuating components of velocity are assumed to have the same relative uncertainty. The maximum relative uncertainty in the diameter was presented in Chapter 3 as 0.603%. The uncertainty in the cylinder length, measured with a ruler with a precision of $^1/_{32}$", was determined as 0.154%.

The density and viscosity were not explicitly measured, but taken from well established correlations for a given temperature and pressure (White 1991). Thus, the relative uncertainty in these properties was taken as the relative uncertainty of the ambient-air temperature measurement. The ambient-air temperature was measured with a thermocouple connected to a digital display, which had a resolution of $0.1°C$. The uncertainty in this temperature is:

$$uncertainty = \frac{1}{\sqrt{3}}\frac{0.1}{T}, \tag{C.10}$$

where T is the ambient-air temperature. Using the smallest temperature reading ($18°C$), the relative uncertainty in the temperature measurement is 0.321%. The total relative uncertainties in the Reynolds number, drag coefficient, and turbulence intensity, are summarized in Table C–1.

Variable	Relative Uncertainty (%)
Velocity (m/s)	1.30
Force (g)	0.59
Re	1.47
C_D	2.06
T_i	1.85

Table C–1: Relative uncertainties in measured and calculated quantities.

Appendix D: Instructions for Drag Experiments

In this appendix, the experimental procedure for installing a cylinder on the wind tunnel balance (WTB), calibrating the WTB, and measuring drag are presented.

D.1 Installing a Cylinder on the Wind Tunnel Balance

1. Remove the three connecting rods from the WTB, and place protective caps over each load cell.
2. A threaded rod with a washer, nut and two stops is used to hold the cylinder in place during installation. Thread the nut to the upper stop of the threaded rod.
3. From the top of the wind tunnel, screw the threaded rod into the top of the cylinder (not too tightly) until the washer is flush with the top wall of the tunnel.
4. Remove the 2 horizontal screws fastening the cylinder base to the WTB bracket. The cylinder should remain in place as it is supported by the threaded rod.
5. Lift up the threaded rod, and thread the nut down until the washer reaches the lower stop. The bottom of the cylinder should now be a few inches above the WTB.
6. Unscrew the bolt fastening the bottom of the cylinder to the cylinder base. Support the bolt from the bottom to prevent it from falling on the WTB when it is unscrewed.
7. Using the threaded rod, pull the cylinder out from the top of the tunnel.
8. Thread the rod into the next cylinder all the way until the stop, without making it too tight (over-tightening risks stripping the threads on the cylinder).
9. Slide the new cylinder into the tunnel from the top, until the washer is flush with the top wall of the wind tunnel.
10. Screw the cylinder base into bottom of cylinder, ensuring that the seam of the porous cylinder is oriented in the downstream direction. Again, take care not to screw it too tightly so as not to damage the threads.

11. From the top of the tunnel, thread the nut along the threaded rod until the upper stop, lowering the cylinder towards the WTB. The holes on the cylinder base should be roughly aligned with the holes on the WTB bracket.
12. Insert the screws into the cylinder base without installing the nuts. Unscrew the threaded rod from the cylinder. Check to make sure the cylinder is not touching either of the end plates.
13. Thread the nuts into the bolts on the cylinder base. Verify once more that the cylinder is not touching either of the end plates.

D.2 Calibrating the Wind Tunnel Balance

The WTB should be calibrated each time a new cylinder is installed, or for the same cylinder, a minimum of once per day. Elastics can be used to stiffen the WTB to reduce load cell drift over time.

1. Remove all connecting rods from the WTB.
2. Record the voltages from the 3 load cells (1.024×10^4 samples recorded at a rate of 400Hz). This is the no-load voltage for each load cell.
3. Using these voltages, as well as the typical slopes presented in Table D–1, compute the required pre-compression voltage values for each load cell.
4. Re-connect the rods. Plug the output from the first load cell into the multi-meter, and using a hex key, adjust the two calibration screws until the voltage is within $\pm$ 1mV of the calculated pre-compression voltage values.
5. Repeat step 4 for the other two load cells. Once all the load cells are pre-compressed to the desired values, wait 10 minutes for the WTB to stabilize.
6. Record a zero reading for all three load cells (1.024×10^4 samples recorded at a rate of 400Hz).
7. Using the rope, screw and pulley, load the 0.3" gauge block ($\sim$30g) onto the WTB. Wait 5 minutes for the WTB to stabilize, then record the voltages of the three load cells (1.024×10^4 samples recorded at a rate of 400Hz).

8. Repeat step 6 for gauge blocks 0.4", 0.5", 0.6", 0.7", 0.8", 0.9", and 1".
9. After removing the final gauge block, wait 5 minutes before recording another zero reading. It is not unusual for this value to be different from the pre-calibration value.

Variable	Load Cell 1	Load Cell 2	Load Cell 3
Typical slope a (mV/g)	0.18	0.10	0.17
Typical no-load reading x_0 (mV)	60	18	-36
Desired pre-compression F_0 (g)	200	200	100
Pre-compression voltage $(= x_0 + aF_0)$ (mV)	96	38	-19

Table D–1: Typical pre-compression voltage for each load cell on the wind tunnel balance.

D.3 Measuring Drag

1. Insert the hot-wire probe into the tunnel upstream of the cylinder ($x = 2.32$m). Using markings on the probe shield, set the hot-wire to the tunnel centreline ($y = 0$"), with the elbow parallel to the flow.
2. Measure the hot-wire ambient resistance, and verify that it has not drifted more than $\pm 0.02\Omega$ from the ambient resistance measured during calibration. If it has, the hot-wire should be recalibrated.
3. Compute the hot-wire operating resistance, and set the hot-wire anemometer to operate.
4. If required, turn on the active grid.
5. Record three successive zero readings of the WTB to ensure it has stabilized. Use the final reading as the zero.
6. Turn on the blower and set it to the required frequency to obtain a mean velocity around 4m/s.
7. Record the initial temperature by inserting a thermocouple into the flow.
8. Adjust the blower frequency until the mean velocity is within ± 0.05m/s of 4m/s, then record a mean velocity reading (1.024×10^4 samples recorded at a rate of 400Hz).

9. Set the hot-wire probe near the wall to $y = -7$" to minimize interference with the air flow over the cylinder.
10. Wait 5 minutes for the WTB to stabilize, then record the voltages from all three load cells, using the following parameters:
    - At 4 m/s: 1.2288×10^5 samples recorded at a rate of 400Hz.
    - At 6, 8, and 10 m/s: 4.096×10^4 samples recorded at a rate of 400Hz.
11. Using the recorded voltages, the zero readings, and the slopes obtained during calibration, compute the drag force measured by each load cell.
12. Set the hot-wire back to the tunnel centreline ($y = 0$"), and record another mean velocity reading (1.024×10^4 samples recorded at a rate of 400Hz).
13. Using the average of the two mean velocity measurements, and the average of the drag forces measured with the three load cells, compute the drag coefficient.
14. Repeat steps 8-13 for nominal mean velocities of 6, 8, and 10 m/s.
15. Record the final temperature by inserting a thermocouple into the flow.
16. Turn off the blower. Set the hot-wire anemometer to standby. Wait at least 10 minutes for the WTB to stabilize before the next test.
17. Turn off the active grid.

Appendix E: Raw Data Related to Drag-Force Measurements

PPI	PLT (in)	Grid	$U\ (m/s)$	Re_D	C_D
Smooth	-	None	3.95	6668	0.90
			5.97	10072	0.93
			7.98	13467	0.95
			10.03	16928	0.98
		Passive 1in	4.01	6764	0.96
			6.01	10142	1.00
			7.98	13473	1.01
			9.96	16813	1.04
		Passive 2in	3.99	6731	1.02
			5.96	10064	1.05
			7.99	13492	1.08
			9.95	16806	1.11
		Active	4.04	6815	0.89
			5.98	10101	0.93
			7.95	13424	0.95
			9.96	16810	0.96

Table E–1: Raw data for smooth cylinder.

PPI	PLT (in)	Grid	U (m/s)	Re_D	C_D
10	1/16	None	4.05	7180	1.06
			6.02	10678	1.09
			8.10	14362	1.12
			10.09	17882	1.15
		Passive 1in	4.11	7284	1.21
			6.10	10821	1.23
			8.12	14403	1.24
			10.07	17854	1.23
		Passive 2in	4.10	7264	1.27
			6.15	10911	1.30
			8.11	14371	1.30
			10.09	17889	1.28
		Active	4.05	7174	1.23
			6.12	10859	1.24
			8.16	14462	1.24
			10.18	18051	1.24

Table E–2: Raw data for 10 PPI−1/16" PLT cylinder.

PPI	PLT (in)	Grid	U (m/s)	Re_D	C_D
10	1/8	None	3.96	6691	1.14
			5.96	10080	1.16
			7.97	13480	1.18
			9.94	16797	1.20
		Passive 1in	3.95	6677	1.32
			5.93	10032	1.33
			7.97	13465	1.33
			9.96	16843	1.32
		Passive 2in	4.03	6811	1.36
			6.09	10300	1.37
			8.14	13752	1.37
			10.12	17107	1.35
		Active	3.95	6675	1.28
			5.96	10078	1.32
			7.89	13339	1.31
			9.94	16797	1.31

Table E–3: Raw data for 10 PPI−1/8" PLT cylinder.

PPI	PLT (in)	Grid	U (m/s)	Re_D	C_D
10	1/4	None	3.92	6687	1.18
			5.96	10065	1.23
			7.96	13440	1.25
			9.96	16820	1.28
		Passive 1in	4.09	6916	1.32
			6.17	10414	1.33
			8.19	13829	1.34
			10.17	17174	1.33
		Passive 2in	4.04	6822	1.39
			6.09	10283	1.41
			8.13	13727	1.39
			10.16	17157	1.40
		Active	3.93	6643	1.33
			6.02	10166	1.34
			7.96	13439	1.36
			9.99	16880	1.37

Table E–4: Raw data for 10 PPI−1/4" PLT cylinder.

PPI	PLT (in)	Grid	U (m/s)	Re_D	C_D
20	1/16	None	4.05	6697	0.96
			6.00	9927	1.01
			7.95	13137	1.04
			9.93	16424	1.07
		Passive 1in	4.01	6630	1.06
			6.01	9940	1.11
			8.00	13229	1.13
			9.99	16516	1.14
		Passive 2in	4.02	6644	1.13
			6.01	9934	1.18
			8.04	13292	1.21
			10.01	16555	1.21
		Active	4.04	6687	1.04
			6.07	10037	1.09
			8.09	13380	1.07
			9.96	16460	1.07

Table E–5: Raw data for 20 PPI−1/16" PLT cylinder.

PPI	PLT (in)	Grid	U (m/s)	Re_D	C_D
20	1/8	None	3.95	6597	1.11
			5.97	9971	1.13
			7.98	13343	1.15
			9.98	16684	1.16
		Passive 1in	3.95	6602	1.22
			5.94	9934	1.26
			8.00	13369	1.27
			9.96	16641	1.28
		Passive 2in	4.01	6699	1.31
			6.01	10043	1.35
			8.01	13390	1.37
			10.00	16715	1.37
		Active	3.99	6674	1.16
			5.99	10004	1.20
			8.03	13423	1.21
			9.98	16679	1.22

Table E–6: Raw data for 20 PPI−1/8" PLT cylinder.

PPI	PLT (in)	Grid	U (m/s)	Re_D	C_D
20	1/4	None	3.96	6590	1.11
			6.00	9992	1.15
			8.01	13334	1.17
			9.99	16637	1.20
		Passive 1in	3.97	6616	1.25
			5.96	9929	1.27
			8.03	13376	1.29
			9.96	16582	1.31
		Passive 2in	4.01	6687	1.32
			6.03	10037	1.35
			8.00	13317	1.37
			9.98	16628	1.38
		Active	4.03	6706	1.22
			6.01	10015	1.26
			8.02	13359	1.26
			10.00	16656	1.28

Table E–7: Raw data for 20 PPI−1/4" PLT cylinder.

PPI	PLT (in)	Grid	U (m/s)	Re_D	C_D
40	1/16	None	4.02	6794	1.10
			6.00	9935	1.14
			8.01	13268	1.19
			10.03	16623	1.23
		Passive 1in	3.97	6573	1.20
			5.97	9885	1.25
			7.97	13196	1.29
			9.92	16441	1.32
		Passive 2in	3.98	6599	1.30
			5.98	9904	1.34
			7.99	13234	1.38
			9.96	16505	1.40
		Active	4.10	6797	0.96
			6.02	9971	1.01
			7.99	13232	1.01
			10.03	16621	0.97

Table E–8: Raw data for 40 PPI−1/16" PLT cylinder.

PPI	PLT (in)	Grid	U (m/s)	Re_D	C_D
40	1/8	None	3.98	6649	1.15
			6.00	10019	1.24
			7.99	13345	1.28
			10.01	16704	1.30
		Passive 1in	4.01	6694	1.35
			6.01	10035	1.40
			8.01	13377	1.42
			9.96	16622	1.44
		Passive 2in	3.96	6605	1.37
			5.91	9870	1.43
			8.04	13426	1.47
			9.98	16661	1.48
		Active	4.08	6803	1.06
			5.96	9956	1.12
			8.06	13452	1.13
			9.97	16636	1.14

Table E–9: Raw data for 40 PPI−1/8" PLT cylinder.

PPI	PLT (in)	Grid	U (m/s)	Re_D	C_D
40	1/4	None	4.00	6569	1.21
			5.99	9842	1.26
			8.00	13151	1.28
			10.01	16446	1.30
		Passive 1in	4.00	6571	1.35
			5.99	9837	1.37
			7.98	13112	1.39
			10.01	16445	1.41
		Passive 2in	4.00	6565	1.36
			6.00	9867	1.42
			8.02	13185	1.45
			10.04	16504	1.46
		Active	4.01	6588	1.11
			5.98	9829	1.15
			7.98	13114	1.17
			10.00	16441	1.14

Table E–10: Raw data for 40 PPI−1/4" PLT cylinder.

REFERENCES

Achenbach, E. (1968). "Distribution of local pressure and skin friction around a circular cylinder in cross-flow up to $Re = 5 \times 10^6$". *Journal of Fluid Mechanics*, 34 (4), pp. 625–639.

Adams, M. A. (2013). "Mega-fires, tipping points and ecosystem services: Managing forests and woodlands in an uncertain future". *Forest Ecology and Management*, 294, pp. 250–261.

Albini, F. A. (1979). *Spot fire distance from burning trees: a predictive model*. Technical Report INT-56. Ogden, UT: USDA Forest Service, Intermountain Forest and Range Experiment Station.

Albini, F. A. (1981). "A model for the wind-blown flame from a line fire". *Combustion and Flame*, 43, pp. 155–174.

Allen, H. J. and Vincenti, W. G. (1944). *Wall interference in a two-dimensional-flow wind tunnel with consideration of the effect of compressibility*. Technical Report 782. National Advisory Committee for Aeronautics NACA.

Anthenien, R. A., Stephen, D. T., and Fernandez-Pello, A. C. (2006). "On the trajectories of embers initially elevated or lofted by small-scale ground fire plumes in high winds". *Fire Safety Journal*, 41 (5), pp. 349–363.

Aon Benfield (2018). *Companion Volume to Weather, Climate Catastrophe Insight: Additional Data to Accompany the 2017 Annual Report*. `http://thoughtleadership.aonbenfield.com/Documents/20180124-ab-if-annual-companion-volume.pdf`.

Arie, M., Kiya, M., Suzuki, Y., Hagino, M., and Takahashi, K. (1981). "Characteristics of circular cylinders in turbulent flows". *Bulletin of the JSME*, 24 (190), pp. 640–647.

Baum, H. R. and McCaffrey, B. (1989). "Fire induced flow field-theory and experiment". *Fire Safety Science*, 2, pp. 129–148.

Bearman, P. and Morel, T. (1983). "Effect of free stream turbulence on the flow around bluff bodies". *Progress in Aerospace Sciences*, 20 (2-3), pp. 97–123.

Beaulac, S. and Mydlarski, L. (2004a). "Dependence on the initial conditions of scalar mixing in the turbulent wake of a circular cylinder". *Physics of Fluids*, 16 (8), pp. 3161–3172.

Beaulac, S. and Mydlarski, L. (2004b). "Inverse structure functions of temperature in grid-generated turbulence". *Physics of Fluids*, 16 (6), pp. 2126–2129.

Berajeklian, A. and Mydlarski, L. (2011). "Simultaneous velocity-temperature measurements in the heated wake of a cylinder with implications for the modeling of turbulent passive scalars". *Physics of Fluids*, 23. Art. no. 055107.

Bhattacharyya, S. and Singh, A. (2011). "Reduction in drag and vortex shedding frequency through porous sheath around a circular cylinder". *International Journal for Numerical Methods in Fluids*, 65 (6), pp. 683–698.

British Columbia Wildfire Service (2018). *Wildfire Season Summary*. `https://www2.gov.bc.ca/gov/content/safety/wildfire-status/about-bcws/wildfire-history/wildfire-season-summary`.

Bruneau, C.-H. and Mortazavi, I. (2006). "Control of vortex shedding around a pipe section using a porous sheath". *International Journal of Offshore and Polar Engineering*, 16 (2), pp. 90–96.

Bruun, H. H. (1987). *Hot-wire Anemometry: Principles and Signal Analysis*. Oxford University Press.

Cattafesta, L., Bahr, C., and Mathew, J. (2010). "Fundamentals of wind-tunnel design". *Encyclopedia of Aerospace Engineering*, pp. 1–10.

Cheung, J. and Melbourne, W. (1983). "Turbulence effects on some aerodynamic parameters of a circular cylinder at supercritical Reynolds numbers". *Journal of Wind Engineering and Industrial Aerodynamics*, 14, pp. 399–410.

Comte-Bellot, G. and Corrsin, S. (1966). "The use of a contraction to improve the isotropy of grid-generated turbulence". *Journal of Fluid Mechanics*, 25 (4), pp. 657–682.

Comte-Bellot, G. and Corrsin, S. (1971). "Simple Eulerian time correlation of full-and narrow-band velocity signals in grid-generated, 'isotropic' turbulence". *Journal of Fluid Mechanics*, 48 (2), pp. 273–337.

Counihan, J. (1975). "Adiabatic atmospheric boundary layers: a review and analysis of data from the period 1880–1972". *Atmospheric Environment*, 9 (10), pp. 871–905.

Dalton, C. (1971). "Allen and Vincenti blockage corrections in a wind tunnel". *AIAA Journal*, 9 (9), pp. 1864–1865.

Delany, N. K. and Sorensen, N. E. (1953). *Low-speed drag of cylinders of various shapes*. Technical Report 3038. National Advisory Committee for Aeronautics NACA.

Eames, I., Jonsson, C., and Johnson, P. (2011). "The growth of a cylinder wake in turbulent flow". *Journal of Turbulence*, (12), N39.

Fage, A. and Faulkner, V. (1931). *Further experiments on the flow around a circular cylinder*. Technical Report 1369. Aeronautical Research Council Reports & Memoranda.

Fage, A. and Warsap, J. (1929). *The effects of turbulence and surface roughness on the drag of a circular cylinder*. Technical Report 1283. Aeronautical Research Council Reports & Memoranda.

Gad-el-Hak, M. and Corrsin, S. (1974). "Measurements of the nearly isotropic turbulence behind a uniform jet grid". *Journal of Fluid Mechanics*, 62 (1), pp. 115–143.

Hearst, R. J. and Lavoie, P. (2015). "The effect of active grid initial conditions on high Reynolds number turbulence". *Experiments in Fluids*, 56 (10), p. 185.

Jørgensen, F. E. (2005). *How to Measure Turbulence with Hot-Wire Anemometers: a Practical Guide*. Dantec dynamics.

Khorsandi, B., Gaskin, S., and Mydlarski, L. (2013). "Effect of background turbulence on an axisymmetric turbulent jet". *Journal of Fluid Mechanics*, 736, pp. 250–286.

Klausmann, K. and Ruck, B. (2017). "Drag reduction of circular cylinders by porous coating on the leeward side". *Journal of Fluid Mechanics*, 813, pp. 382–411.

Ko, S. C. and Graf, W. H. (1972). "Drag coefficient of cylinders in turbulent flow". *Journal of the Hydraulics Division*, 98 (5), pp. 897–912.

Koo, E., Pagni, P. J., Weise, D. R., and Woycheese, J. P. (2010). "Firebrands and spotting ignition in large-scale fires". *International Journal of Wildland Fire*, 19 (7), pp. 818–843.

Kubo, Y., Miyazaki, M., and Kato, K. (1989). "Effects of end plates and blockage of structural members on drag forces". *Journal of Wind Engineering and Industrial Aerodynamics*, 32 (3), pp. 329–342.

Larssen, J. V. and Devenport, W. J. (2011). "On the generation of large-scale homogeneous turbulence". *Experiments in Fluids*, 50 (5), pp. 1207–1223.

Lee, S.-L. and Hellman, J. (1969). "Study of firebrand trajectories in a turbulent swirling natural convection plume". *Combustion and Flame*, 13 (6), pp. 645–655.

Lee, S.-L. and Hellman, J. (1970). "Firebrand trajectory study using an empirical velocity-dependent burning law". *Combustion and Flame*, 15 (3), pp. 265–274.

Lepore, J. and Mydlarski, L. (2009). "Effect of the scalar injection mechanism on passive scalar structure functions in a turbulent flow". *Physical Review Letters*, 103. Art. no. 034501.

Lepore, J. and Mydlarski, L. (2012). "Finite-Péclet-number effects on the scaling exponents of high-order passive scalar structure functions". *Journal of Fluid Mechanics*, 713, pp. 453–481.

Lienhard, J. H. (1966). *Synopsis of lift, drag, and vortex frequency data for rigid circular cylinders*. Technical Extension Service, Washington State University.

Makita, H. (1991). "Realization of a large-scale turbulence field in a small wind tunnel". *Fluid Dynamics Research*, 8 (1-4), pp. 53–64.

Manzello, S. L., Park, S.-H., Suzuki, S., Shields, J. R., and Hayashi, Y. (2011). "Experimental investigation of structure vulnerabilities to firebrand showers". *Fire Safety Journal*, 46 (8), pp. 568–578.

Massey, B. S. (1979). *Mechanics of Fluids*. 4th Edition. Van Nostrand Reinhold.

Medvescek, J. (2013). "Experimental investigation of fully developed flows of a Newtonian fluid in straight rectangular ducts with adjacent open and porous-metal-foam domains". M. Eng. thesis. McGill University.

Medvescek, J., Afara, S., Mydlarski, L., and Baliga, B. R. (2014). "Calibration of a wall-shear-stress sensor made of a flush-mounted hot-wire over a shallow rectangular slot". *ASME 2014 International Mechanical Engineering Congress and Exposition*. American Society of Mechanical Engineers, V007T09A097–V007T09A097.

Muraszew, A. and Fedele, J. (1976). *Statistical model for spot fire spread*. Technical Report ATR-77(7588)-1. Los Angeles, CA: The Aerospace Corporation.

Muraszew, A. and Fedele, J. (1977). "Trajectory of firebrands in and out of fire whirls". *Combustion and Flame*, 30, pp. 321–324.

Muraszew, A., Kuby, W., and Fedele, J. (1975). *Firebrand investigation*. Technical Report ATR-75(7470)-1. Los Angeles, CA: The Aerospace Corporation.

Mydlarski, L. (2017). "A turbulent quarter century of active grids: from Makita (1991) to the present". *Fluid Dynamics Research*, 49. Art. no. 061401.

Mydlarski, L. and Warhaft, Z. (1996). "On the onset of high-Reynolds-number grid-generated wind tunnel turbulence". *Journal of Fluid Mechanics*, 320, pp. 331–368.

Mydlarski, L. and Warhaft, Z. (1998). "Passive scalar statistics in high-Péclet-number grid turbulence". *Journal of Fluid Mechanics*, 358, pp. 135–175.

Norberg, C. (1987). "Effects of Reynolds number and a low-intensity freestream turbulence on the flow around a circular cylinder". *Chalmers University, Goteborg, Sweden, Technological Publications*, 87 (2), pp. 1–55.

Ohmiya, Y. and Iwami, T. (2000). "An investigation on the distribution of fire brands and spot fires due to a hotel fire". *Fire Science and Technology*, 20 (1), pp. 27–35.

Okamoto, T. and Yagita, M. (1973). "The experimental investigation on the flow past a circular cylinder of finite length placed normal to the plane surface in a uniform stream". *Bulletin of JSME*, 16 (95), pp. 805–814.

Oliveira, L. A., Lopes, A. G., Baliga, B. R., Almeida, M., and Viegas, D. X. (2014). "Numerical prediction of size, mass, temperature and trajectory of cylindrical wind-driven firebrands". *International Journal of Wildland Fire*, 23 (5), pp. 698–708.

Pal, A. and Sarkar, S. (2015a). "Effect of external turbulence on a turbulent wake". *International Symposium on Turbulence and Shear Flow Phenomena TSFP*. Melbourne, Australia.

Pal, A. and Sarkar, S. (2015b). "Effect of external turbulence on the evolution of a wake in stratified and unstratified environments". *Journal of Fluid Mechanics*, 772, pp. 361–385.

Pope, S. B. (2000). *Turbulent Flows*. Cambridge University Press.

Ragland, K., Aerts, D., and Baker, A. (1991). "Properties of wood for combustion analysis". *Bioresource technology*, 37 (2), pp. 161–168.

Rind, E. and Castro, I. P. (2012a). "Direct numerical simulation of axisymmetric wakes embedded in turbulence". *Journal of Fluid Mechanics*, 710, pp. 482–504.

Rind, E. and Castro, I. P. (2012b). "On the effects of free-stream turbulence on axisymmetric disc wakes". *Experiments in Fluids*, 53 (2), pp. 301–318.

Roshko, A. (1954). *On the development of turbulent wakes from vortex streets*. Technical Report 1191. National Advisory Committee for Aeronautics NACA.

Sadeh, W. Z. and Saharon, D. B. (1982). *Turbulence effect on crossflow around a circular cylinder at subcritical Reynolds numbers*. NASA Contractor Report 3622. National Aeronautics and Space Administration.

Sardoy, N., Consalvi, J.-L., Porterie, B., and Fernandez-Pello, A. C. (2007). "Modeling transport and combustion of firebrands from burning trees". *Combustion and Flame*, 150 (3), pp. 151–169.

Schulz, K. W. and Kallinderis, Y. (2000). "Three-dimensional numerical prediction of the hydrodynamic loads and motions of offshore structures". *Journal of Offshore Mechanics and Arctic Engineering*, 122 (4), pp. 294–300.

Simmons, L. and Salter, C. (1934). "Experimental investigation and analysis of the velocity variations in turbulent flow". *Proc. R. Soc. Lond. A*, 145 (854), pp. 212–234.

Simms, C. D. (2016). "Canada's Fort McMurray fire: mitigating global risks". *The Lancet Global Health*, 4 (8).

Sirivat, A. and Warhaft, Z. (1983). "The effect of a passive cross-stream temperature gradient on the evolution of temperature variance and heat flux in grid turbulence". *Journal of Fluid Mechanics*, 128, pp. 323–346.

Sobera, M. P., Kleijn, C. R., Akker, H. E. Van den, and Brasser, P. (2003). "Convective heat and mass transfer to a cylinder sheathed by a porous layer". *AIChE Journal*, 49 (12), pp. 3018–3028.

Stansby, P. (1974). "The effects of end plates on the base pressure coefficient of a circular cylinder". *The Aeronautical Journal*, 78 (757), pp. 36–37.

Stewart, R. W. and Townsend, A. A. (1951). "Similarity and self-preservation in isotropic turbulence". *Phil. Trans. R. Soc. Lond. A*, 243 (867), pp. 359–386.

Tarifa, C. S., del Notario, P. P., and Moreno, F. G. (1965). "On the flight paths and lifetimes of burning particles of wood". *Proceedings of the Combustion Institute*. Vol. 10. 1. Elsevier, pp. 1021–1037.

Taylor, J. (1997). *Introduction to Error Analysis, the Study of Uncertainties in Physical Measurements*. 2nd Edition. University Science Books.

Tennekes, H. and Lumley, J. L. (1972). *A First Course in Turbulence*. MIT press.

Tse, S. D. and Fernandez-Pello, A. C. (1998). "On the flight paths of metal particles and embers generated by power lines in high winds a potential source of wildland fires". *Fire Safety Journal*, 30 (4), pp. 333–356.

Viegas, D. X. (1998). "Forest fire propagation". *Philosophical Transactions-Mathematical Physical and Engineering Sciences*, 356 (1748), pp. 2907–2928.

Von Kármán, T. (1911). "Über den Mechanismus des Widerstandes, den ein bewegter Körper in einer Flüssigkeit erfährt (On the mechanism of drag generation on the body moving in fluid)". *Nachrichten von der Gesellschaft der Wissenschaften zu Göttingen*, pp. 509–517.

Watanabe, T., Kato, T., Kamata, Y., and Onodera, A. (1989). "The air flow around a clothed cylinder". *Sen'i Gakkaishi*, 45 (5), pp. 175–182.

Watanabe, T., Kato, T., and Kamata, Y. (1991). "The velocity distribution in the inner flow field around a clothed cylinder". *Sen'i Gakkaishi*, 47 (6), pp. 271–275.

White, F. M. (1991). *Viscous Fluid Flow*. 2nd Edition. McGraw-Hill.

Wieselsberger, C. (1921). "Neuere feststellungen uber die gesetze des flussigkeits und luftwiderstands (New data on the law of hydro and aerodynamic resistance)". *Physik Zeitschrift*, 22, pp. 321–328.

Wieselsberger, C. (1922). "Weitere Feststellungen uber die Gesetze des Flussigkeits und Luftwiderstandes (Other observations on the laws of fluid and air resistance)". *Physik Zeitschrift*, 23, pp. 219–224.

Woycheese, J. P., Pagni, P. J., and Liepmann, D. (1999). "Brand propagation from large-scale fires". *Journal of Fire Protection Engineering*, 10 (2), pp. 32–44.

Wu, J.-S. and Faeth, G. (1994). "Sphere wakes at moderate Reynolds numbers in a turbulent environment". *AIAA Journal*, 32 (3), pp. 535–541.

Wu, J.-S. and Faeth, G. (1995). "Effect of ambient turbulence intensity on sphere wakes at intermediate Reynolds number". *AIAA Journal*, 33 (1), pp. 171–173.

Yin, C., Rosendahl, L., Kær, S. K., and Sørensen, H. (2003). "Modelling the motion of cylindrical particles in a nonuniform flow". *Chemical Engineering Science*, 58 (15), pp. 3489–3498.

Zdravkovich, M. M. (1997a). *Flow around Circular Cylinders Volume 1: Fundamentals*. Oxford University Press.

Zdravkovich, M. M. (1997b). *Flow around Circular Cylinders: Volume 2: Applications*. Oxford University Press.

Zdravkovich, M. M., Brand, V., Mathew, G., and Weston, A. (1989). "Flow past short circular cylinders with two free ends". *Journal of Fluid Mechanics*, 203, pp. 557–575.